AD NUMBER: AD0865997
LIMITATION CHANGES
TO: Approved for public release; distribution is unlimited.
FROM: This document is subject to special export controls; 01 Feb 1970, and each transmittal to foreign governments or foreign nationals may be made only with prior approval of the AF Flight Dynamics laboratory (FDFR), Wright-Patterson AFB, Ohio.
AUTHORITY
ST-A AFFDL LTR, 6 APR 1972

AFFDL - TR - 70 - 1
PART I, VOLUME I

STUDY AND DESIGN OF AN EJECTION SYSTEM FOR VTOL AIRCRAFT

PART I, VOLUME I

VTOL AIRCRAFT EQUATIONS AND FAILURE MODE ANALYSIS

I. L. Clinkenbeard
E. O. Cartwright, Jr.

Vought Aeronautics Division
LTV Aerospace Corporation

Technical Report AFFDL - TR - 70 - 1, PART I, VOLUME I

FEBRUARY 1970

AIR FORCE FLIGHT DYNAMICS LABORATORY
AIR FORCE SYSTEMS COMMAND
WRIGHT-PATTERSON AIR FORCE BASE, OHIO

NOTICE

When Government drawings, specifications, or other data are used for any purpose other than in connection with a definitely related Government procurement operation, the United States Government thereby incurs no responsibility nor any obligation whatsoever; and the fact that the government may have formulated, furnished, or in any way supplied the said drawings, specifications, or other data, is not to be regarded by implication or otherwise as in any manner licensing the holder or any other person or corporation, or conveying any rights or permission to manufacture, use, or sell any patented invention that may in any way be related thereto.

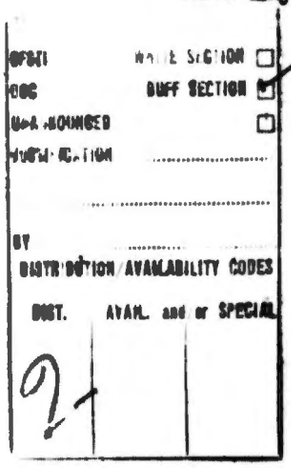

This document is subject to special export controls and each transmittal to foreign governments or foreign nationals may be made only with prior approval of the AF Flight Dynamics Laboratory (FDFR), Wright-Patterson AFB, Ohio.

The distribution of this report is limited because it describes the capabilities and limitations of crew escape concepts for aerospace vehicles in VTOL and conventional take off and landing situations.

Copies of this report should not be returned unless return is required by security considerations, contractual obligations, or notice on a specific document.

AFFDL - TR - 70 - 1

STUDY AND DESIGN OF AN EJECTION SYSTEM FOR VTOL AIRCRAFT

PART I, VOLUME I
VTOL AIRCRAFT EQUATIONS AND FAILURE MODE ANALYSIS

I. L. CLINKENBEARD
E. O. CARTWRIGHT, Jr.

FOREWORD

This report was prepared by the Vought Aeronautics Division of the LTV Aerospace Corporation, a subsidiary of Ling-Temco-Vought, Inc., under Air Force Contract F 33615-69-C-1692. This contract was initiated under Project 1362, "Crew Escape for Flight Vehicles", Task No. 136203, "Crew Escape Techniques Research". The program is administered under the direction of the Recovery and Crew Station Branch, Vehicle Equipment Division, Air Force Flight Dynamics Laboratory, Air Force Systems Command, Wright-Patterson Air Force Base, Ohio. Mr. B. J. White (FDFR) was the Air Force Project Engineer.

This report covers work conducted during the period April 1969 to December 1969. It was submitted by the authors in December 1969.

The documentation of this project necessitates publication in several parts. The total documentation includes:

Part I
- Volume 1- VTOL Aircraft Equations and Failure Mode Analysis
- Volume 2- Escape System Parameters Analysis
- Volume 3- Computer Program User's Manual for VTOL Escape System Simulation

Part II
- Volume 1- Escape Seat Systems Concept Analysis
- Volume 2- Escape Seat Subsystems and Detail Drawings

This technical report has been reviewed and is approved.

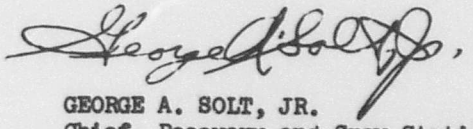

GEORGE A. SOLT, JR.
Chief, Recovery and Crew Station Branch
Vehicle Equipment Division
Air Force Flight Dynamics Laboratory

ABSTRACT

Equations are formulated for a hypothetical fighter/close support VTOL aircraft which will simulate a realistically severe crew station escape environment arising from aircraft failures in the VTOL and high speed,low altitude flight regimes. Four candidate airplanes with dissimilar propulsive and control concepts are analyzed and a lift-fan configuration is selected for a digital computer simulation programmed with the intent to test the feasibility of any crew escape concept. Plotted time histories are presented of aircraft and crew station positions, rates, and accelerations occurring as a consequence of various failure modes. The time histories are summarized to reveal the extreme conditions encountered during VTOL and high speed emergencies, conditions for which existing escape systems are not designed.

(Page iv is blank)

TABLE OF CONTENTS

LIST OF FIGURES

LIST OF TABLES

LIST OF SYMBOLS:

SYMBOL	UNITS	DEFINITION
$\ddot{\Delta h}$	ft/sec^2	Altitude acceleration increment from trimmed flight
$\dot{\Delta h}$	ft/sec	Climb rate increment
Δh	ft	Altitude increment
$\ddot{\Delta\theta}$	rad/sec^2	Pitch acceleration increment
$\dot{\Delta\theta}$	rad/sec	Pitch rate increment
$\Delta\theta$	rad	Pitch attitude increment
$\ddot{\Delta\phi}$	rad/sec^2	Bank angle acceleration increment
$\dot{\Delta\phi}$	rad/sec	Roll rate increment
$\Delta\phi$	rad	Bank angle
ΔT	lb	Thrust loss
$\Delta\tau_x = \Delta L$	ft-lb	Upset rolling moment
$\Delta\tau_y = \Delta M$	ft-lb	Upset pitching moment
τ_q	sec	Pitch damping time constant
τ_p	sec	Roll damping time constant
$\tau_w = -1/z_w$	sec	Heave damping time constant
GW	lb	Gross weight
I_x	$slug\text{-}ft^2$	Rolling moment of inertia
I_y	$slug\text{-}ft^2$	Pitching moment of inertia
t	sec	Time
C_{m_q}	rad^{-1}	Pitch Damping Derivative
$C_{m_{\dot\alpha}}$	rad^{-1}	Plunge Damping Derivative
C_{ℓ_p}	rad^{-1}	Roll Damping Derivative

The three damping time constants (pitch, roll, heave) are primarily due to a $\dot{\Delta}v$ in hover.

SYMBOL	UNITS	DEFINITION
C_{n_r}	rad^{-1}	Yaw Damping Derivative
C_{L_α}	rad^{-1}	Lift Curve Slope
M_q	sec^{-1}	Pitch Damping
$M_{\dot{\alpha}}$	sec^{-1}	Plunge Damping
L_p	sec^{-1}	Roll Damping
N_r	sec^{-1}	Yaw Damping
N_{yF}	non-dim.	Number of fans imposing yawing moments
Y_F	ft	Yaw arm of yaw fan
$\dot{M}_{yF}$	sl/sec	Mass flow rate of yaw fan
N_{XF}	non-dim.	Number of fans imposing pitching moments
X_F	ft	Pitch arm of pitch fan
$\dot{M}_{XF}$	sl/sec	Mass flow rate of pitch fan
$\dot{M}_F$	sl/sec	Mass flow rate of main fan

BLANK PAGE

SECTION I

INTRODUCTION AND SUMMARY

In recognition of the need for improved crew safety, the Air Force Flight Dynamics Laboratory awarded an eleven month study contract to LTV Aerospace Corporation in April, 1969, with the objective to derive an analytical preliminary design of an ejection seat escape system that would be capable of providing safe crew escape from fighter/close support VTOL aircraft during emergencies in the VTOL and the low altitude, high speed flight regimes.

To ensure an optimum design, it was stipulated that detailed quantitative requirements upon which to base an escape system design must be established. A primary consideration in establishing such design specifications is the determination of the crew station environment resulting from the wide range of failures peculiar to VTOL vehicles. Additionally, since VTOL aircraft fly most of the time in conventional configuration, the high speed failure dynamics must be known. This information is attainable only through an accurate simulation of the aircraft. A failure mode analysis has been done to provide data for the ejection seat escape system and is the subject of this report.

The failure mode portion of the study has as its objectives the following:

- Select a hypothetical aircraft as a basis for escape system preliminary design.
- Establish the failure modes which influence the escape system concept.
- Provide a post failure aircraft dynamic simulation for use in preliminary design of the escape system.

A high performance aircraft was to be selected which by definition eliminates helicopters and propeller powered aircraft from consideration. The characteristics of candidate aircraft are selected from existing turbojet direct-lift and lift fan types or power system arrangements which have potential for application in the future. The objective of the selection has been to define a two place aircraft configuration which would provide the most difficult escape environment within the limits of prudent aircraft design.

The modes of failure most important to the VTOL escape system design are those which produce environments different from conventional aircraft or not provided for by current escape design specifications. The probable frequency of failure was not considered in mode selection. To obviate the design of an obsolescent escape seat system, the performance of existing VTOL designs was extrapolated to the expected level of the next generation aircraft. To exclude the possibility of a non-optimum design, the extrapolation was based on data available for present VTOL designs. The extrapolated VTOL configuration simulated with this philosophy will be called a

"hypothetical" aircraft.

After screening of the possible propulsion and configuration characteristics for which adequate simulation data were available, four aircraft with distinctly different propulsion and control traits were selected for evaluation. An abbreviated failure mode analysis was done for each aircraft using a one-degree-of-freedom analysis technique. The most severe failure environments were the only ones considered in making the selection of a hypothetical aircraft. From these four candidates, a lift fan configuration (XV-5A) was chosen as the basis for the hypothetical aircraft, the criterion being to program a flexible simulation which would impose the severest crew station emergency environment. In addition, the aerodynamic data were required to be in a form amenable to simulation of both VTOL and conventional configurations.

A six degree-of-freedom computer simulation was constructed to perform a more detailed analysis of the hypothetical aircraft for use in the preliminary design of the escape system. Mode of failures to be analyzed were selected such that the escape environments beyond those provided for by current specifications would be systematically explored. Time histories of these failures are presented in Appendix II and summary plots are discussed in Section III.

The airplane simulation was programmed to maintain generality and the fan aerodynamic computations were all programmed in one subroutine; consequently, the program can be used to represent any airplane employing any propulsion and control concept in both VTOL and conventional flight. The airplane geometry and engine data were also adjusted to allow supersonic flight up to mach 2.0 for evaluation of high speed escape in addition to the VTOL mode.

A special control subroutine was incorporated in the computer program to enable the synthesis of any conceivable emergency or combination of emergencies requiring crew escape. The sequence of events subsequent to escape initiation is plotted automatically, portraying the aircraft and crew station positions, rates and accelerations. With this information, the acceptibility of any escape concept is revealed and parameter adjustments implemented where needed.

The computer routines which make up the aircraft simulation will be documented in the Volume 3 report to be released later as indicated in the Foreword of this report.

SECTION II

TECHNICAL APPROACH AND SUMMARY

The determination of the operating limits established by evaluation of the emergency environment is fundamental to the design of any escape seat system. A primary objective of this study is to define these operating limits for a high performance VTOL aircraft with a flight envelope encompassing the airspeed range from hover to Mach 2.0 and the altitude boundary between sea level and 50,000 feet. This escape system envelope showing the failure investigation flight conditions is presented below.

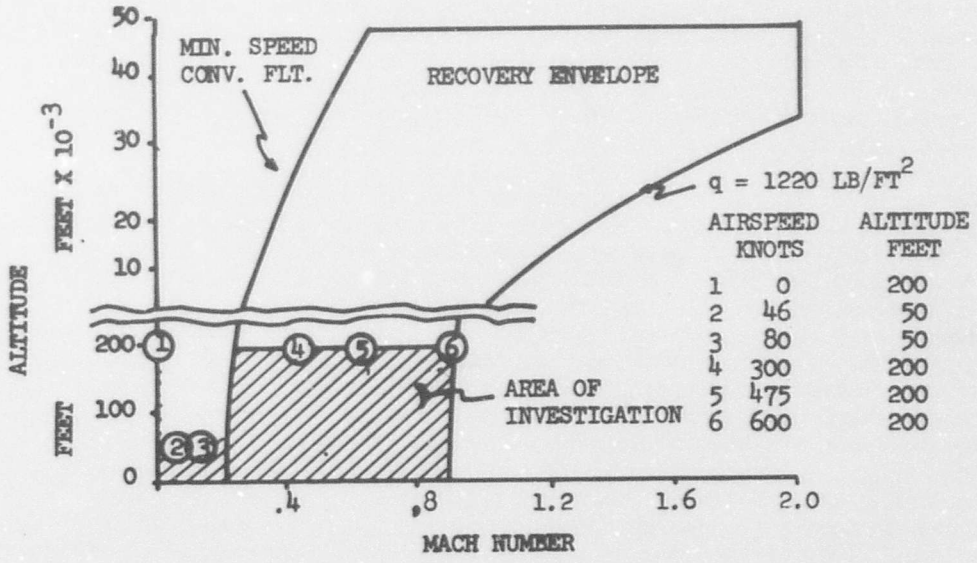

	AIRSPEED KNOTS	ALTITUDE FEET
1	0	200
2	46	50
3	80	50
4	300	200
5	475	200
6	600	200

The failure mode analysis investigation was confined to low altitude flight conditions where VTOL failures and conventional flight failures would result in the most rapid airplane response and accelerations. The remainder of the recovery envelope affects the recovery systems and is addressed in Volume 2.

The complexity inherent in the analysis of a system constructed with these versatile capabilities dictates the use of a computer simulation programmed with sufficient detail to enable the corroboration of any design concept. The computer routine written for this purpose constitutes Volume 3 of Part I "Computer Program Users Manual for VTOL Escape System Simulation." The data contained in this report were computed from the airplane option section of this computer program. Time histories of acceleration, rate and position of the airplane, and crew station reactions to a variety of deterministic aircraft failure modes were generated and plotted.

The modes of failure most important to the VTOL escape system design are those which produce environments different from conventional aircraft or are neglected by current escape design specifications. The probable frequency of failure was not considered in mode selection. To obviate the design of an obsolescent escape seat system, the performance of existing VTOL designs was extrapolated to the expected level of the next generation aircraft. To exclude the possibility of a non-optimum design, the extrapolation was based on data available for present VTOL designs. The extrapolated VTOL configuration simulated with this philosophy will be called a "hypothetical" aircraft.

After screening of the possible propulsion and configuration characteristics for which adequate simulation data were available, four aircraft with distinctly different propulsion and control traits were selected for evaluation. An abbreviated failure mode analysis was done for each aircraft using a one degree-of-freedom analysis technique. The most severe failure environments were the only ones considered in making the selection of a hypothetical aircraft. From these four candidates, a lift fan configuration was chosen as the basis for the hypothetical aircraft, the criterion being to program a flexible simulation which would impose the severest crew station emergency environment.

The necessity for computing the aerodynamic forces and moments in both VTOL and conventional flight regimes suggested the use of slipstream dynamic pressure, q_s, to surmount computational difficulties intrinsic in the use of ambient dynamic pressures in hovering and transition flight simulations. The airplane simulation was programmed to maintain generality and the fan aerodynamic computations were all programmed in one subroutine; consequently, the program can be used to represent any airplane employing any propulsion and control concept in both VTOL and conventional flight. The airplane geometry and engine data were also adjusted to allow supersonic flight up to Mach 2.0 for evaluation of high speed escape in addition to the VTOL mode.

A special control subroutine was incorporated in the computer program to enable the synthesis of any conceivable emergency or combination of emergencies requiring crew escape. The sequence of events subsequent to escape initiation is plotted automatically, portraying the aircraft and crew station positions, rates and accelerations. With this information, the acceptability of any escape concept is revealed and parameter adjustments are implemented where needed.

Using the computer simulation, a detailed analysis was performed on the hypothetical aircraft for use in the design of the escape system. Modes of failures to be analyzed were selected such that the escape environments beyond those provided for by current specifications would be systematically explored. Time histories of these failures are presented in Appendix II, and summary plots are discussed in Section IV.

The most critical failures in terms of airplane attitude or acceleration were found to result from:

o Hard-over roll control failure at 46 knots	90 degrees bank angle in .9 seconds

o Hard-over pitch control failure at 46 knots	90 degrees pitch angle in 1.4 seconds
o Hard-over longitudinal control failure at 600 knots	9.0 "g" in less than 0.1 seconds
	90 degrees pitch attitude in 1.4 seconds
o Hard-over lateral control failure at 600 knots	90 degrees roll attitude in .7 seconds
o Loss of horizontal stabilizer	9 "g" in .4 seconds
o Loss of vertical and horizontal stabilizer	9 "g" in .15 seconds

(Page 6 is blank)

BLANK PAGE

SECTION III

VTOL VEHICLE SELECTION

1. Candidate Aircraft

In designing an emergency escape system from a totally analytical foundation, it is important that a conservative philosophy be employed in choosing a hypothetical vehicle to test the feasibility of the myriad of escape concepts that must be evaluated in the preliminary design phase. For this study, the simulated airplane was synthesized from four aircraft, which are representative of future VTOL fighter-attack configurations, employing dissimilar propulsion and control system concepts.

Sketches of the four configurations, the fan-in-wing GE-Ryan XV-5A, the direct lift Lockheed XV-4B, the vectored thrust Hawker-Siddeley P-1127, and the propulsive wing VAD ADAM III together with pertinent geometrical data are shown in Figures 1 through 4. A brief description of those VTOL aircraft is included below:

a. XV-5A (Fan in Wing)

The XV-5A is a twin engine, tri-fan (two wing fans and a pitch control nose fan), tricycle-gear, mid-wing, turbojet-powered research aircraft. The hover lift is produced by diverting the engines (J-85-5B) exhaust gases through crossover ducts to drive the two wing fans and single nose fan. Pitch trim and control is provided by deflection of the pitch fan exit doors. Wing fan louvers are deflected in various combinations to produce height control, yaw control, roll control, and forward propulsion.

b. XV-4B (Hummingbird)

The XV-4B "Hummingbird" utilizes six General Electric YJ85-19 engines; four are vertically-mounted as lift units and two are horizontally-mounted for either lift or forward propulsion. The use of the latter engines for either the lift or cruise flight modes is accomplished through a diverter valve mechanism. Control in the VTOL flight mode is obtained by ducting compressor bleed air from the six J85 engines through four visor-type reaction control valves located at the extreme fore and aft ends of the fuselage and at each wing tip. Additional flexibility in flight-path and attitude control is obtained by vectoring the engine thrust with six fuselage-mounted swivel nozzles.

c. XV-6A (P-1127)

The XV-6A is powered by a two-spool, axial flow, Bristol-Siddeley Pegasus 5 turbofan engine. The aircraft is supported in the hover mode of flight on four "legs" of high velocity exhaust gas discharging from nozzles located around the aircraft center of gravity.

The forward nozzles exhaust "cold" air from the three-stage forward fan, while the two rear nozzles discharge turbine exhaust. The four nozzles are mechanically inter-connected to operate in unison and vector the engine thrust from zero degrees aft (conventional flight) to 13 degrees forward of the vertical (rearward flight). Control in hover and low speed flight is accomplished with reaction jets located at the fore and aft ends of the fuselage and at the wing tips.

d. ADAM III

The ADAM III (propulsive wing) V/STOL aircraft is being developed by VAD. Several wind tunnel models of the propulsive wing concept have been built and tested, but at this time no flight test experience has been gained. The ADAM III configuration consists of two turbojet gas generators with cross ducting to four wing fans and a forward fuselage nose pitch fan. The turbojet "hot" gases are ejected through the wing fan turbines and exhausted over the flaps in a downward direction. The wing fan turbines drive axial flow compressors which inject "cold" air through the wing leading edge inlet. The "cold" air is turned by means of vane boxes to provide thrust vectoring. Lateral and directional control in hover and low speed transition range would be provided by differential (left and right wings) fan RPM, vane box exit area throttling, and vane box deflections.

2. Failure Evaluation

In selecting the hypothetical aircraft, it is beyond the scope of this program to reduce the aerodynamic data for the many types of VTOL propulsion and control concepts to the form required for a complete six degree-of-freedom computer simulation. Neither is it feasible or essential to account for such intricacies as automatic control system transfer functions or system non-linearities. Therefore, for purposes of selecting critical failure configurations, single degree-of-freedom-linear equations and full hard over control system failures (100% control authorities) are used for comparing vehicle excursions following the failures.

While it is recognized that this simplified dynamic response is not representative of the true dynamics of the aircraft, the relative rates and displacements do provide a meaningful basis for selecting a configuration or composite configuration for subsequent detailed Six-DOF (Degree-of-Freedom) computer simulation. The directional axis was eliminated from this study because a distrubance about this axis in VTOL mode does not position the aircraft in a dangerous attitude relative to the ground for safe crew ejection. The following additional assumptions were also made:

- Step inputs for all types of propulsion and control system failures
- Instantaneous full available control power against an aircraft upset moment caused by an asymmetric propulsion system failure

- Propulsion system contribution to angular rate damping and vertical damping in hover were based on the simple momentum theory, $\dot{m}\ \Delta V$ through the propulsion and control fans.

The aircraft's vertical displacement time history can be computed from the Laplace transformation of the differential equation:

$$\Delta \ddot{h} = 32.2 \left(\frac{\Delta T}{GW}\right) - 1/\tau_w\ \Delta \dot{h}$$

With an instantaneous engine failure, a step thrust change,

$$\frac{\Delta T/GW}{s}$$

results in a closed form solution of the form

$$\Delta \dot{h} = \frac{32.2 \left(\frac{\Delta T}{GW}\right)}{s\ (s + 1/\tau_w)}$$

$\Delta \dot{h}$ is the aircraft climb rate (negative sink rate), ft/sec

ΔT is the thrust loss, lb

The inverse transformation then yields:

CLIMB RATE CHANGE

$$\Delta \dot{h} = 32.17 \left(\frac{\Delta T}{GW}\right) \left[\tau_w \left[1 - e^{-t/\tau_w}\right]\right]$$

$$= 32.17 \left(\frac{\Delta T}{GW}\right) t, \quad 1/\tau_w = 0 \qquad \text{(zero heave damping)}$$

A similar development produces:

ALTITUDE CHANGE

$$\Delta h = 32.17 \left(\frac{\Delta T}{GW}\right) \left[\tau_w^2 \left[e^{-t/\tau_w} + t/\tau_w - 1\right]\right]$$

$$= 32.17 \left(\frac{\Delta T}{GW}\right) t^2/2, \quad 1/\tau_w = 0 \qquad \text{(zero heave damping)}$$

PITCH RATE CHANGE

$$\Delta\dot{\theta} = \left(\frac{\Delta TY}{Iy}\right) \left[\tau_q \left(1 - e^{-t/\tau_q}\right)\right]$$

$$= \left(\frac{\Delta TY}{Iy}\right) t, \quad 1/\tau_q = 0 \qquad \text{(zero pitch damping)}$$

PITCH ATTITUDE CHANGE

$$\Delta\theta = \left(\frac{\Delta TY}{Iy}\right) \left[\tau_q^2 \left[e^{-t/\tau_q} + t/\tau_q - 1\right]\right]$$

$$= \left(\frac{\Delta TY}{Iy}\right) t^2/2, \quad 1/\tau_q = 0 \qquad \text{(zero pitch damping)}$$

ROLL RATE CHANGE

$$\Delta\dot{\phi} = \left(\frac{\Delta TX}{Ix}\right) \left[\tau_p \left(1 - e^{-t/\tau_p}\right)\right]$$

$$= \left(\frac{\Delta TX}{Ix}\right) t, \quad 1/\tau_p = 0 \qquad \text{(zero roll damping)}$$

BANK ANGLE CHANGE

$$= \left(\frac{\Delta Tx}{Ix}\right)\left[\tau_p^2\left[e^{-t/\tau_p} + t/\tau_p - 1\right]\right]$$

$$= \left(\frac{\Delta Tx}{Ix}\right) t^2/2 , \quad 1/\tau_p = 0 \qquad \text{(zero roll damping)}$$

The time constants are functions of aerodynamic damping coefficients and damping from mass flow rate terms.

ROLL DAMPING

$$1/\tau_p = -\left(\rho \frac{V_T S b^2 C_{l_p}}{4} - N_{y_F} \dot{m}_{y_F} y_F^2\right) / Ix$$

N_{y_F} is the number of lateral mass flow generators.

y_F is the distance to the mass flow generator.

PITCH DAMPING

$$1/\tau_q = -\left(\rho \frac{V_T S \bar{c}^2}{4} C_{m_q} - N_{x_F} \dot{m}_{x_F} x_F^2\right) / Iy$$

N_{x_F} is the number of longitudinal mass flow generators.

x_F is the distance to the longitudinal mass flow generator.

HEAVE DAMPING

$$1/\tau_w = -32.2\left(\rho \frac{S \bar{c}}{4} C_{l_{\dot{\alpha}}} - \dot{m}_F\right) / GW$$

(Symbols not defined in List of Symbols, page xx, are standard names defined in Appendix I.)

Tables III contain the values for the damping parameters.

For the configurations listed on the following tables, using the base geometry of Figures 1 through 4, transfer function coefficients were calculated from aerodynamic information available in the listed references.

TABLE I

MASS AND INERTIA CHARACTERISTICS

AIRPLANE	G.W.	C.G.	I_X	I_Y
XV-5A	9200	25.6%-30.8%	4252	15,139
XV-4B	12,000	10%	3184	13,400
XV-6A	11,800	10%	3500	22,450
ADAM III	28,800	FS 345.46	17,976	81,624

TABLE II (a)

TIME CONSTANTS AND UPSETTING FORCES AND MOMENTS

CASE/FAILURE CONDITION			(a) THRUST		(b) ROLL		(c) PITCH		
CASE	FLIGHT CONDITION	AIRCRAFT	$\left(\frac{\Delta T}{GW}\right)$	$\left(\frac{1}{\tau_w}\right)$	$\left(\frac{\Delta I_X}{I_X}\right)$	$\left(\frac{1}{\tau_p}\right)$	$\left(\frac{\Delta I_Y}{I_Y}\right)$	$\left(\frac{1}{\tau_q}\right)$	REFERENCES
1	Hover	XV-5A	0.665	0.0865	5.6	0.0865	1.05	0.0747	1, 2, 3, 4, 5, 6, 7
2	|	XV-4B			2.6	0.0	1.04	0.0	8
3	|	XV-6A	1.01	0.0	1.88	0.0	-0.97	0.0	9, 10
4	|	ADAM III	0.66	0.037	2.37	0.032	-0.76	0.0	11, 12
5	Transition	XV-5A	*	*	2.95	1.485	2.8	0.6175	1, 2, 3, 4, 5, 6, 7
6	80 Knots	XV-4B	*	*	2.84	0.635	2.43	0.442	8
7	|	XV-6A	*	*	2.54	0.805	1.16	0.297	9, 10
8	|	ADAM III	*	*	*	*	*	*	11, 12

* Denotes insufficient data to conduct analysis

TABLE II (b)

FAILURE CONDITION INVESTIGATED FOR VEHICLE SELECTION

FAILURE	CASE	EXPLANATION
(a) Thrust	1	Instantaneous loss of one engine- 60% thrust available due to cross ducting
	2	Instantaneous loss of one engine- 5 engines remaining provide ample lift
	3	Instantaneous loss of one engine- Total loss of power of the single engine aircraft
	4	Instantaneous loss of one engine- 70% thrust available due to cross ducting through four wing fans
(b) Roll	1	Instantaneous loss of one wing fan
	2	Hard over roll control failure
	3	Hard over roll control failure
	4	Outboard wing fan complete failure
	5	Loss of one wing fan
	6	Lateral control system hard over failure
	7	Lateral control system hard over failure
(c) Pitch	1	Nose fan hard over failure
	2	Longitudinal control system hard over failure
	3	Longitudinal control system hard over failure
	4	Nose fan failure
	5	Nose fan hard over failure
	6	Longitudinal control system hard over failure
	7	Longitudinal control system hard over failure

TABLE III (a)

AERODYNAMIC DAMPING

AIRSPEED	AIRPLANE	Cm_q	$Cm_{\dot{\alpha}}$	C_{ℓ_p}	Cn_r	M_q	$M_{\dot{\alpha}}$	L_p	$N_{\dot{r}}$
80 Knots	XV - 5A	- 4.39	- 3.34	- .340	-1.115	-8100	-6150	-6310	-21,400
	XV - 4B	-35.40	-26.90	- .328	-1.089	-5910	-4500	-2025	-6720
	XV - 6A	- 6.71	- 5.1	- .36	-1.140	-6680	-5070	-2810	-8870
	ADAM III	*	*	*	*	*	*	*	*

TABLE III (b)

JET MOMENTUM DAMPING

AIRSPEED	AIRPLANE	$N_{Y_F}\ \dot{M}_{Y_F}\ Y^2_F$	$N_{X_F}\ \dot{M}_{X_F}\ X^2_F$	$\dot{M}_F$
80 Knots	XV - 5A	566	1264	NEG.
	XV - 4B	NEG.	NEG.	NEG.
	XV - 6A	NEG.	NEG.	NEG.
	ADAM III	*	*	*

* Denotes insufficient data to conduct analysis

3. Hypothetical Aircraft Selection

From the foregoing equations, the geometry of Figures 1 through 4, the weight and inertia data of Table I and the damping and accelerations of Table II, the time histories shown in Figures 5 through 14 were computed. Scrutiny of these time histories (a maximum excursion time of 3 seconds was assumed for calculation purposes) shows that:

- The XV-6A was the most critical VTOL configuration relative to sink rate following the loss of one engine in the hover flight mode.
- The XV-5A and XV-4B aircraft were the most critical VTOL configurations relative to longitudinal control system failures in the hover flight mode.
- The XV-5A with one complete wing fan failure and full lateral control against the upset moment was the most severe VTOL aircraft configuration evaluated relative to bank angle displacement after the failure occurred in the hover flight mode.
- At the intermediate transition velocity of 80 knots, the XV-5A was the most critical airplane evaluated relative to pitch attitude changes following a hard-over failure in the longitudinal control system.
- At the intermediate transition velocity of 80 knots, the XV-4B was the most critical airplane evaluated relative to bank angle changes following the most critical failure, per aircraft, affecting lateral control.

Heave damping and thrust data were not available for the transition 80 knot speed condition. However, since these data would primarily affect the altitude loss which is critical in hover where data are available, the vehicle selection is still valid. The absence of data for the ADAM III configuration was not crucial to vehicle selection since the failure time histories for which data were available did not reveal any outstanding excursions as compared to the other configurations.

From these observations it was concluded that the XV-5A, in general, has the worst failure characteristics. It was selected as the simulator model for the detailed 6-DOF study with adjustments in data to permit the airplane to attain the high speed and altitude envelope prescribed for the escape system. Also the single engine failure was changed to a dual engine failure to cause the XV-5A to plunge with a higher sink rate more nearly like the XV-6A following a single lift engine failure.

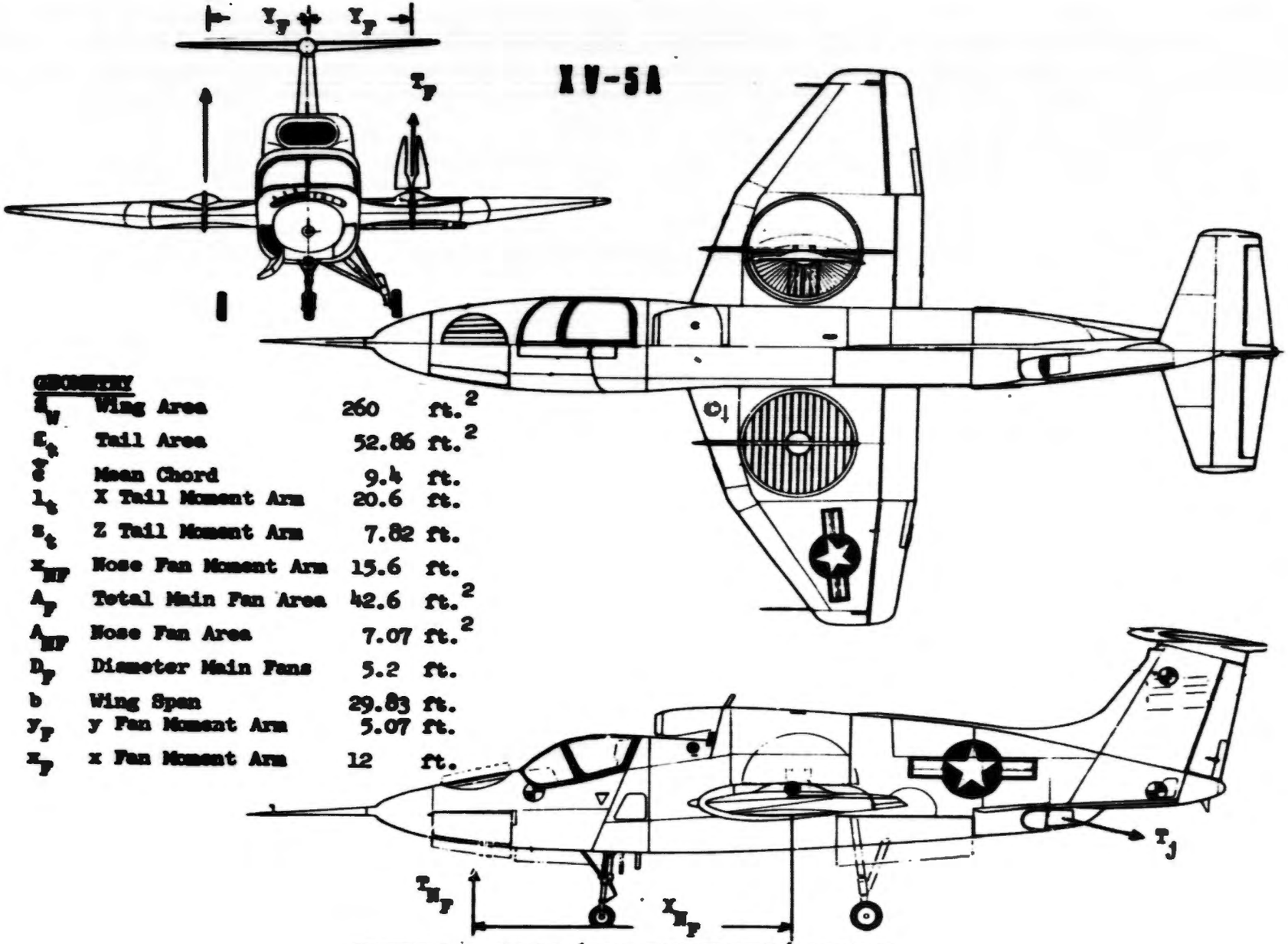

GEOMETRY

S_w	Wing Area	260	ft.^{2}
S_t	Tail Area	52.86	ft.^{2}
$\bar{c}$	Mean Chord	9.4	ft.
l_t	X Tail Moment Arm	20.6	ft.
z_t	Z Tail Moment Arm	7.82	ft.
x_{HF}	Nose Fan Moment Arm	15.6	ft.
A_p	Total Main Fan Area	42.6	ft.^{2}
A_{HF}	Nose Fan Area	7.07	ft.^{2}
D_p	Diameter Main Fans	5.2	ft.
b	Wing Span	29.83	ft.
y_p	y Fan Moment Arm	5.07	ft.
x_p	x Fan Moment Arm	12	ft.

FIGURE 1 XV-5A (RYAN FAN-IN-WING) DRAWING

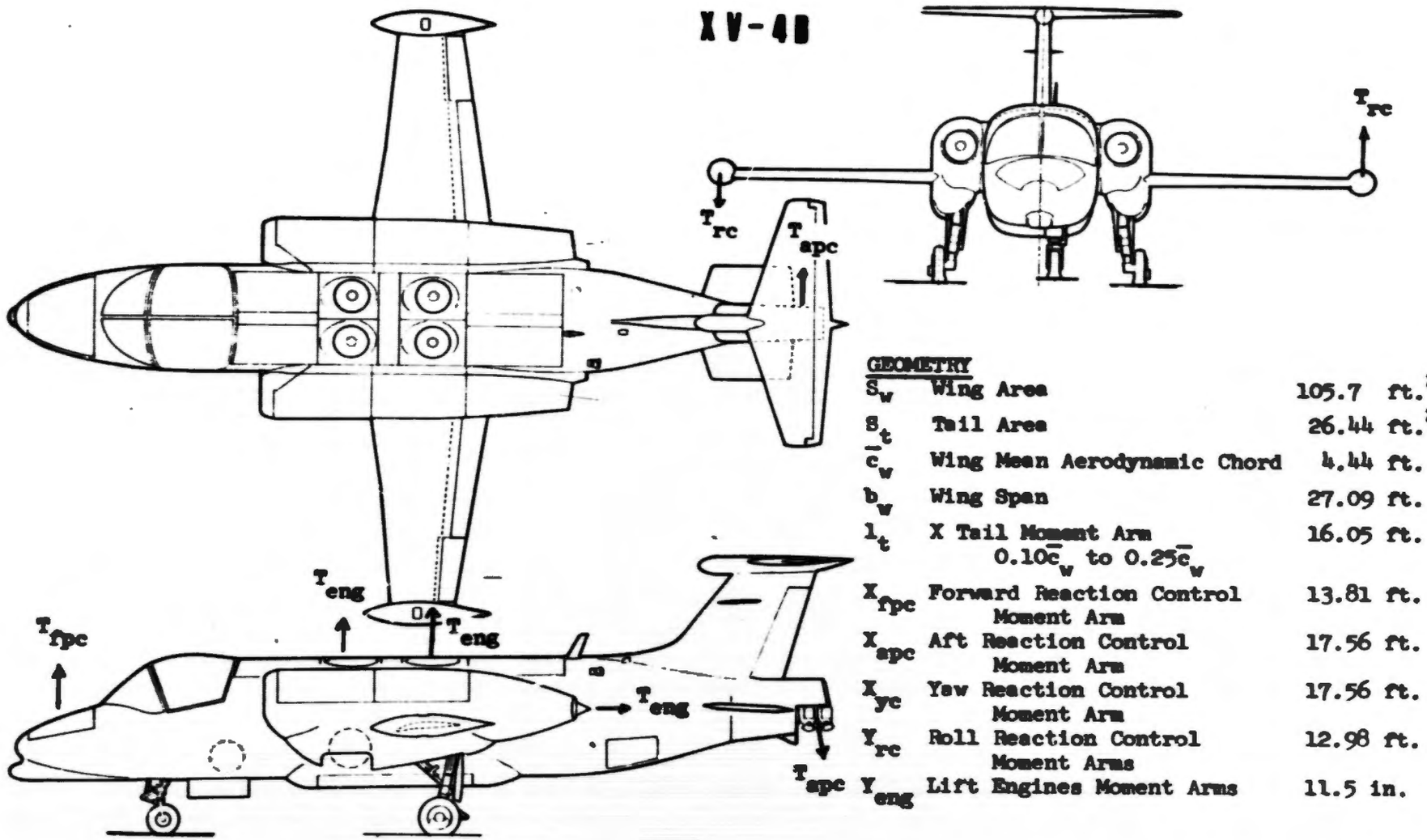

GEOMETRY		
S_w	Wing Area	105.7 ft.^{2}
S_t	Tail Area	26.44 ft.^{2}
$\bar{c}_w$	Wing Mean Aerodynamic Chord	4.44 ft.
b_w	Wing Span	27.09 ft.
l_t	X Tail Moment Arm $0.10\bar{c}_w$ to $0.25\bar{c}_w$	16.05 ft.
X_{fpc}	Forward Reaction Control Moment Arm	13.81 ft.
X_{apc}	Aft Reaction Control Moment Arm	17.56 ft.
X_{yc}	Yaw Reaction Control Moment Arm	17.56 ft.
Y_{rc}	Roll Reaction Control Moment Arms	12.98 ft.
Y_{eng}	Lift Engines Moment Arms	11.5 in.

FIGURE 2 XV-4B (LOCKHEED "HUMMINGBIRD") DRAWING

GEOMETRY

S_w	Wing Area	186.4 ft.^{2}
S_t	Tail Area	47.5 ft.^{2}
$\bar{c}_w$	Wing Mean Aerodynamic Chord	8.15 ft.
b_w	Wing Span	22.82 ft.
l_t	X Tail Moment Arm	16.70 ft.

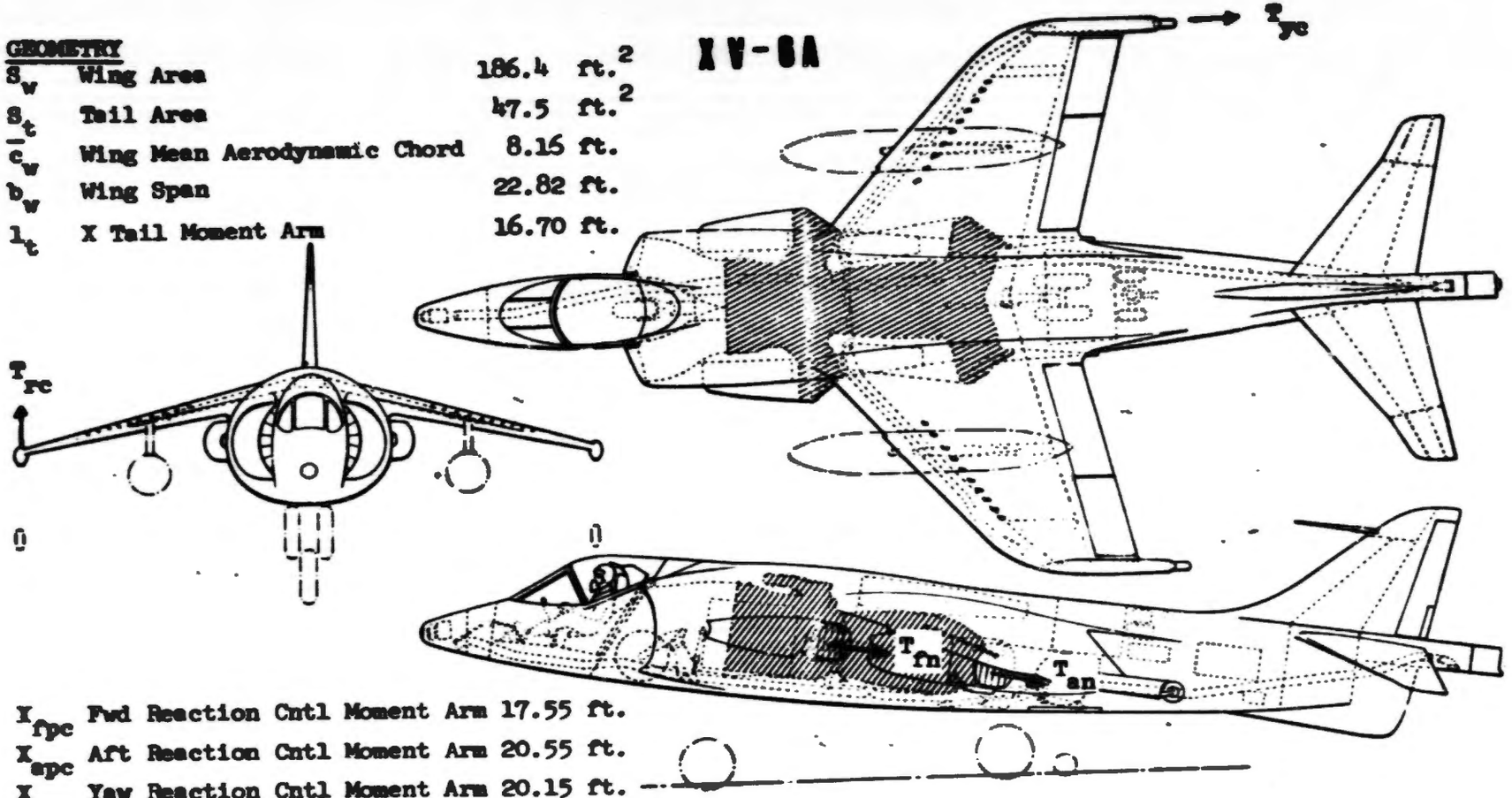

X_{fpc}	Fwd Reaction Cntl Moment Arm	17.55 ft.
X_{apc}	Aft Reaction Cntl Moment Arm	20.55 ft.
X_{yc}	Yaw Reaction Cntl Moment Arm	20.15 ft.
Y_{rc}	Roll Reaction Cntl Mom. Arms	11.2 ft.
Y_{fn}	Fwd Eng "Cold" Flow Nozzle Moment Arm	3.4 ft.
Y_{an}	Aft Eng Exhaust Flow Nozzle Moment Arm	2.61 ft.

FIGURE 3 XV-6A (HAWKER-SIDDELEY P-1127 "HARRIER") DRAWING

ADAM III

GEOMETRY

S_w	Wing Area	376.0 ft.^{2}
S_t	Tail Area	(Included in Wing Area)
b_w	Wing Span	34.33 ft.
X_{nf}	Nose Fan Moment Arm	11.7 ft.
A_{wf}	Total Wing Fan Area	22.0 ft.^{2}
A_{nf}	Nose Fan Area	10.16 ft.^{2}
D_{wf}	Diameter Wing Fan	2.65 ft.
D_{nf}	Diameter Nose Fan	3.6 ft.
Y_{if}	Inboard Wing Fan Moment Arm	5.0 ft.
Y_{of}	Outboard Wing Fan Moment Arm	8.45 ft.

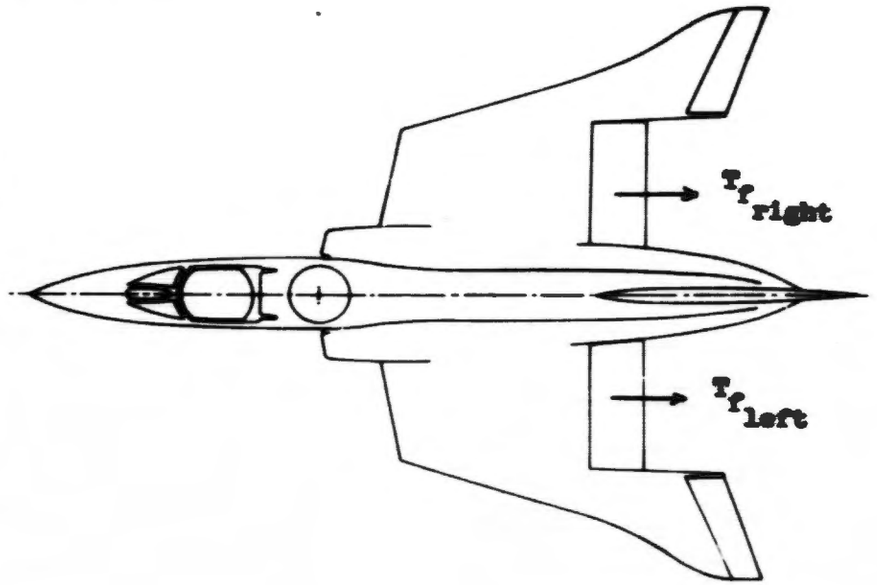

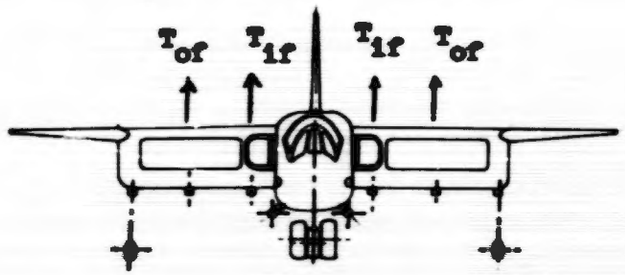

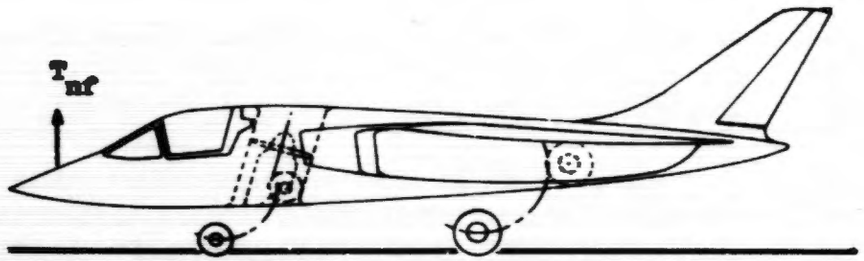

FIGURE 4 ADAM III (LTV PROPULSIVE WING) DRAWING

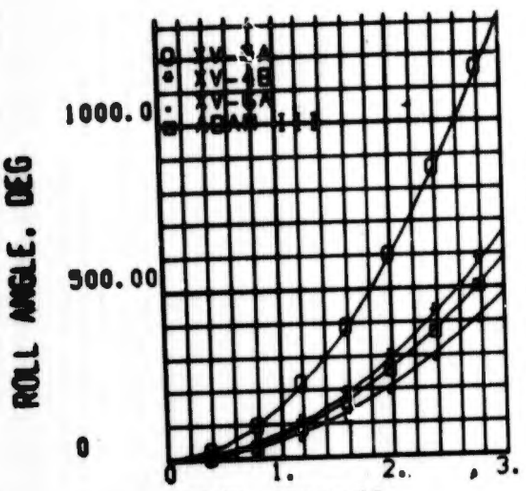

FIG 5 ROLLING MOMENT FAILURES
ROLL ANGLE FROM INITIAL HOVER

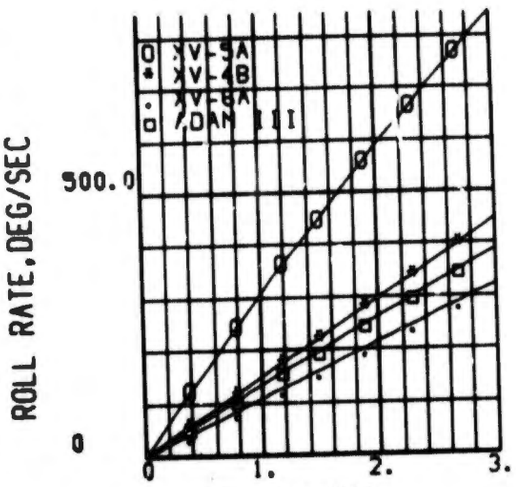

FIG 6 ROLLING MOMENT FAILURES
ROLL RATE FROM INITIAL HOVER

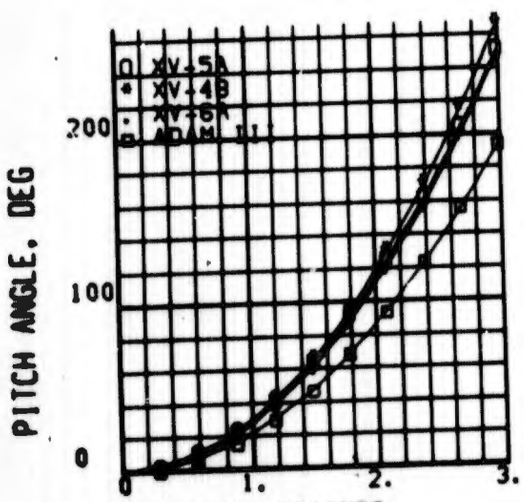

FIG 7 PITCHING MOMENT FAILURES
PITCH ANGLE FROM INITIAL HOVER

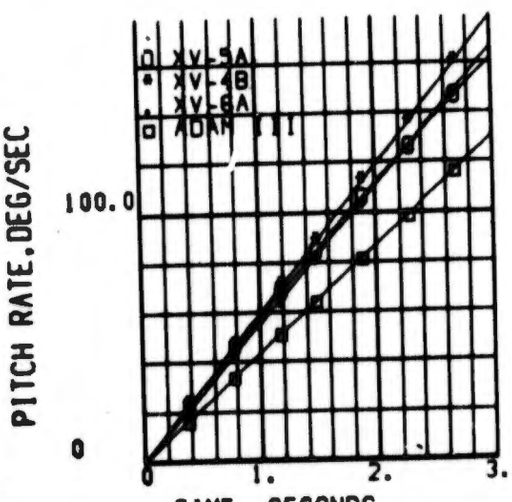

FIG 8 PITCHING MOMENT FAILURES
PITCH RATE FROM INITIAL HOVER

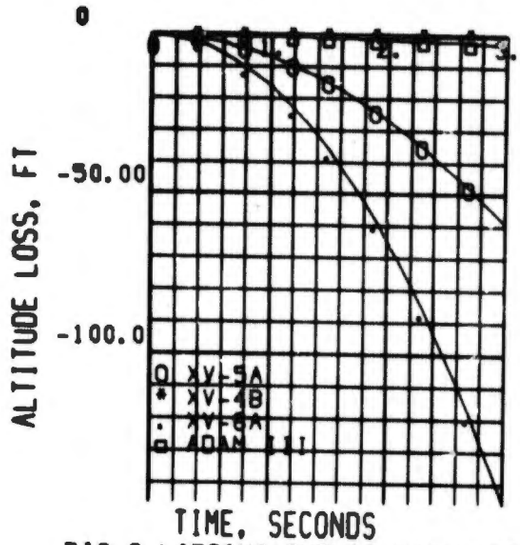

FIG 9 LIFTING THRUST FAILURES
ALTITUDE LOSS FROM HOVER

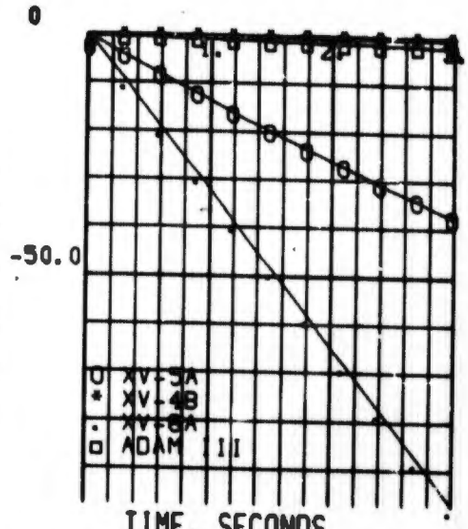

FIG 10 LIFTING THRUST FAILURES
CLIMB RATE CHANGE FROM HOVER

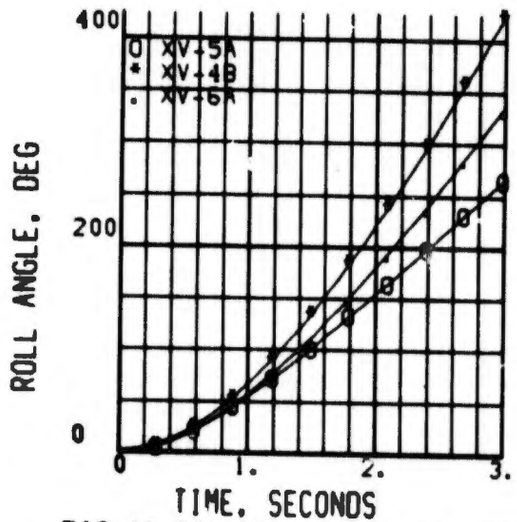

FIG 11 ROLLING MOMENT FAILURES
ROLL ANGLE AT 80 KNOTS

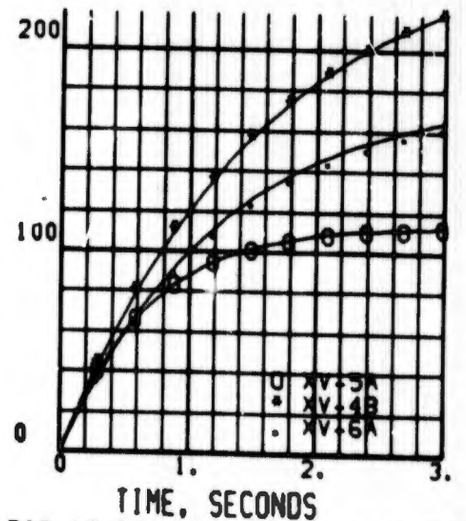

FIG 12 ROLLING MOMENT FAILURES
ROLL RATE AT 80 KNOTS

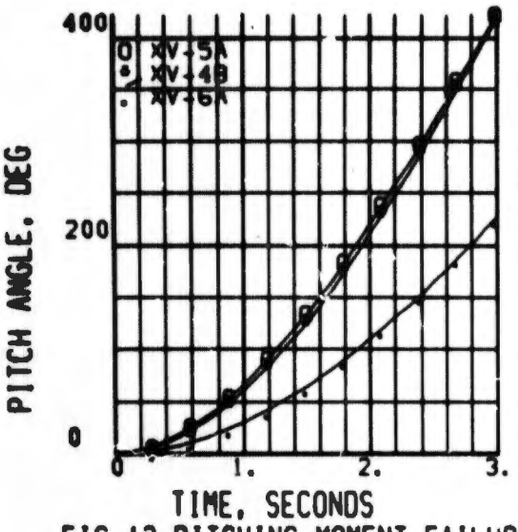

FIG 13 PITCHING MOMENT FAILURE
PITCH ANGLE AT 80 KNOTS

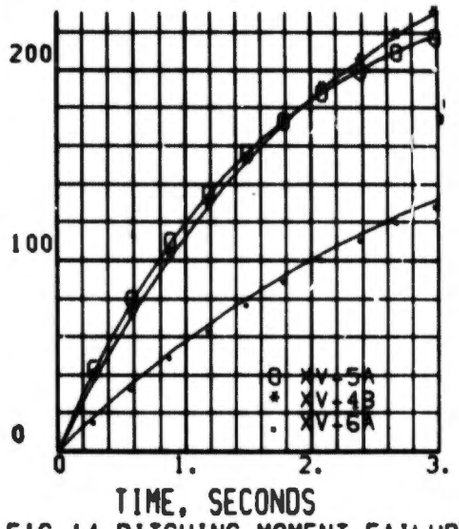

FIG 14 PITCHING MOMENT FAILURE
PITCH RATE AT 80 KNOTS

SECTION IV

FAILURE MODE ANALYSIS

The failure modes discussed in this section are summarized from aircraft and cockpit acceleration, rate and position post-failure time histories similar to those of Appendix II. A six degree-of-freedom digital computer simulation was employed in which the equations of Appendix I were programmed. The primary objective is to define those escape system operating limits for the hypothetical aircraft selected in Section III.

The most severe failure consequences occur with an instantaneous failure initiated at the level of the primary forcing function with no pilot corrective action being taken. For example, a horizontal tail hard-over command could result from many malfunctions beginning with the pilot or autopilot and progressing through the control system to the final servo linkage. The aircraft responds only to the change in tail incidence, however, and this is considered to be the primary forcing function; i.e., only the results of failures not the causes are considered.

Since conventional aerodynamic controls are ineffective in VTOL flight, only VTOL control system failures were considered for the VTOL flight mode. Longitudinally, the pitching moment from the nose fan far exceeded the wing fan pitching moments and was the obvious choice for longitudinal failure inputs. Roll control, mechanized by staggering the wing fan louvers to vary the mass flow rate, was more critical than wing fan yaw vectoring because of the rapidity with which the airplane became inverted. All VTOL controls and lift are dependent upon outputs from the propulsion system, necessitating the analysis of full propulsion failures for lift loss and partial propulsion failures for control loss coupling (operable VTOL controls do not exist during a full propulsion failure). From all these considerations, seven critical failure modes listed below were selected and are discussed in Section IV-1.

- o complete propulsion failure
- o partial propulsion
- o hardover lateral control failure
- o partial propulsion failure with lateral control failure
- o hard-over longitudinal control failure
- o partial propulsion failure with longitudinal control failure
- o partial propulsion failure with longitudinal and lateral control failure

In conventional flight, at the level of the primary forcing function, the variable incidence horizontal tail was the logical choice for hard-over control failures because of the high pitch effectiveness relative to elevator control. The choice of a lateral control failure over a directional control failure was dictated by the high roll rates resulting from a lateral control failure as compared to the rates produced by a directional control failure. Structural failures resulting in loss of horizontal stabilizer, wing and horizontal and vertical stabilizer were also considered. Other structural failures, such as elevator destruction or partial stabilizer loss, result in lower loads than a full failure; however, because of the roll rates developed, loss of one side of a wing proved to be more serious than complete wing loss. From this reasoning, the five conventional flight failure modes listed below and discussed in Section IV-2 were investigated at an airspeed of 600 knots at 200 feet altitude.

- o hard-over longitudinal control failure
- o hard-over lateral control failure
- o wing structural failure
- o loss of horizontal stabilizer
- o loss of vertical and horizontal stabilizers

Limit load factors for contemporary fighter and attack aircraft are generally in the range of 6.4 to 7.5 "g". Realizing that a VTOL fighter/attack configuration would probably compromise high load factor capability in the interest of weight saving, a limit load factor of 6.0 "g" was assumed. For those conditions where wing structural failure could occur prior to large angular excursions an ultimate load factor of 9.0 "g" (1.5 x 6.0 "g") was used.

1. VTOL And Transition Failures

In the VTOL configuration the airplane stability and control is dependent almost exclusively upon control of propulsion vectoring devices; consequently, the failure modes were selected to reflect this dependency. In addition to control failures, the loss of lifting propulsion has obviously serious consequences for VTOL modes and the effects of single and dual engine failures were investigated.

To ascertain the airspeed at which the most dangerous failures occur, several time histories were run for airspeeds from hovering flight to transition flight. Figures 15 through 46 summarize these time histories, showing the maximum excursions of those variables that significantly affect crew recovery. At such low speeds, crew load factors proved to be small as would be expected and were not cross-plotted. Airplane attitude changes, however, would demand recovery control to prevent earthward ejection of the crew as the airplane rolled or pitched toward an inverted attitude. Altitude losses in all cases were unimportant compared to the attitude changes.

The maximum values are plotted at three typically critical points in time. At 0.15 seconds, the failure would probably have been identified and escape sequencing initiated. By 0.3 seconds the catapult would have fired and the seat would have travelled up (or down) the rails to a position near tip-off. At 0.5 seconds the seat would probably be near the limit of collision with some part of the airplane, such as the vertical tail or wing tip.

The complete time histories from which the hover and 46 knots data were extracted are given by Figures 93 through 190. The 46 knot time histories were chosen for presentation over the 80 knot case because it produced the larger excursions in pitch and roll attitudes. Forty-six knots is the airspeed at which the fan jet momentum control forces begin to phase out as aerodynamic controls start to become effective.

a. Propulsion Failure - Both Engines Out

The malfunctioning of a single engine in a fan-in-wing vehicle imposes no stringent demands upon an escape system because more than half the two engine

lifting thrust remains and destabilizing asymmetrical control forces are obviated by cross ducting design. But total loss of all engine power, however unlikely in a dual engine design, may be envisaged for the purpose of designing an escape system for those aircraft having only one engine. Figures 15 through 18 portray the changes in the most significant escape system parameters resulting from total loss of power while in the VTOL configuration.

In both hovering and transition engine failures, the airplane evidences a pitch-down tendency because of the cessation of upwash on the wing from the lift-fans. Figure 17 shows that this pitch-down characteristic becomes more pronounced at higher speeds because of the increase of horizontal tail effectiveness at higher dynamic pressures; however, the magnitude is too small to constitute a hazard to crew recovery and the rate, Figure 18, is low enough to allow sufficient time for failure identification and escape initiation.

b. Propulsion Failure - Single Engine Out

Figures 19 through 22 show the variation of critical escape parameters when a single engine fails, reducing the gas generator effectiveness by 40%. Point by point comparison with Figures 15 through 18 shows that this failure is naturally less serious than the dual engine failure. It is included here for later comparison with control failures occurring during a single engine malfunction.

c. Hard-Over Lateral Control Failure

The ingestion of a large, solid object through a wing duct would obliterate the turbine blades, causing both a lift loss and catastrophic control coupling in the lateral-directional and longitudinal degrees of freedom. Figures 23 through 26 delineate the consequences of an abrupt and total loss of life from the right wing fan with no compensating inputs from the left louver vanes. The hovering maneuver is seen to be less critical than the transition maneuver as is evident in Figure 25 which shows a 23% increase in bank angle at 46 knots and in Figure 26 which shows a 17% increase in roll rate at 46 knots.

As in most VTOL emergencies, the attitude changes predominate over translational excursions and the bank angle, Figure 25, is the significant parameter in this failure mode. With such a rapid increase in bank angle at the 46 knot failure initiation, the airplane has reached the critical 90° in 0.9 sec. with a roll rate of 2.7 rad/sec (Appendix II, Figures 140 and 143), and a conventional escape system must have completed seat separation or programmed an ejection delay until 1.6 seconds when the airplane has rolled to a safe recovery attitude of 270 degrees; i.e., safe ejection could be accomplished only between bank angles of $\pm$90 degrees.

d. Partial Propulsion Failure with Lateral Control Failure

Figures 27 through 32 show that this failure combination is less severe than the single lateral control failure. This demonstrates anew that VTOL control effectiveness is dependent primarily upon propulsion magnitudes.

The bank angle, Figure 29, is less for the single engine hard-over malfunction than for the hard-over failure with full power available, Figure 25. In Appendix II, Figures 159 and 162, the bank angle requires 1.4 seconds to roll to 90 degrees at which time the roll rate is 1.5 rad/sec -- about half the roll rate from the lateral control failure alone.

e. Hard-Over Longitudinal Control Failure

Pitch control in VTOL flight is mechanized through nose fan doors, or buckets, which divert the gas efflux from the ducted nose fan. Pitch-down control power from the nose fan is limited by design in the XV-5A and the hypothetical vehicle to approximately 20% of the nose up control power a magnitude only slightly in excess of that required to trim. In contrast, enough pitch-up effectiveness is available to constitute a possibly serious hard-over failure.

Figures 33 through 36 are summary plots from Appendix II showing the effects of hard-over failure in hover and transition. Figures 115 through 152 demonstrate the effects of a full pitch-up moment from the nose fan. Figure 119 is a graph of the pitch attitude showing how quickly the airplane becomes inverted as a consequence of this failure. Unlike a conventional aerodynamic control, the pitch fan maintains sufficient angular acceleration to invert the aircraft, even from hover, in about 2.4 seconds.

In aircraft having equal nose-down and nose-up control powers, there would be essentially no difference in the magnitude of nose fan induced angular excursions for the hover and 46 knot case. Also, for the time intervals of interest, altitude change following a nose up or nose down failure would be only slightly affected since the nose fan force is small relative to the total propulsion lifting force. Hence, the time histories for nose fan failures causing a nose-up moment can be treated as a nose down moment with a corresponding sign change in pitch attitude and rate.

f. Partial Propulsion Failure with Longitudinal Control Failure

With only 60% of the thrust available for control power through the nose fan, a full nose up pitching moment failure is less hazardous than the same failure with full available trim thrust. Figures 37 through 40 (reduced from Figures 153 through 190) show the pitch attitude and pitch rate to be little more than half the values for the same control malfunction with full trim power.

g. Partial Propulsion Failure with Longitudinal and Lateral Control Failures

The effects of coupled failures in lift propulsion, hard-over roll control and fully open pitch fan buckets are seen in Figures 41 through 46. By comparing these figures with those for single control failures, it can be established that a dual control malfunction results in escape conditions that are less dangerous than single control failures. This is because the upsetting moment which becomes greater for a single roll failure than for simultaneous roll-pitch inputs, positions the aircraft more rapidly in the inverted position.

Comparison of Figure 29 with Figure 45 reveals that the bank angles are nearly identical for the first half second but, soon after, increase faster for the single lateral control failure. For three simultaneous failures at 46 knots, for example, the airplane is inverted in about 3.0 seconds while requiring only about 1.6 seconds for the double failures (Figure 178). The pitch attitude, after an initial inertially stabilizing pitch-up for the triple failure stays about the same order of magnitude for both types of failures (Figure 176). A triple failure with a hard-over, nose-down pitching moment is inertially destabilizing and would be the worst failure possible, if realizable.

2. Conventional Flight Failure Modes

Structural failures and excessive aerodynamic control inputs are the emergencies simulated in the conventional flight regime. Figures 191 through 226, Appendix II, are time history plots depicting the consequences of the five kinds of emergencies considered to be the most hazardous at low altitudes under high dynamic pressure. The summary plots in this section include crew station load factors, which were inconsequential in the low speed emergencies.

To permit the supersonic speeds required for the ejection seat design envelope, the XV-5A data were modified for speeds to Mach 2.0. The wing-body axial drag coefficients (Appendix I) were reduced to reflect a thinner wing mechanizable by telescoping fan ducts and/or higher aspect ratio fan blades operating at lower RPM. Further drag reduction was assumed to be realizable by construction of a smaller horizontal tail. A 20% increase in available thrust was also hypothesized.

a. Hard-Over Longitudinal Control Failure

The airplane flying at 600 knots at a 200 foot altitude will respond to limit horizontal tail inputs with excessive load factors which integrate rapidly to dangerous airplane attitudes such that aircraft spatial orientation with respect to the earth may preclude safe crew escape. Figures 47 through 50 reveal the serious consequences of a full trailing-edge-down horizontal tail failure.

The time history, Figures 191 through 209, Appendix II, was run with a step horizontal tail. A conservative 30% loss in control power due to aeroelasticity was assumed based on A-7 aircraft experience. Assuming an ultimate load factor of 9.0 "g" based on a limit load factor of 6.0 "g", the wings would fail structurally in less than 0.1 seconds.

b. Hard-Over Lateral Control Failure

Figures 51 through 54 show the demands imposed on any escape system when the roll control surfaces are driven instantaneously to the limits at high speeds.

The bank angle, Figure 51, at the 600 knot condition has already reached 64° at the end of half a second, and the complete time history, Figure 197, shows that the airplane is inverted at 1.3 seconds and that

ejection through the canopy would propel the seat toward the earth during the time interval between 0.7 and 1.9 seconds.

A 20% loss in lateral control effectiveness due to aeroelasticity was assumed, in contrast to approximately 25% for a conventional fighter/attack aircraft based on A-7 aircraft experience for example.

c. Loss of Horizontal Stabilizer

A fighter/close support VTOL aircraft will be exposed to battle conditions which can compromise its structural integrity and result in loss of the horizontal tail. Time history plots, Figures 210 through 228, portray the results of such an emergency. After 0.9 sec. the airplane is inverted (Figure 214).

This emergency was simulated by setting the horizontal tail reference area to zero and reducing the horizontal tail pitch damping to zero at time history initiation. An initial condition of 6.0 G's occurring in level flight following dive recovery was assumed for this failure study.

d. Wing Structural Failure

The loss of the complete right half wing in high speed flight is simulated through estimates of the lateral c.g. shift, weight and inertia changes, and by assessments of the variation of static and dynamic aerodynamic coefficients. (With the right half and left half wing aerodynamics being simulated independently, this type of failure is easily accomplished by nulling the dynamic pressure for one wing half.)

Figures 211 through 228 show that the airplane responds to this failure very nearly as if full lateral control had been applied to the airplane, with no wing failure. The roll rate, Figure 219, oscillates slightly about 2.3 rad/sec. The load factors at the cockpit c.g. represented by Figures 226, 227, and 228 reveal that the accelerations at that point are not excessive, mainly because the cockpit c.g. location is very close to the roll axis of the airplane.

At time history initiation, the airplane was assumed to have a horizontal tail position which would impose a 6.0 G normal load factor and the time history was then begun with the right wing dynamic pressure nulled. (The smaller normal load factor, Figure 224, reflects the instantaneous loss of one wing half). Stabilizing inertial coupling results from the positive pitch rate corresponding to the positive load factor (Figure 217).

e. Loss of Vertical and Horizontal Stabilizers

Because of the T-tail configuration, both horizontal and vertical stabilizers will be lost if the vertical stabilizer suffers complete structural failure. Figures 210 through 228 are time histories generated through the assumption of total loss of both stabilizing surfaces. Weight, inertia, and c.g changes were estimated, the horizontal tail reference area was set to zero in the computer simulation, tail pitch and yaw damping were nulled, and the lateral-directional aerodynamic coefficients were shifted to the tail-off unstable region. In addition, an initial sideslip angle of 3^{o} was

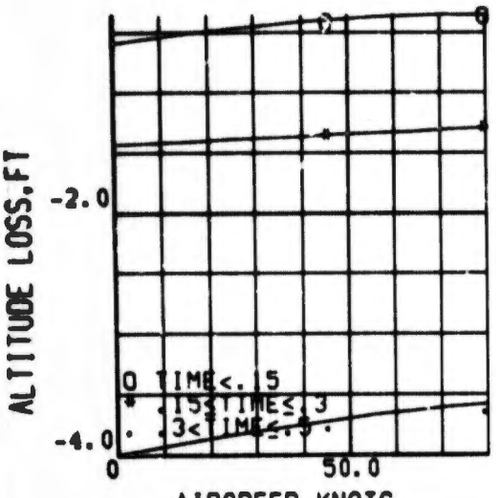

FIG 15 VTOL TWO ENGINE FAILURE
ALTITUDE LOSS AT CRITICAL TIME

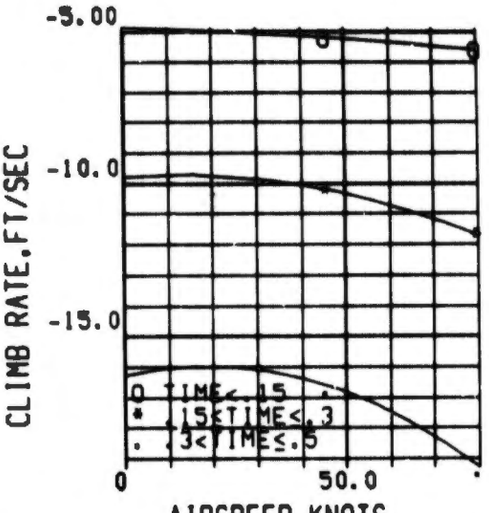

FIG 16 VTOL TWO ENGINE FAILURE
CLIMB RATE AT CRITICAL TIMES

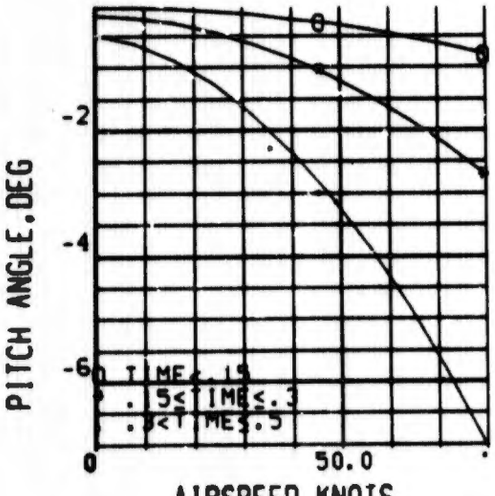

FIG 17 VTOL TWO ENGINE FAILURE
PITCH ANGLE AT CRITICAL TIMES

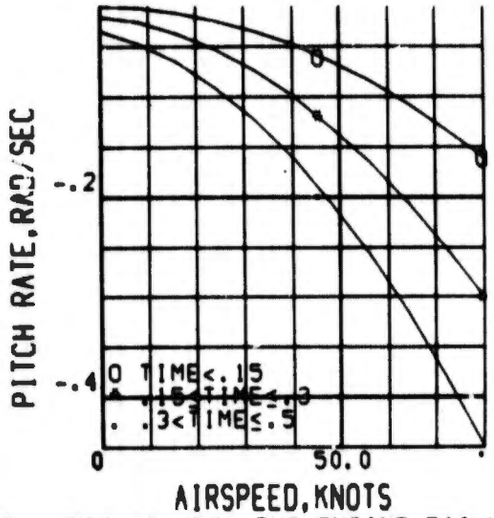

FIG 18 VTOL TWO ENGINE FAILURE
PITCH RATE AT CRITICAL TIMES

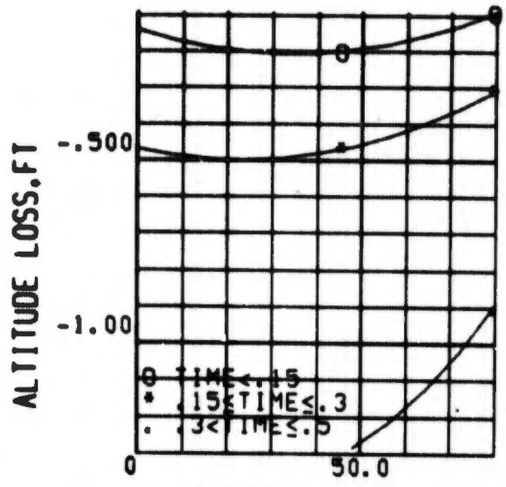

FIG 19 VTOL ONE ENGINE FAILURE
ALTITUDE LOSS AT CRITICAL TIME

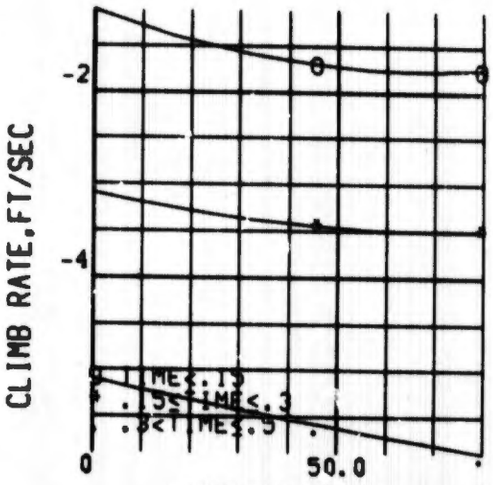

FIG 20 VTOL ONE ENGINE FAILURE
CLIMB RATE AT CRITICAL TIMES

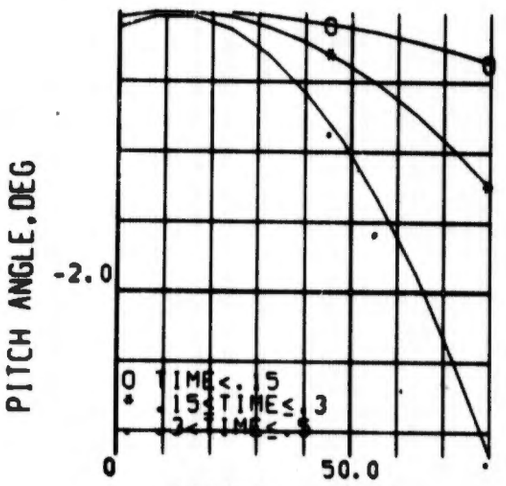

FIG 21 VTOL ONE ENGINE FAILURE
PITCH ANGLE AT CRITICAL TIMES

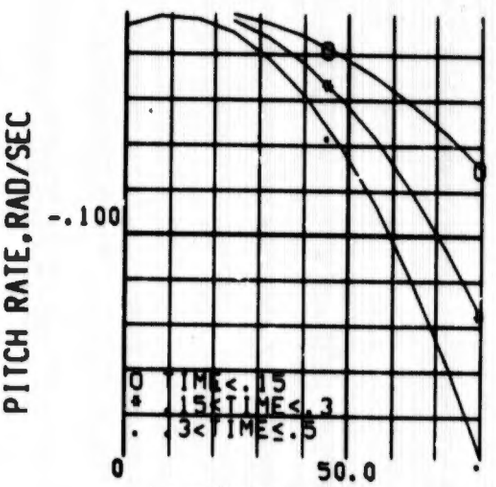

FIG 22 VTOL ONE ENGINE FAILURE
PITCH RATE AT CRITICAL TIMES

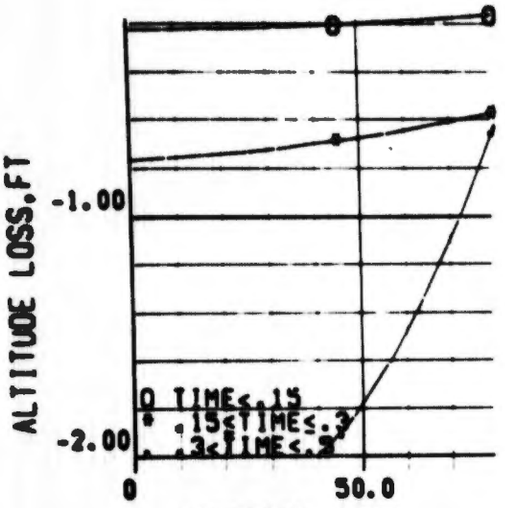

FIG 23 VTOL LAT. CONTROL FAIL.
ALTITUDE LOSS AT CRITICAL TIME

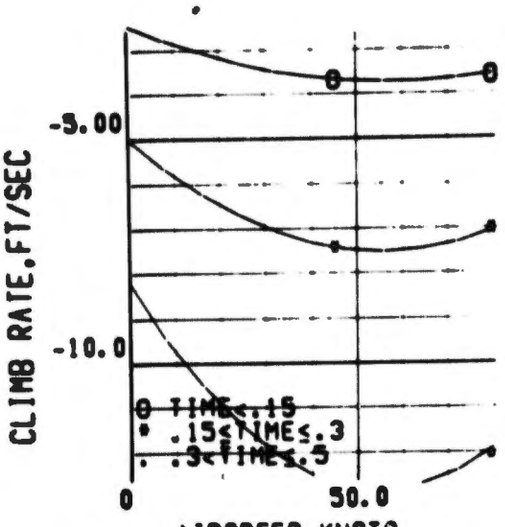

FIG 24 VTOL LAT. CONTROL FAIL.
CLIMB RATE AT CRITICAL TIMES

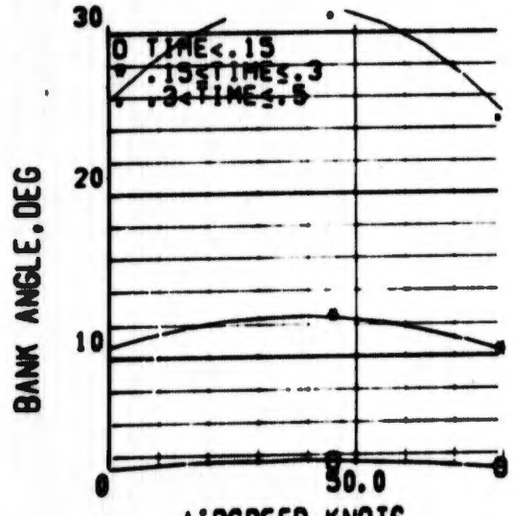

FIG 25 VTOL LAT. CONTROL FAIL.
BANK ANGLE AT CRITICAL TIMES

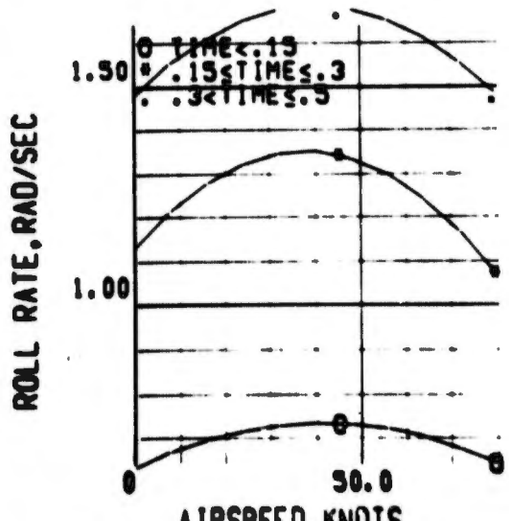

FIG 26 VTOL LAT. CONTROL FAIL.
ROLL RATE AT CRITICAL TIMES

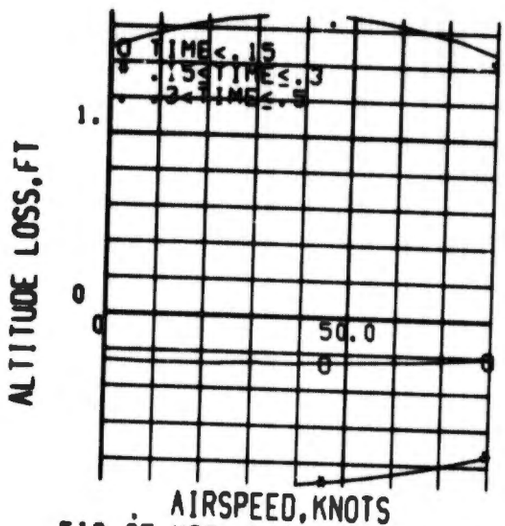

FIG 27 VTOL LAT. CONTROL PLUS ONE ENG. FAIL.,ALT. LOSS

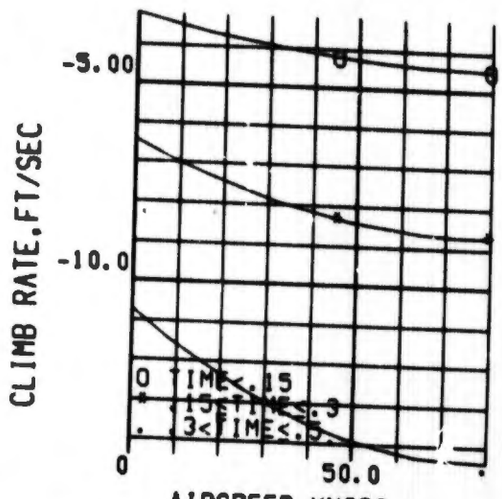

FIG 28 VTOL LAT. CONTROL PLUS ONE ENG. FAIL.,CLIMB RATE

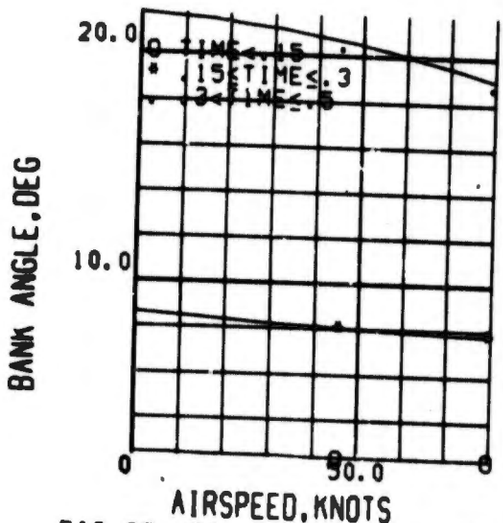

FIG 29 VTOL LAT. CONTROL PLUS ONE ENG. FAIL..BANK ANGLE

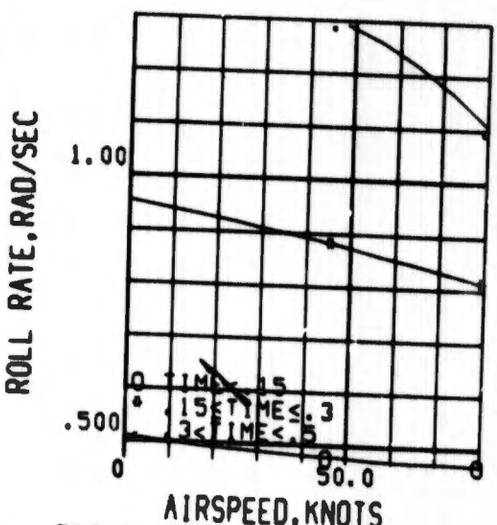

FIG 30 VTOL LAT. CONTROL PLUS ONE ENG. FAIL..ROLL RATE

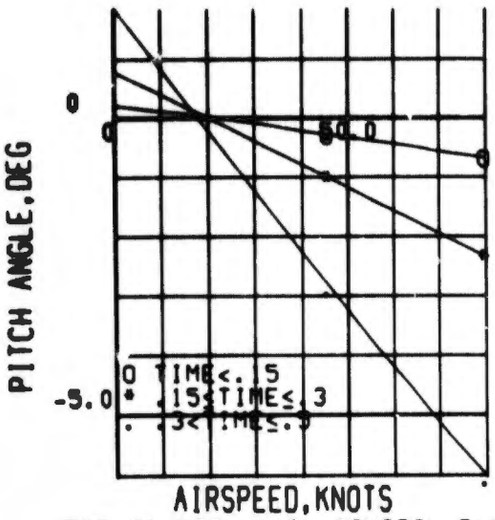

FIG 31 VTOL LAT. CONTROL PLUS ONE ENG. FAIL., PITCH ANGLE

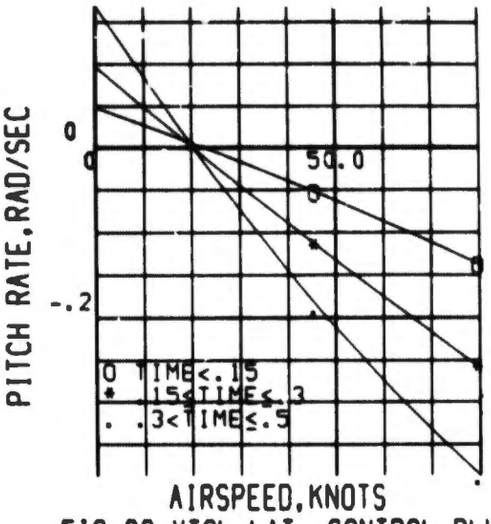

FIG 32 VTOL LAT. CONTROL PLUS ONE ENG. FAIL., PITCH RATE

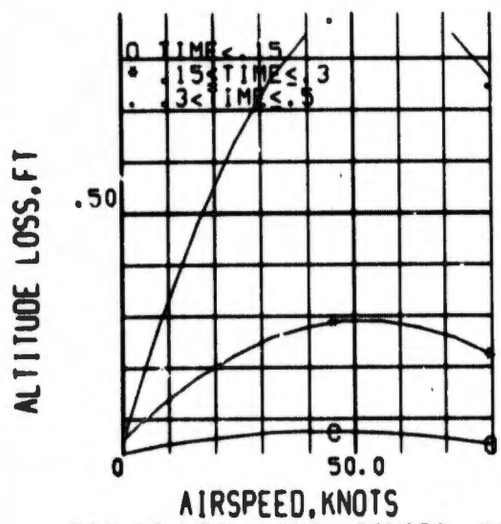

FIG 33 VTOL LONG. CONTROL FAIL ALTITUDE LOSS AT CRITICAL TIME

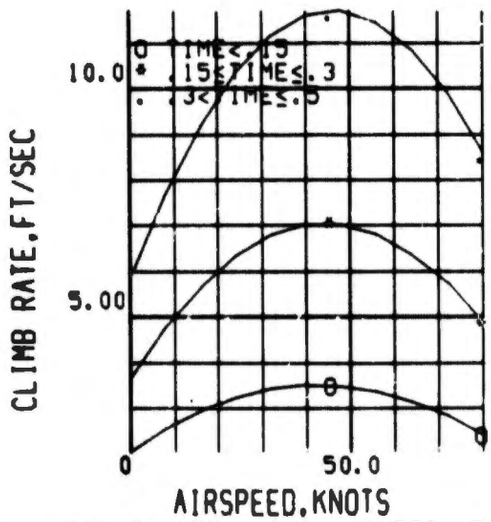

FIG 34 VTOL LONG. CONTROL FAIL CLIMB RATE AT CRITICAL TIMES

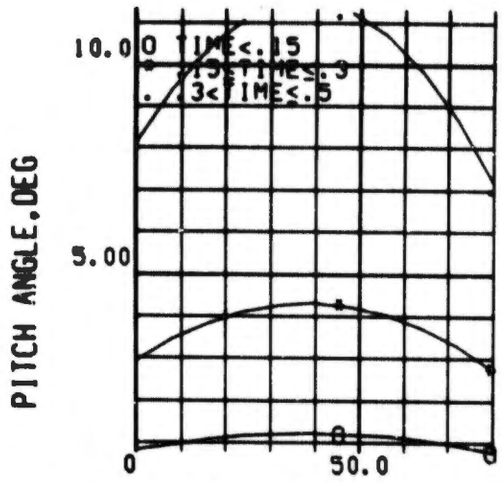

FIG 35 VTOL LONG. CONTROL FAIL
PITCH ANGLE AT CRITICAL TIMES

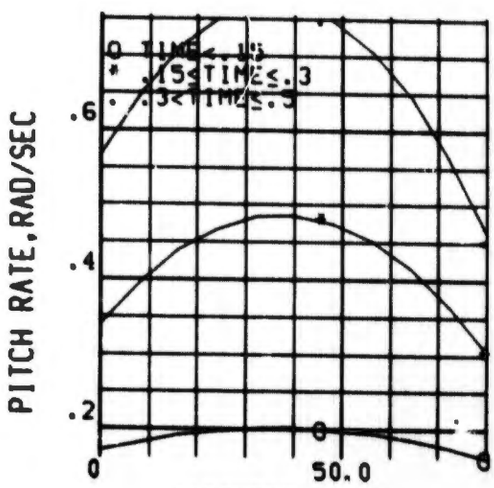

FIG 36 VTOL LONG. CONTROL FAIL
PITCH RATE AT CRITICAL TIMES

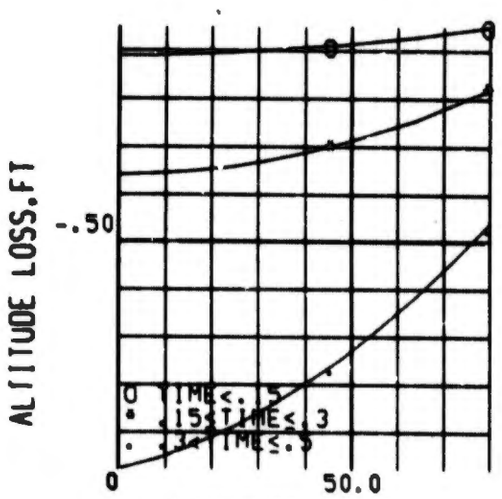

FIG 37 VTOL LONG. CONTROL PLUS
ONE ENG. FAIL., ALT. LOSS

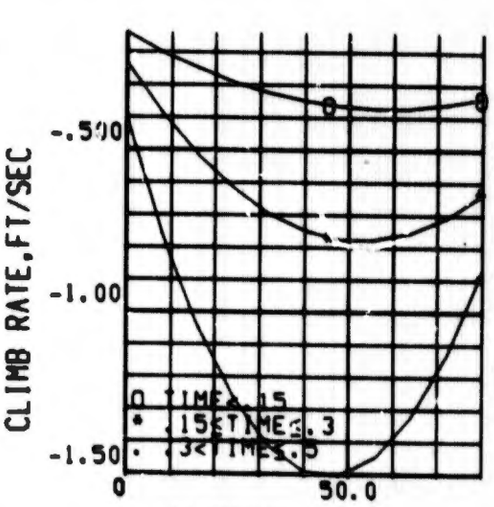

FIG 38 VTOL LONG. CONTROL PLUS
ONE ENG. FAIL., CLIMB RATE

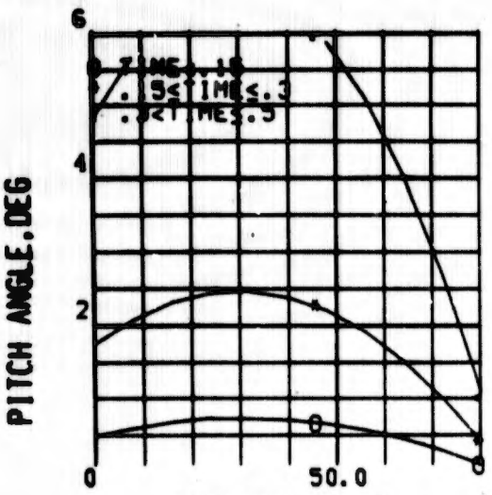

FIG 39 VTOL LONG. CONTROL PLUS ONE ENG. FAIL., PITCH ANGLE

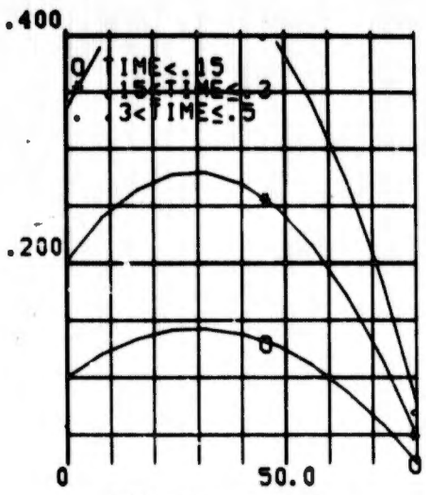

FIG 40 VTOL LONG. CONTROL PLUS ONE ENG. FAIL., PITCH RATE

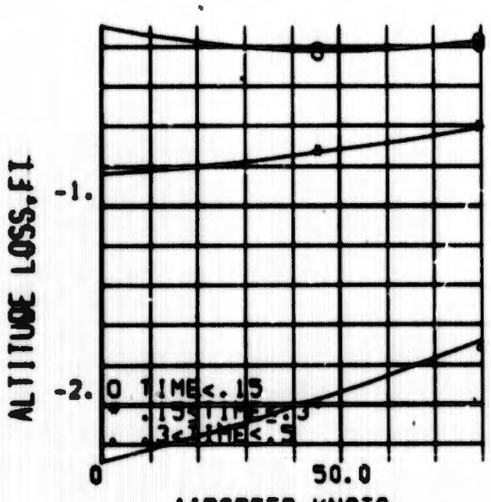

FIG 41 VTOL LAT.,LONG. CONTROL PLUS SINGLE ENGINE FAILURE

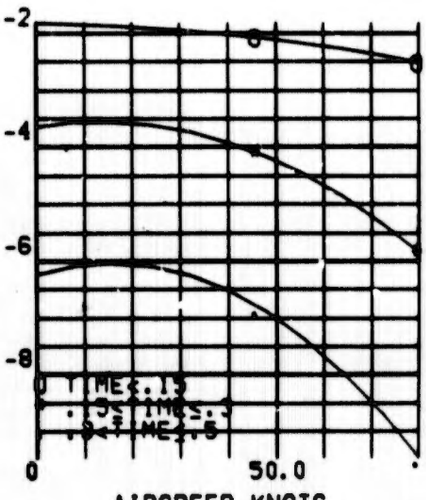

FIG 42 VTOL LAT.,LONG. CONTROL PLUS SINGLE ENGINE FAILURE

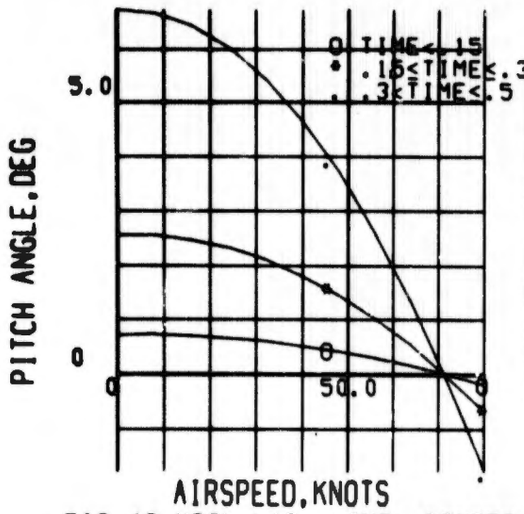

FIG 43 VTOL LAT.,LONG. CONTROL PLUS SINGLE ENGINE FAILURE

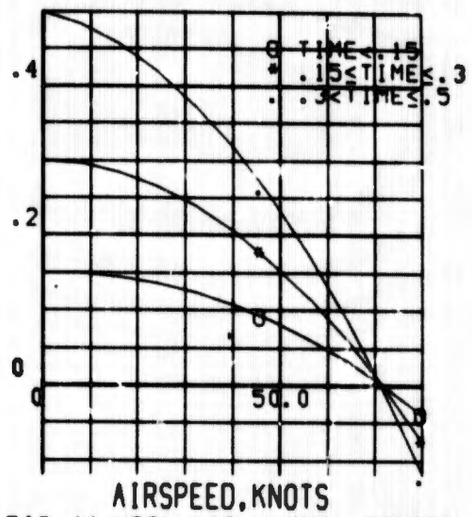

FIG 44 VTOL LAT.,LONG. CONTROL PLUS SINGLE ENGINE FAILURE

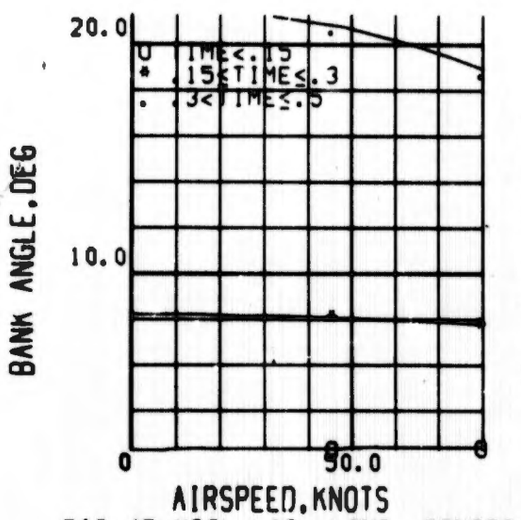

FIG 45 VTOL LAT.,LONG. CONTROL PLUS SINGLE ENGINE FAILURE

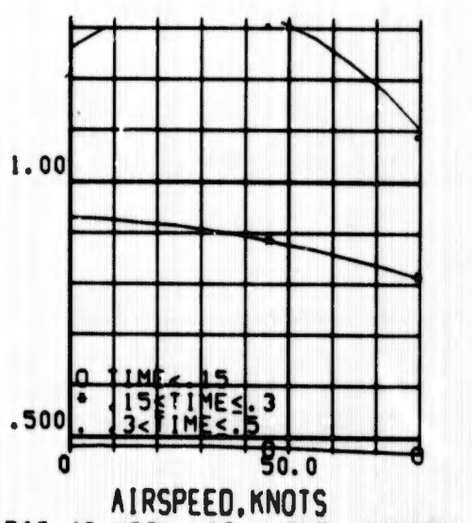

FIG 46 VTOL LAT.,LONG. CONTROL PLUS SINGLE ENGINE FAILURE

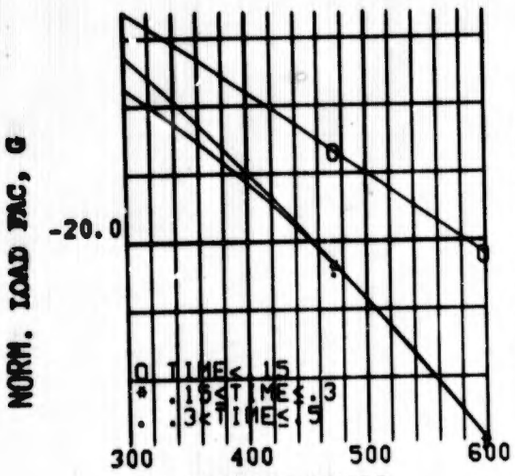

FIG 47 LONG. CONTROL FAILURE CONV. FLT., COCKPIT LOAD FAC.

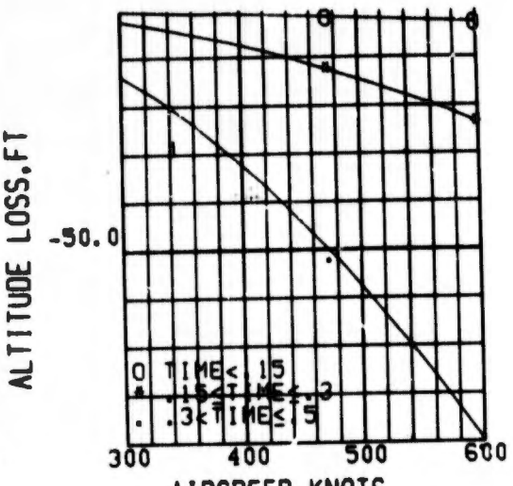

FIG 48 LONG. CONTROL FAILURE CONV. FLT., ALTITUDE LOSS

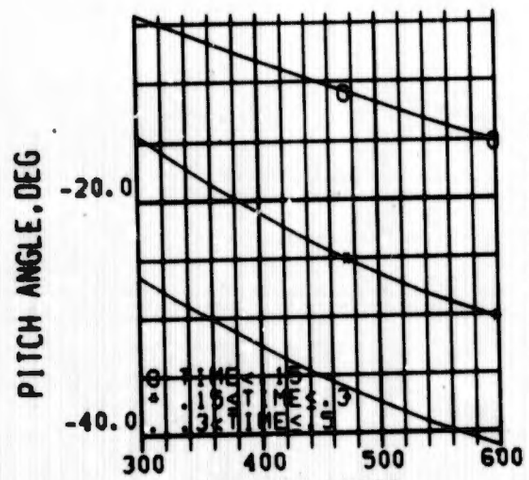

FIG 49 LONG. CONTROL FAILURE CONV. FLT., PITCH ATTITUDE

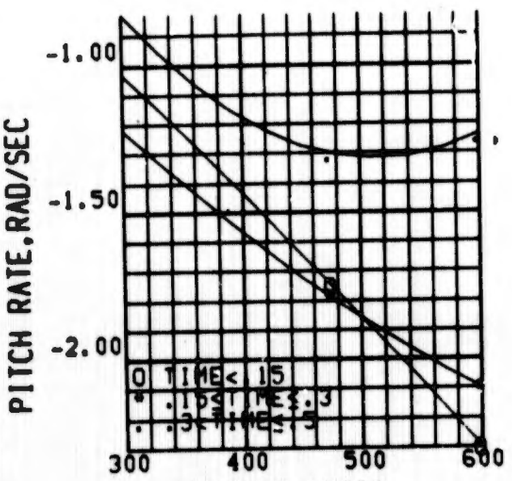

FIG 50 LONG. CONTROL FAILURE CONV. FLT., PITCH RATE

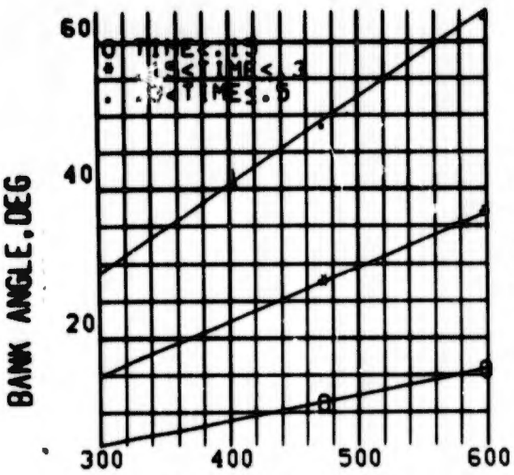

FIG 51 LAT. CONTROL FAILURE CONV. FLT., BANK ANGLE

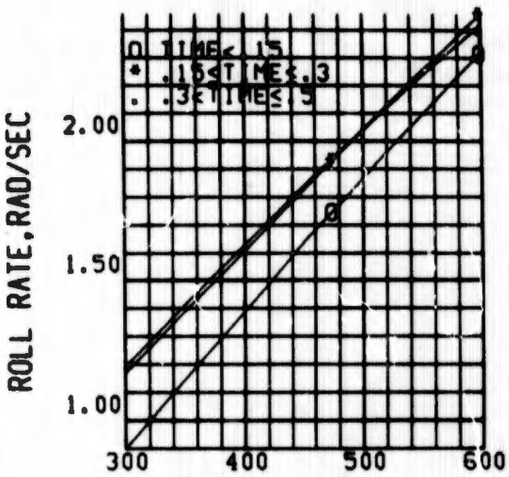

FIG 52 LAT. CONTROL FAILURE CONV. FLT., ROLL RATE

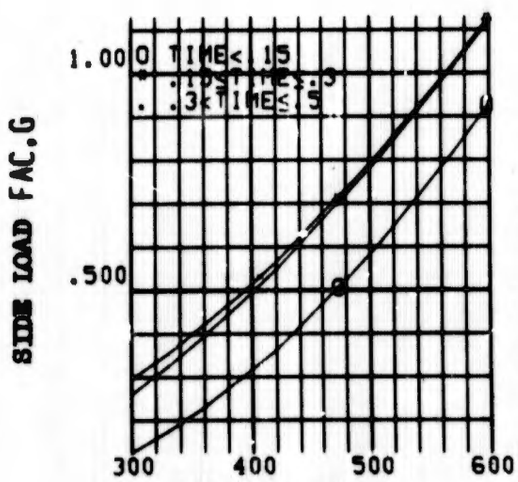

FIG 53 LAT. CONTROL FAILURE CONV. FLT., COCKPIT LOAD FAC.

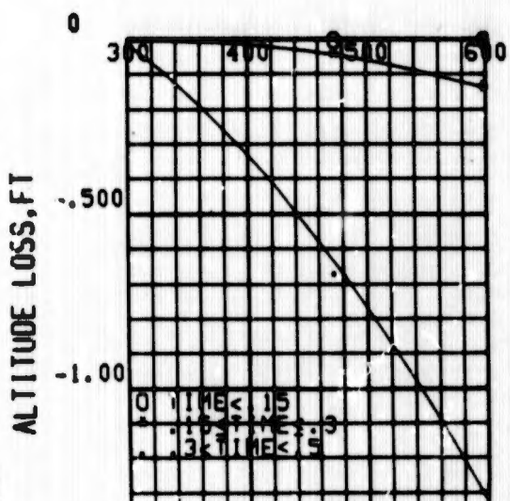

FIG 54 LAT. CONTROL FAILURE CONV. FLT., ALTITUDE LOSS

(Page 40 is blank)

BLANK PAGE

Appendix I

VTOL SIMULATION EQUATIONS AND DATA

APPENDIX I

TABLE OF CONTENTS

APPENDIX I
VTOL SIMULATION EQUATIONS AND DATA

SECTION I
GENERAL

The equations formulated in this section have been used in conjunction with the accompanying data to mechanize a six degree-of-freedom digital computer simulation of an airplane operating from the VTOL regime to high speed conventional flight conditions.

The body axis equations of motion are derived from fundamental physical laws expressed as vector relations which are transformed to matrices for the computation of three angular acceleration components and three linear acceleration components. The resulting coupled acceleration components are converted to six first order differential equations soluble by digital computer through a numerical integration algorithm. The integrated variables are the desired time histories, revealing the aircraft response to an arbitrary combination of forcing functions.

The aerodynamic data are referenced to "slipstream q" and, therefore, present no computational difficulties in hover, transition or conventional flight. Curve-fit and table-look-up techniques are utilized to compute the non-dimensional aerodynamic coefficients and are efficient enough to provide computation time less than real time.

The aircraft attitude with respect to the earth is computed by integrating six of the nine conventional direction cosine rates. The remaining three direction cosines are determined through an orthogonal relationship involving the six integrated rates. From the appropriate direction cosines the Euler angles are computed.

All the symbols needed to understand the equations and data curves are summarized in Section II.

SECTION II
SYMBOLS

Summarization of symbols for equations and data curves.

PARAMETER	UNITS	DEFINITION
I_X	SL-FT^2	Body axis rolling moment of inertia
I_Y	SL-FT^2	Body axis pitching moment of inertia
I_Z	SL-FT^2	Body axis yawing moment of inertia
I_{XZ}	SL-FT^2	Body axis product of inertia
m	SLUG	Airplane mass
ρ	SL/FT^3	Air density
A_F	FT^2	Area of two fans (reference area)
A_{NF}	FT^2	Area of the nose fan (reference area)
S_w	FT^2	Wing reference area
S_t	FT^2	Horizontal tail reference area
$\bar{c}$	FT	Wing mean aerodynamic chord (M.A.C.)
b	FT	Reference wing span
D_F	FT	Reference diameter of one wing fan
Y_F	FT	Spanwise distance from the plane of symmetry to the wing fan hub, >0.
X_{NF}	FT	Longitudinal body axis distance, in the plane of symmetry, from the C.G. (Center of Gravity) to the nose fans hub, >0.
Tc^s	NON-DIM	Average slipstream thrust coefficient based on slipstream q and wing fan area

SECTION II

SYMBOLS

PARAMETER	UNITS	DEFINITION
i_e	RAD	Engine thrust vector incidence angle, positive for an upward rotation of the thrust above the body X-axis
$\frac{\ell_t}{\bar{c}}$	NON-DIM	H. T. (Horizontail tail) arm, from the C. G. to the horizontal tail M.A.C., positive for tail aft of the C. G. (Non-dimensionalized by the wing M.A.C.)
$\frac{Z_t}{\bar{c}}$	NON-DIM	Vertical, non-dimensional distance in the plane of symmetry, from the C. G. to the H. T. M.A.C., positive for the H. T. M.A.C. above the C. G.
Z_j	FT	Engine thrust vertical moment arm. distance from the C.G. to the point of thrust application, positive for thrust point below the C.G.
ℓ_j	FT	Engine thrust horizontal moment arm. Distance from the C.G. to the point of thrust application, positive for thrust point forward of the C.G.
$C_{L_{\alpha_t}}$	RAD^{-1}	H.T. lift-curve slope, referenced to H.T. area, excluding downwash
$C_{L_{\delta_e}}$	RAD^{-1}	Elevator lift effectiveness, referenced to H.T. area
$C_{D_{o_t}}$	NON-DIM	H.T. drag coefficient at H.T. zero lift, based on H.T. area
$C_{D_{C_L{}^2_t}}$	NON-DIM	H.T. induced drag, referenced to H.T. area
$C_{y_{\delta_r}}$	RAD^{-1}	Rudder side force coefficient, based on wing area
$C_{y_{\delta_a}}$	RAD^{-1}	Aileron side force coefficient, based on wing area
$C_{n_{\delta_r}}$	RAD^{-1}	Rudder yawing effectiveness, based on wing area and wing span
$C_{n_{\delta_a}}{}_{(Tc^\beta=0)}$	RAD^{-1}	Aileron yawing effectiveness at zero slipstream thrust coefficient (Tc^β), based on wing area and span
$\frac{\partial C_{n_{\delta_a}}}{\partial Tc^\beta}$	RAD^{-1}	Variation of aileron yawing effectiveness with Tc^β, based on wing area and span

PARAMETER	UNITS	DEFINITION
$C_{\ell_{\delta r}}$	RAD^{-1}	Rudder rolling effectiveness, based on wing area and span
$C_{\ell_{\delta a}}$	RAD^{-1}	Aileron rolling effectiveness, referenced to wing area and span, for one aileron
T_{sso_R}	LB	Static thrust from the right fan at zero speed, zero vector and zero stagger
T_{sso_L}	LB	Static thrust from the left fan at zero speed, zero vector, and zero stagger
$T_{o_{NF}}$	LB	Nose fan static thrust at zero speed
δ_T , δ_H	RAD	H.T. incidence, positive for trailing edge down, relative to fuselage center line
δ_e	RAD	Elevator deflection, positive for trailing edge down, relative to H.T. root chord
δ_r	RAD	Rudder deflection, positive for trailing edge left, relative to plane of symmetry
δ_{a_R}	RAD	Right aileron deflection, positive for trailing edge down
δ_{a_L}	RAD	Left aileron deflection, positive for trailing edge down
$K_{x_{NF}}$	NON-DIM	Nose fan axial force variation with thrust reverser door position
K_{tS}	NON-DIM	Thrust spoiler effectiveness
$K_{z_{NF}}$	NON-DIM	Nose fan normal force variation with thrust reverser door position
Tj	LB	Turbojet thrust
Cy_r	RAD^{-1}	$\partial Cy / \partial\left(\frac{rb}{2V_T}\right)$, side force coefficient variation with non-dimensional yaw rate
C_{L_q}	RAD^{-1}	$\partial C_L / \partial\left(\frac{\bar{q}c}{2V_T}\right)$, lift coefficient variation with non-dimensional pitch rate
$C_{L_{\dot{\alpha}}}$	RAD^{-1}	$\partial C_L / \partial\left(\frac{\dot{\alpha}c}{2V_T}\right)$, lift coefficient variation with non-dimensional plunge rate, primarily H.T. downwash lag
C_{ℓ_p}	RAD^{-1}	$\partial C_\ell / \partial\left(\frac{Pb}{2V_T}\right)$, roll damping

PARAMETER	UNITS	DEFINITION
C_{l_r}	RAD^{-1}	$\partial C_l / \partial \left(\frac{rb}{2V_T}\right)$, rotary coupling derivative relating variation of rolling moment coefficient with non-dimensional yaw rate
C_{m_β}	RAD^{-1}	$\partial C_m / \partial \lvert\beta\rvert$, pitch-sideslip coupling
C_{m_q}	RAD^{-1}	$\partial C_m / \partial \left(\frac{q\bar{c}}{2V_T}\right)$, pitch damping
$C_{m_{\dot{\alpha}}}$	RAD^{-1}	$\partial C_m / \partial \left(\frac{\dot{\alpha}\bar{c}}{2V_T}\right)$, pitching moment coefficient variation with non-dimensional plunge rate
C_{n_r}	RAD^{-1}	$\partial C_n / \partial \left(\frac{rb}{2V_T}\right)$, yaw damping
C_{n_p}	RAD^{-1}	$\partial C_n / \partial \left(\frac{pb}{2V_T}\right)$, rotary coupling derivative, variation of yawing moment coefficient with helix angle
β_{V_o}	RAD	β_V origin about which the variation of $\frac{\partial}{\partial \beta_V}\left(\frac{\partial C_X^s}{\partial \alpha}\right)$ is expanded.
α_1 thru α_9	RAD	Table of alphas for TLU (Table-Look-Up) of alpha dependent functions.
β_{V_R}	RAD	Right fan louver vector angle
β_{V_L}	RAD	Left fan louver vector angle
β_{S_R}	RAD	Right fan louver stagger angle
β_{S_L}	RAD	Left fan louver stagger angle
R_{q_1} thru R_{q_5}	NON-DIM	$R_q = 1 - T_c^s$, ratio of slipstream q^s to free-stream q. These five values of R_q are used for TLU of R_q dependent functions.
$\lvert\beta\rvert_{max}$	RAD	Limit of sideslip angle which will generate realistic aerodynamic functions
$C_{N^s}{}_{o_{R,L}}$	NON-DIM	Tail off zero lift normal force coefficient. $C_{N^s}{}_o = Y_o + B_1 R_q + B_2 R_q^2$

PARAMETER	UNITS	DEFINITION
$\partial C_m^{\,s}/\partial \alpha_{R,L}$	RAD^{-1}	Tail off longitudinal static stability coefficient. $\partial C_m^{\,s}/\partial \alpha = Yo + B_1 R_q + B_2 R_q^{\,2}$
$\epsilon_{(\alpha=0)}$	RAD	Downwash angle at the H.T. at zero angle of attack. $\epsilon_{(\alpha=0)} = Yo + B_1 R_q + B_2 R_q$
Cy^{s}_{β}	RAD^{-1}	Side force coefficient. $C_y^{\,s}{}_{\beta} = Yo + B_1 R_q + B_2 R_q^{\,2}$
$C_n^{\,s}{}_{\beta}$	RAD^{-1}	Directional Stability. $C_n^{\,2}{}_{\beta} = Yo + B_1 R_q + B_2 R_q^{\,2}$
$\frac{\partial}{\partial \beta_v}\left[\frac{\partial C_N^{\,s}}{\partial \alpha}\right]$	RAD^{-2}	Variation of slope of the normal force coefficient with exit louver vector.
$\frac{\partial}{\partial R_q}\left[\frac{\partial}{\partial \beta_v}\left(\frac{\partial C_N^{\,s}}{\partial \alpha}\right)\right]$	RAD^{-2}	Variation of the slope of the normal force coefficient with exit louver vector and dynamic pressure ratio.
$C_N^{\,s}{}_{o_{NF}}$	NON-DIM	Nose fan normal force coefficient. $C_N^{\,s}{}_{o_{NF}} = Yo + B_1 R_{q_{NF}} + B_2 R_{q_{NF}}^{\,2}$
$C_X^{\,s}{}_{o_{NF}}$	NON-DIM	Nose fan axial force coefficients. $C_X^{\,2}{}_{o_{NF}} = Yo + B_1 R_{q_{NF}} + B_2 R_{q_{NF}}^{\,2}$
$\left(1/\frac{C_P^{\,s}}{C_{P_o}^{\,2}}\right)_{NF}$	NON-DIM	Nose fan power coefficient ratio $\left(1/\frac{C_P^{\,s}}{C_{P_o}^{\,2}}\right)_{NF} = Yo + B_1 R_{q_{NF}} + B_2 R_{q_{NF}}^{\,2}$
P_{NF}	FT-LB/SEC	Nose fan power $P_{NF} = Yo + B_1 N + B_2 N^2$

PARAMETER	UNITS	DEFINITION
$C_{PS}/C_{P_o}{}^{s}$	NON-DIM	Main fan power coefficient ratio, $C_{PS}/C_{Pso} = Yo + B_1\beta_s + B_2\beta_s{}^2$
$\epsilon_{(\alpha)}$	RAD	H.T. downwash angle variation with angle of attack, $\epsilon_{(\alpha)} = \epsilon_{(\alpha=o)} + B_1\alpha + B_2\alpha^2$
$(K_t\eta_t)$	NON-DIM	Horizontal tail efficiency factor $(K_t\eta_t) = Yo + B_1\alpha + B_2\alpha^2$
$C^s{}_{\ell_{\beta_{(\alpha=o)}}}$	RAD^{-1}	Zero angle of attack effective dihedral table, corresponding to the R_q table,
$B_1\left(\Delta C^s{}_{\ell_\beta}\right)$	RAD^{-2}	$B_1 = \frac{\partial}{\partial\alpha}\left(C^s{}_{\ell_\beta}\right)$. For a given R_q $C^s{}_{\ell_\beta} = C^s{}_{\ell_{\beta(\alpha=o)}} + B_1\alpha + B_2\alpha^2$, where $C^s{}_{\ell_{\beta_{(\alpha=o)}}}$, B_1 and B_2 vary with R_q.
$\left(\frac{\partial C_N{}^s}{\partial\alpha}\right)_{\beta_v=o}$	RAD^{-1}	R_q dependent table of the slope of the normal force coefficient for zero exit louver vector angle.
$C_p{}^s/C_p{}^s{}_o$	NON-DIM	$C_p{}^s/C_p{}^s{}_o = \left[C_p{}^s/C_p{}^s{}_o\right]_{\beta_v=o} + B_1\beta_v + B_2\beta_v{}^2$, where $\left[C_p{}^s/C_p{}^2{}_o\right]_{\beta_v=o}$, B_1 and B_2 are tables of R_q dependent values, $\beta_s = 0$.
$\Delta C_N{}^s{}_{(\beta_v)}$	RAD^{-1}, RAD^{-2}	$\Delta C_N{}^s{}_{(\beta_v)} = B_1\beta_v + B_2\beta_v{}^2$, where B_1 and B_2 are tables of R_q dependent values, $\beta_s = o$.

PARAMETER	UNITS	DEFINITION
$\Delta C_{x}^{s}{}_{(\beta_v)}$	RAD^{-1}, RAD^{-2}	$C_{x}^{s}{}_{(\beta_v)} = B_1\beta_v + B_2\beta_v^2$, where B_1 and B_2 are tables of R_q dependent values, $\beta_s = 0$.
$\Delta C_{m}^{s}{}_{(\beta_v)}$	RAD^{-1}, RAD^{-2}	$\Delta C_{m}^{s}{}_{(\beta_v)} = B_1\beta_v + B_2\beta_v^2$, where B_1 and B_2 are tables of R_q dependent values, $\beta_s = 0$.

SECTION III
GENERAL EQUATIONS OF MOTION

GENERAL EQUATIONS OF MOTION

The following equations of motion are developed with sufficient generality to be used in simulating any airplane, in V/STOL or conventional flight, as well as an escape seat and a parachuting human. For each type of simulation the nature of the forces and moments vary but the equations of motion will still be representative, although many of the terms can be neglected for the simpler systems.

ANGULAR MOMENTUM RATE VECTOR

$$\Sigma r = \dot{H}_a + \Omega_a X H_a + \dot{H}_{ep} + \Omega_{ep} X H_{ep} + \dot{H}_e + \Omega_e X H_e$$

Where the subscripts are:

a - refers to fixed structural components of the airplane.

ep - refers to varying incidence components such as engine, pod and/or wings.

e - refers to components with significantly high rotation rates whose angular momentum is not canceled by counter rotating parts - such as turbine blades, fans and propellers.

$$H_a = iH_{x_a} + jH_{y_a} + kH_{z_a}$$

$$\begin{Bmatrix} H_{x_a} \\ H_{y_a} \\ H_{z_a} \end{Bmatrix} = \begin{bmatrix} I_{xx_a} & 0 & -I_{xz_a} \\ 0 & I_{yy_a} & 0 \\ -I_{xz_a} & 0 & I_{zz_a} \end{bmatrix} \begin{Bmatrix} p \\ q \\ r \end{Bmatrix}$$

$$\Omega_a = ip + jq + kr$$

The angular momentum components, expressed in matrix notation, are

$$H_a = G_a \Omega_a$$

where G_a is the inertia tensor, expanded above.

Consequently,

$$\dot{H}_a = \mathbf{i}\dot{H}_{x_a} + \mathbf{j}\dot{H}_{y_a} + \mathbf{k}\dot{H}_{z_a}$$

Where the components are given by the derivative of the inertia tensor.

$$\dot{H}_a = G_a\dot{\Omega}_a$$

The remaining two angular momentum rate vectors must be transformed to the I, J, K axis system before adding components.

The unit vectors relating the two axis systems are developed from the following figure, for systems a and ep.

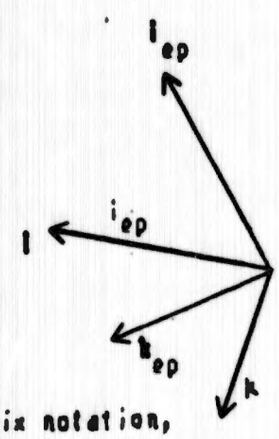

Or, in matrix notation,

$$\begin{Bmatrix} i_{ep} \\ j_{ep} \\ k_{ep} \end{Bmatrix} = \begin{bmatrix} \mathrm{Cos}(i_{ep}) & 0 & -\mathrm{Sin}(i_{ep}) \\ 0 & 1 & 0 \\ \mathrm{Sin}(i_{ep}) & 0 & \mathrm{Cos}(i_{ep}) \end{bmatrix} \begin{Bmatrix} I \\ J \\ K \end{Bmatrix}$$

$$U_{ep} = D_{ep}\, U_a$$

Furthermore, because of the orthogonality of D_{ep}, $D_{ep}^{-1} = D_{ep}^{T}$

$$U_a = D^{T}_{ep}\, U_{ep}$$

Now, defining the ep inertia tensor

$$G_{ep} = \begin{bmatrix} I_{x_{ep}} & 0 & -I_{xz_{ep}} \\ 0 & I_{y_{ep}} & 0 \\ -I_{xz_{ep}} & 0 & I_{z_{ep}} \end{bmatrix}$$

The components of the angular momentum vector,

$$\mathbf{H}_{ep} = \mathbf{i}H_{x_{ep}} + \mathbf{j}H_{y_{ep}} + \mathbf{k}H_{z_{ep}}$$

are given by

$$H_{ep} = D_{ep}\, G_{ep}\, D^{T}_{ep}\, \Omega_a$$

which, when expanded, results in

$$H_{x_{ep}} = [I_{x_{ep}}\mathrm{Cos}^2(i_{ep}) - 2I_{xz_{ep}}\mathrm{Sin}(i_{ep})\,\mathrm{Cos}(i_{ep}) + I_{z_{ep}}\mathrm{Sin}^2(i_{ep})\,]\,p$$
$$+ [[(I_{z_{ep}} - I_{x_{ep}})\,\mathrm{Sin}(i_{ep})\,\mathrm{Cos}(i_{ep}) + I_{xz_{ep}}(\mathrm{Sin}^2(i_{ep}) - \mathrm{Cos}^2(i_{ep}))]\,r$$

$$H_{y_{ep}} = I_{y_{ep}}\, q$$

$$H_{z_{ep}} = [(I_{z_{ep}} - I_{x_{ep}})\,\mathrm{Sin}(i_{ep})\,\mathrm{Cos}(i_{ep}) + I_{xz_{ep}}(\mathrm{Sin}^2(i_{ep}) - \mathrm{Cos}^2(i_{ep}))]\,p$$
$$+ [I_{x_{ep}}\mathrm{Sin}^2(i_{ep}) + 2I_{xz_{ep}}\mathrm{Sin}(i_{ep})\,\mathrm{Cos}(i_{ep}) + I_{z_{ep}}\mathrm{Cos}^2(i_{ep})\,]\,r$$

Similarly, a direction cosine matrix relating system e to system a is

$$D_e = \begin{bmatrix} \mathrm{Cos}(i_e) & 0 & -\mathrm{Sin}(i_e) \\ 0 & 1 & 0 \\ \mathrm{Sin}(i_e) & 0 & \mathrm{Cos}(i_e) \end{bmatrix}$$

The inertia tensor is

$$G_e = \begin{bmatrix} Ix_e & 0 & 0 \\ 0 & Iy_e & 0 \\ 0 & 0 & Iz_e \end{bmatrix}$$

The rotation vector representing the fast rotating part plus the rates of mounts attached to the fixed frame is

$$\Omega_e = I_e\omega_{x_e} + Ip + Jq + Kr$$

$$= I[p + \omega_{x_e}\mathrm{Cos}(i_e)] + Jq + K[r - \omega_{x_e}\mathrm{Sin}(i_e)]$$

The components of the angular momentum vector

$$H_e = IH_{x_e} + JH_{y_e} + KH_{z_e}$$

are given by

$$H_e = D_e\, G_e\, D_e^T \Omega_n + D_e\, G_e\, (\omega_{x_e}, 0, 0)^T$$

which, when expanded, results in

$$H_{x_e} = [Ix_e\mathrm{Cos}^2(i_e) + Iz_e\mathrm{Sin}^2(i_e)]\,p$$

$$+ [(Iz_e - Ix_e)\mathrm{Sin}(i_e)\,\mathrm{Cos}(i_e)]\,r$$

$$+ I_{x_e}\mathrm{Cos}(i_e)\,\omega_{x_e}$$

$$H_{y_e} = I_{y_e}\,q$$

$$H_{z_e} = [(I_{z_e}-I_{x_e})\mathrm{Cos}(i_e)\,\mathrm{Sin}(i_e)\,]\,p + [I_{x_e}\mathrm{Sin}^2(i_e) + I_{z_e}\mathrm{Cos}^2(i_e)\,]\,r - I_{x_e}\mathrm{Sin}(i_e)\,\omega_{x_e}$$

All the angular momentum components have now been transformed to the same axis system and can be added to generate the matrix equations

$$\begin{Bmatrix} H_x \\ H_y \\ H_z \end{Bmatrix} = \begin{bmatrix} I_{xx} & 0 & -I_{xz} \\ 0 & I_{yy} & 0 \\ -I_{xz} & 0 & I_{zz} \end{bmatrix} \begin{Bmatrix} p \\ q \\ r \end{Bmatrix} + \begin{Bmatrix} I_{x_e}\mathrm{Cos}(i_e)\,\omega_{x_e} \\ 0 \\ -I_{x_e}\mathrm{Sin}(i_e)\,\omega_{x_e} \end{Bmatrix}$$

Where

$$I_{xx} = I_{xx_e} + I_{x_{ep}}\mathrm{Cos}^2(i_{ep}) - 2I_{xz_{ep}}\mathrm{Sin}(i_{ep})\,\mathrm{Cos}(i_{ep}) + I_{z_{ep}}\mathrm{Sin}^2(i_{ep}) + I_{x_e}\mathrm{Cos}^2(i_e) + I_{z_e}\mathrm{Sin}^2(i_e)$$

$$I_{xz} = I_{xz_e} + I_{xz_{ep}}[\mathrm{Cos}^2(i_{ep}) - \mathrm{Sin}^2(i_{ep})\,] + [I_{x_{ep}}-I_{z_{ep}}]\mathrm{Sin}(i_{ep})\,\mathrm{Cos}(i_{ep}) + [I_{x_e}-I_{z_e}]\mathrm{Sin}(i_e)\,\mathrm{Cos}(i_e)$$

$$I_{yy} = I_{y_e} + I_{y_{ep}} + I_{y_e}$$

$$I_{zz} = I_{zz_e}$$

$$+ I_{z_{op}}\cos^2(i_{op}) + 2I_{xz_{op}}\sin(i_{op})\cos(i_{op}) + I_{x_{op}}\sin^2(i_{op})$$

$$+ I_{z_g}\cos^2(i_g) + I_{x_g}\sin^2(i_g)$$

The components of $\dot{\vec{H}}$ are given by differentiating the angular momentum vector components, resulting in the following matrix.

$$\begin{Bmatrix} \dot{H}_x \\ \dot{H}_y \\ \dot{H}_z \end{Bmatrix} = \begin{bmatrix} I_{xx} & 0 & -I_{xz} \\ 0 & I_{yy} & 0 \\ -I_{xz} & 0 & I_{zz} \end{bmatrix} \begin{Bmatrix} \dot{p} \\ \dot{q} \\ \dot{r} \end{Bmatrix} + \begin{Bmatrix} I_{x_g}\cos(i_g)\,\dot{\Omega}_{z_g} \\ 0 \\ -I_{x_g}\sin(i_g)\,\dot{\Omega}_{z_g} \end{Bmatrix}$$

The vector product is

$$\vec{\Omega} \times \vec{H} = \begin{bmatrix} \vec{i} & \vec{j} & \vec{k} \\ p & q & r \\ H_x & H_y & H_z \end{bmatrix}$$

$$= \vec{i}(qH_z - rH_y) + \vec{j}(rH_x - pH_z) + \vec{k}(pH_y - qH_x)$$

Equating the moment components of the vector equation

$$\Sigma\vec{r} = \dot{\vec{H}} + \vec{\Omega} \times \vec{H}$$

results in

$$\Sigma r_x = I_{xx}\dot{p} - I_{xz}\dot{r} + qH_z - rH_y$$

$$= r_{x_g} + r_{x_p}\dot{p} + r_{x_r}\dot{r} + r_{x_v}\dot{v}$$

$$\Sigma r_y = I_{yy}\dot{q} + rH_x - pH_z$$

$$= r_{y_g} + r_{y_q}\dot{q} + r_{y_m}\dot{m}$$

$$\Sigma r_z = -I_{xz}\dot{p} + I_{zz}\dot{r} + qH_y - qH_x$$

$$= r_{z_0} + r_{z_r}\dot{r} + r_{z_p}\dot{p} + r_{z_v}\dot{v}$$

Where the external moments are general enough to be representative of any conceivable configuration.

For conventional flight, the external moments are

$$r_{x_0} = q_0 SbCC_l + F_{z_e}\Delta y_e - F_{y_e}\Delta z_e + \Delta r_x$$

$$r_{y_0} = q_0 Sc\bar{C}C_m + F_{x_e}\Delta z_e - F_{z_e}\Delta x_e + \Delta r_y$$

$$r_{z_0} = q_0 SbCC_n + F_{y_e}\Delta x_e - F_{x_e}\Delta y_e + \Delta r_z$$

$$r_{y_\alpha} = (\rho Sc^2/4)\, C_{m_\alpha}$$

$$r_{y_q} = (\rho Sc^2/4)\,(c/2)\, C_{m_q}$$

$$r_{x_v} = (\rho Sb^2/4)\, C_{l_\beta}$$

$$r_{z_v} = (\rho Sb^2/4)\, C_{n_\beta}$$

$$r_{x_p} = (\rho Sb^2/4)\,(b/2)\, C_{l_p}$$

$$r_{x_r} = (\rho Sb^2/4)\,(b/2)\, C_{l_r}$$

$$r_{z_p} = (\rho Sb^2/4)\,(b/2)\, C_{n_p}$$

$$r_{z_r} = (\rho Sb^2/4)\,(b/2)\, C_{n_r}$$

The aerodynamic coefficient summations, ΣC_l, ΣC_m and ΣC_n are non-dimensional body axis moment coefficients which may require table-look-up for complex, non-linear systems.

For V/STOL flight the equations will have the same form but the variables

will be modified by the use of slipstream notation.

For V/STOL flight replace

q_s with q^s

ΣC_m with $\Sigma C_m{}^s$

$C_{m_{\dot{\alpha}}}$ with $C_{m_{\dot{\alpha}}}{}^s$

ΣC_l with $\Sigma C_l{}^s$

ΣC_n with $\Sigma C_n{}^s$

C_{l_β} with $C_{l_\beta}{}^s$

C_{n_β} with $C_{n_\beta}{}^s$

The remaining aerodynamic coefficients represent structural deformations from accelerations and may be referenced to slipstream q if a configuration is ever encountered for which they are significant in V/STOL flight.

LINEAR MOMENTUM RATE OF CHANGE

The linear momentum equations are simpler than the angular momentum terms because structural constraints will force the varying incidence mass to translate parallel to the fixed structural components with only a center of gravity shift. Consequently, only the components with significantly high rotation rates need be added to the basic airplane equations.

With the foregoing assumption, the linear momentum equations are

$$\Sigma F = (m_s + m_e)(\dot{V}_s + \Omega_s \times V_s) + m_e \Omega_e \times V_e$$

$$\dot{V}_s + \Omega_s \times V_s = I(\dot{u} + qw - rv) + J(\dot{v} + ru - pw) + K(\dot{w} + pv - qu)$$

$$\Omega_e \times V_e = I(\omega_{x_e} \sin(i_e)\, v) + J(-\omega_{x_e} \sin(i_e)\, w - \omega_{x_e} \cos(i_e)\, u) + K(\omega_{x_e} \cos(i_e)\, v)$$

Collecting components and defining

$$m = m_s + m_e$$

$$\Sigma F_x = m(\dot{u} + qw - rv) + m_e \omega_{x_e} \sin(i_e)\, v$$

$$= F_{x_0} + m a_{g1}$$

$$\Sigma F_y = m(\dot{v} + ru - pw) - m_e \omega_{x_e}(w \sin(i_e) + u \cos(i_e))$$

$$= F_{y_0} + F_{y_{\dot{v}}} \dot{v} + m a_{g2}$$

$$\Sigma F_z = m(\dot{w} + pv - qu) + \omega_{x_e} \cos(i_e)\, v$$

$$= F_{z_0} + F_{z_{\dot{w}}} \dot{w} + m a_{g3}$$

The external forces are, in conventional flight

$$F_{x_0} = -q_s S C_A + F_{x_\delta} + \Delta F_x$$

$$F_{y_0} = q_s S C_y + F_{y_\delta} + \Delta F_y$$

$F_{y_v^\cdot} = (\rho S b/4)\, C_{y_\beta}$

$F_{z_{\dot{w}}} = -(\rho S c/4)\, C_{L_\alpha}$

For V/STOL flight, replace

q_∞ with q^s

C_A with C_A^s

C_y with C_y^s

C_N with C_N^s

Solving for the linear acceleration components, in preperation for numerical integration, results in

$$\dot{u} = rv - qw + g\, a_{31} + F_{x_a}/m - (a_\infty/m)\, \omega_{x_\theta} \sin(i_\theta)\, v$$

$$\dot{v} = [m(pw - ru + g\, a_{32}) + F_{y_a} - a_\infty \omega_{x_\theta} [u \sin(i_\theta) + w \cos(i_\theta)]] / [m - F_{y_v^\cdot}]$$

$$\dot{w} = [m(qu - pv + g\, a_{33}) + F_{z_a} + a_{x_\theta} \cos(i_\theta)\, v] / [m - F_{z_{\dot{w}}}]$$

The load factors, $n_{x_{cg}}$, $n_{y_{cg}}$ and $n_{z_{cg}}$ can be computed at

time and used in an efficient way to compute the effects of center of gravity shifts.

Axial load factor, positive reaction forward (result of an aft acceleration or a forward gravity component)

$$n_{x_{cg}} = -F_{x_a}/GW$$

Lateral load factor, positive reaction to the right (result of a left acceleration or a right-wing-down gravity component)

$$n_{y_{CG}} = -(F_{y_0} + F_{y_{\dot{v}}}\dot{v}) / GW$$

Normal load factor, positive downward reaction (result of an upward acceleration or a downward gravity component)

$$n_{z_{CG}} = -(F_{z_0} + F_{z_{\dot{w}}}\dot{w}) / GW$$

For a center of gravity consider the summation of moments about a base C. G. , denoted by the substrict, 1.

$$r_1 = r_0 + R_{a_1} \times F_a + R_{e_1} \times F_e + + +$$

Where the subscripts, a and e, refer to aerodynamic and engine forces, respectively, and r_0 is a couple, independent of C. G.

A second moment about a different C. G. is

$$r_2 = r_0 + R_{a_2} \times F_a + R_{e_2} \times F_e + + +$$

Subtracting

$$r_2 - r_1 = (R_{a_2} - R_{a_1}) \times F_a + (R_{e_2} - R_{e_1}) \times F_e + + +$$

Obviously,

$$R_{a_2} - R_{a_1} = R_{e_2} - R_{e_1} = \Delta R_{CG}$$

$$r_2 = r_1 + \Delta R_{CG} \times (F_a + F_e + + +)$$

$$F_a + F_e = iF_{x_0} + j(F_{y_0} + F_{y_{\dot{v}}}\dot{v}) + k(F_{z_0} + F_{z_{\dot{w}}}\dot{w})$$

$$= -GW(i\, n_{x_{CG}} + j\, n_{y_{CG}} + k\, n_{z_{CG}})$$

$$\Delta R_{CG} = i\Delta x_{CG} + j\Delta y_{CG} + k\Delta z_{CG}$$

$$\Delta R_{CG} \times (F_a + F_e) = i(GW(n_{y_{CG}} \Delta z_{CG} - n_{z_{CG}} \Delta y_{CG}))$$

$$+ \mathbb{K}[GW(n_{z_{cg}}\Delta x_{cg} - n_{x_{cg}}\Delta z_{cg})]$$

$$+ \mathbb{M}[GW(n_{x_{cg}}\Delta y_{cg} - n_{y_{cg}}\Delta x_{cg})]$$

With this C. G. shift correction added to the previously developed moment equations, the rolling, pitching and yawing accelerations are

$$I_{xx}\dot{p} - I_{xz}\dot{r} + qH_z - rH_y =$$

$$r_{x_0} + r_{x_p}\dot{p} + r_{x_r}\dot{r} + r_{x_v}\dot{v} + GW(n_{y_{cg}}\Delta z_{cg} - n_{z_{cg}}\Delta y_{cg})$$

$$I_{yy}\dot{q} + rH_x - pH_z =$$

$$r_{y_0} + r_{y_q}\dot{q} + r_{y_w}\dot{w} + GW(n_{z_{cg}}\Delta x_{cg} - n_{x_{cg}}\Delta z_{cg})$$

$$-I_{xz}\dot{p} + I_{zz}\dot{r} + pH_y - qH_x =$$

$$r_{z_0} + r_{z_r}\dot{r} + r_{z_p}\dot{p} + r_{z_v}\dot{v} + GW(n_{x_{cg}}\Delta y_{cg} - n_{y_{cg}}\Delta x_{cg})$$

Solving for pitch acceleration

$$\dot{q} = [pH_z - rH_x + r_{y_0} + r_{y_w}\dot{w} + GW(n_{z_{cg}}\Delta x_{cg} - n_{x_{cg}}\Delta z_{cg})]/[I_{yy} - r_{y_q}]$$

The rolling and yawing accelerations must be solved simultaneously for $\dot{p}$ and $\dot{r}$, since the digital computer is not a parallel device.

defining, for compactness,

$$r_{x_1} = rH_y - qH_z + r_{x_0} + r_{x_v}\dot{v} + GW(n_{y_{cg}}\Delta z_{cg} - n_{z_{cg}}\Delta y_{cg})$$

$$r_{z_1} = qH_x - pH_y + r_{z_0} + r_{z_v}\dot{v} + GW(n_{x_{cg}}\Delta y_{cg} - n_{y_{cg}}\Delta x_{cg})$$

The resulting two simultaneous equations that result are

$$(I_{xx} - r_{x_p})\dot{p} - (I_{xz} + r_{x_r})\dot{r} = r_{x_1}$$

$$-(I_{xz} + r_{z_p}\cdot)\,\dot{p} + (I_{zz} - r_{z_r}\cdot)\,\dot{r} = r_{z_1}$$

Solving for the determinant

$$\Delta = (I_{xx} - r_{x_p}\cdot)(I_{zz} - r_{z_r}\cdot) - (I_{xz} + r_{x_r}\cdot)(I_{xz} + r_{z_p}\cdot)$$

Solving for roll acceleration

$$\dot{p} = [(I_{zz} - r_{z_r}\cdot)\,r_{x_1} + (I_{xz} + r_{x_r}\cdot)\,r_{z_1}] / \Delta$$

Solving for yaw acceleration in terms of the known $\dot{p}$

$$\dot{r} = [r_{z_1} + (I_{xz} + r_{z_p}\cdot)\,\dot{p}] / (I_{zz} - r_{z_r}\cdot)$$

DIRECTION COSINE RATES

$$\dot{a}_{11} = a_{12}\,r + a_{13}\,q$$

$$\dot{a}_{12} = a_{13}\,p - a_{11}\,r$$

$$\dot{a}_{13} = a_{11}\,q - a_{12}\,p$$

$$\dot{a}_{21} = a_{22}\,r - a_{23}\,q$$

$$\dot{a}_{22} = a_{23}\,p - a_{21}\,r$$

$$\dot{a}_{23} = a_{21}\,q - a_{22}\,p$$

DIRECTION COSINES

$$a_{ij} = \int \dot{a}_{ij}\,dt$$

$$a_{31} = a_{12}\,a_{23} - a_{13}\,a_{22}$$

$$a_{32} = a_{13}\,a_{21} - a_{11}\,a_{23}$$

$a_{33} \quad a_{11} a_{22} - a_{12} a_{21}$

EULER ANGLES

$\psi = \text{Tan}^{-1}(a_{21}/a_{11})$

$\theta = \text{Sin}^{-1}(-a_{31})$

$\phi = \text{Tan}^{-1}(a_{32}/a_{33})$

EARTH AXIS VELOCITY COMPONENTS

$\dot{x}_e = a_{11} u + a_{12} v + a_{13} w$

$\dot{y}_e = a_{21} u + a_{22} v + a_{23} w$

$\dot{z}_e = a_{31} u + a_{32} v + a_{33} w$

SECTION IV

AERODYNAMIC COEFFICIENT EQUATIONS

AERODYNAMIC COEFFICIENTS

FORCE COEFFICIENT BUILD-UP

TAIL LIFT

$$C_{L_t} = C_{L_{\alpha_t}} (\alpha + \delta_t - \varepsilon) + C_{L_{\delta_e}} \delta_e$$

TAIL DRAG

$$C_{D_t} = C_{D_{O_t}} + C_{D_{C_{L_t}}^2} C_{L_t}^2$$

AXIAL FORCE COEFFICIENT BUILD-UP

$$IC_{X_R}^{\beta} = C_{X_{O_R}}^{\beta} + C_{X_{\beta_{VR}}}^{\beta} + C_{X_{\beta_{SR}}}^{\beta} + C_{X}^{\beta}(\alpha_R)$$

$$IC_{X_L}^{\beta} = C_{X_{O_L}}^{\beta} + C_{X_{\beta_{VL}}}^{\beta} + C_{X_{\beta_{SL}}}^{\beta} + C_{X}^{\beta}(\alpha_L)$$

$$C_{X_{tail}} = -(C_{D_t} \cos\alpha + C_{L_t} \sin\alpha) \left[\frac{S_t}{S_w} \cos\alpha \right]$$

$$+ (C_{L_t} \cos\alpha - C_{D_t} \sin\alpha) \left[\frac{S_t}{S_w} \sin\alpha \right]$$

NORMAL FORCE COEFFICIENT BUILD-UP

$$IC_{N_R} = C_{N_{O_R}}^{\beta} + C_{N_{\beta_{VR}}}^{\beta} + C_{N_{\beta_{SR}}}^{\beta} + C_{N}^{\beta}(\alpha_R)$$

$$IC_{N_L} = C_{N_{O_L}}^{\beta} + C_{N_{\beta_{VL}}}^{\beta} + C_{N_{\beta_{SL}}}^{\beta} + C_{N}^{\beta}(\alpha_L)$$

$$C_{N_{tail}} = (C_{L_t} \cos\epsilon - C_{D_t} \sin\epsilon) \left(\frac{S_t}{S_w} \cos\alpha\right) + (C_{D_t} \cos\epsilon + C_{L_t} \sin\epsilon) \left(\frac{S_t}{S_w} \sin\alpha\right)$$

$$C_N{}^{s}_{(\alpha_{NF})} = \frac{\partial C_N{}^{s}}{\partial \sin\alpha_{NF}} \left(1 - T_C{}^{s}_{NF}\right) \sin\alpha_{NF}$$

MOMENT COEFFICIENT BUILD-UP

PITCHING

$$\Sigma C^{s}_{m_R} = C^{s}_{m_{OR}} + C^{s}_{m_{\delta_{VR}}} + C^{s}_{m_{\delta_{SR}}} + C^{s}_{m_{(\alpha_R)}}$$

$$\Sigma C^{s}_{m_L} = C^{s}_{m_{OL}} + C^{s}_{m_{\delta_{VL}}} + C^{s}_{m_{\delta_{SL}}} + C^{s}_{m_{(\alpha_L)}}$$

YAWING

$$C_{n_{\delta a}} = C_{n_{\delta a_0}} + \frac{\partial C_{n_{\delta a}}}{\partial T_c{}^{s}} \frac{\left[T_c{}^{s}_{R} + T_c{}^{s}_{L}\right]}{2}$$

SECTION V

AERODYNAMIC AND THRUST FORCE EQUATIONS

AERODYNAMIC AND THRUST FORCES

AXIAL (FORWARD)

$$F_{x_o} = \frac{A_F}{2} q^s_R \Sigma C_{x^2_R} + \frac{A_F}{2} q^s_L \Sigma C_{x^s_L} + K_{x_{NF}} q^s_{NF} A_{NF} C_{x^s_{O_{NF}}}$$

$$+ (K_t \eta_t) q_a S_w C_{x_{tail}} + K_{ts} \cos(i_e) T_j + \Delta F$$

LATERAL (SIDE)

$$F_{y_o} = q^s_{AV} S_w C_{y^s_\beta} \beta + q_a S_w \left[C_{y_{\delta_R}} \delta_R + C_{y_{\delta_a}} (\delta_{a_L} - \delta_{a_R}) \right]$$

$$+ \frac{\rho V_T S_w b}{4} C_{y_r} r + \left(\frac{\partial Y}{\partial V} v + \frac{\partial Y}{\partial r} r - \frac{\rho V_T}{2} (C_D S_w) v \right) \text{[POF1]}$$

VERTICAL (NEGATIVE NORMAL)

$$F_{z_o} = -\frac{A_F}{2} q^s_R \Sigma C_{N_R} - \frac{A_F}{2} q^s_L \Sigma C_{N_L} - \frac{\rho V_T S_w c}{4} C_{L_q} q$$

$$- K_{N_{NF}} q^s_{NF} A_{NF} \left[C_N{}^s_{O_{NF}} + C_N{}^s_{(\alpha_{NF})} \right] - (K_t \eta_t) q_a S_w C_{N_{tail}}$$

$$- K_{ts} \sin(i_e) T_j - \left[\frac{\partial N}{\partial |u|} |u| + \frac{\partial N}{\partial |v|} |v| \right] \text{[POF1]}$$

$$+ q^s_{AV} A_F \Delta C_N \left(\frac{w}{\sqrt{u^2 + w^2}} \right) \text{[POF2]}$$

SECTION VI

AERODYNAMIC AND THRUST MOMENTS

AERODYNAMIC AND THRUST MOMENTS

ROLLING

$$T_{x_o} = q^s_{AV} S_w b C_{\ell}{}^s_{\beta} \beta + \frac{\rho V_T S_w b^2}{4} (C_{\ell_p} p + C_{\ell_r} r)$$

$$+ q_a S_w b [C_{\ell_{\delta_a}} (\delta_{a_L} - \delta_{a_R}) + C_{\ell_{\delta_r}} \delta_r]$$

$$+ \frac{A_F}{2} q^s_L \Sigma C_N{}^s_L Y_F - \frac{A_F}{2} q^s_R \Sigma C_N{}^s_R Y_F$$

$$- \frac{A_F}{2} Y_F \left[q^s_L C_N{}^s_{(\alpha_L)} - q^s_R C_N{}^s_{(\alpha_R)} \right] [POF1]$$

$$+ \left(\frac{\partial L}{\partial v} v + \frac{\partial L}{\partial p} p \right) [POF1]$$

PITCHING

$$T_{y_o} = \frac{A_F}{2} D_F q^s_R \Sigma C_{m_R} + \frac{A_F}{2} D_F q^s_L \Sigma C_{m_L} + q_a S_w c C_{m_\beta} |\beta|$$

$$+ K_{M_{NF}} q^s_{NF} A_{NF} X_{NF} \left[C^s_{N_{O_{NF}}} + C^s_{N_{(\alpha_{NF})}} \right]$$

$$+ \left(\frac{\partial m}{\partial u} \right) |u| [POF1]$$

$$- (K_t \eta_t) q_a S_w c \left[\frac{\ell_t}{c} C_{N_{tail}} + \frac{Z_t}{c} C_{x_{tail}} \right]$$

$$+ \frac{\rho V_T S_w c^2}{4} C_{m_q} q + K_{TS} T_j [Z_j \cos(i_e) - \ell_j \sin(i_e)]$$

YAWING

$$T_{z_o} = q^s_{AV} S_w b C_{n_\beta}{}^s \beta + q_a S_w b \left| C_{n_{\delta_a}} (\delta_{a_L} - \delta_{a_R}) + C_{n_{\delta_r}} \delta_r \right|$$

$$+ \frac{\rho V_T S_w b^2}{4} (C_{n_r} r + C_{n_p} p) + \frac{A_T}{2} q^s_L \Sigma C^s_{x_{(L)}} Y_F$$

$$- \frac{A_T}{2} q^s_R \Sigma C^s_{x_R} Y_F - \left[\frac{A_T}{2} q^s_L C^s_{x_{(\alpha_L)}} Y_F - \frac{A_T}{2} q^s_R C^s_{x_{(\alpha_R)}} Y_F \right] \cdot$$

$$[POF1] + \left[\frac{\partial \eta}{\partial V} v + \frac{\partial \eta}{\partial \left[\frac{\rho V_T v}{2} \right]} \rho \frac{V_T}{2} v + \frac{\partial \eta}{\partial r} MF\ r \right] [POF1]$$

$$+ \frac{\partial \eta_{NF}}{\partial (X^2_{NF} r)} X^2_{NF}\ r$$

SECTION VII

AERODYNAMIC ANGLES

AERODYNAMIC ANGLES

ANGLE OF ATTACK

$$\alpha = \mathrm{Tan}^{-1}\,(w/u),\ u > 0$$

$$= w\pi/|w| + \mathrm{Tan}^{-1}(w/u),\ u < 0,\ (w/|w| = 0,\ w = 0)$$

$$= w\pi/2|w|,\ u = 0,\ (w/|w| = 0,\ w = 0)$$

$$= \alpha_{max}(\alpha/|\alpha|),\ \ |\alpha| > \alpha_{max},\ \neq 0$$

ANGLE OF ATTACK, RIGHT FAN

$$\alpha_R = \mathrm{Tan}^{-1}\left(\frac{w + pY_F}{u - rY_F}\right),\ u - rY_F > 0$$

$$= \frac{(w + pY_F)}{|w + pY_F|}\,\pi + \mathrm{Tan}^{-1}\left(\frac{w + pY_F}{u - rY_F}\right),\ u - rY_F < 0,$$

$$\left(\frac{w + pY_F}{|w + pY_F|} = 0,\ w + pY_F = 0\right)$$

$$= \frac{(w + pY_F)}{|w + pY_F|}\cdot\frac{\pi}{2},\ u - rY_F = 0,\left(\frac{w + pY_F}{|w + pY_F|} = 0,\ w + pY_F = 0\right)$$

$$= \alpha_{max}\,(\alpha_R/|\alpha_R|),\ |\alpha_R| > \alpha_{max}$$

ANGLE OF ATTACK, LEFT FAN

$$\alpha_L = \mathrm{Tan}^{-1}\left(\frac{w - pY_F}{u + rY_F}\right),\ u + rY_F > 0$$

$$\alpha_L = \frac{(w - pY_p)}{|w - pY_p|}\,\pi + \mathrm{Tan}^{-1}\left(\frac{w - pY_p}{u + rY_p}\right),\ u + rY_p < 0,$$

$$\left(\frac{w - pY_p}{|w - pY_p|} = 0,\ w - pY_p = 0\right)$$

$$= \frac{(w + pY_p)}{|w + pY_p|}\,\frac{\pi}{2},\ u + rY_p = 0,\ \left(\frac{w - pY_p}{|w - pY_p|} = 0,\ w - pY_p = 0\right)$$

$$= \alpha_{max}\,(\alpha_L/|\alpha_L|),\quad \alpha > \alpha_{max}$$

ANGLE OF ATTACK, NOSE FAN

$$\alpha_{NF} = \mathrm{Tan}^{-1}\left(\frac{w - X_{NF}q}{u}\right),\ u > 0$$

$$= \frac{(w - X_{NF}q)}{|w - X_{NF}q|}\,\pi + \mathrm{Tan}^{-1}\left(\frac{w - X_{NF}q}{u}\right),\quad u < 0$$

$$= \frac{(w - X_{NF}q)}{|w - X_{NF}q|}\,\frac{\pi}{2},\ u = 0$$

$$= \alpha_{max}\,(\alpha_{NF}/|\alpha_{NF}|)\quad |\alpha_{NF}| > \alpha_{max}$$

SIDESLIP ANGLE

$$\beta = \mathrm{Tan}^{-1}\frac{v}{\sqrt{u^2 + w^2}},\ u^2 + w^2 \neq 0,\ u \geq 0$$

$$= \frac{v}{|v|}\,\pi - \mathrm{Tan}^{-1}\frac{v}{\sqrt{u^2 + w^2}},\ u^2 + w^2 \neq 0,\ u < 0$$

$$= \frac{v}{|v|}\,\frac{\pi}{2},\ u^2 + w^2 = 0$$

$$= (\beta_{max})\,(\beta/|\beta|),\ |\beta| > \beta_{max}$$

SECTION VIII

DYNAMIC PRESSURE, THRUST COEFFICIENTS, AIRSPEED EQUATIONS

DYNAMIC PRESSURE, THRUST COEFFICIENTS, AIRSPEED

AMBIENT DYNAMIC PRESSURE

$$\lambda = (1 - 0.000006879h)^{5.256}, \quad h < 35{,}332 \text{ ft.}$$

$$= 10^{(4705 - h)/48211}, \quad h \geq 35{,}332 \text{ ft.}$$

$$V_s = 1116.016\ (1 - 0.000006879h)^{1/2}, \quad h < 35{,}332 \text{ ft.}$$

$$= 970.9579, \quad h \geq 35{,}332 \text{ ft.}$$

$$\rho = 2(.0481\lambda)\ V_s^2$$

$$q_a = 1/2(\rho V_T^2)$$

SLIPSTREAM DYNAMIC PRESSURES

$$q^e_R = T_{000_R} / (A_p/2) + q_a$$

$$q^e_L = T_{000_L} / (A_p/2) + q_a$$

$$q^e_{NF} = T_{000_{NF}} / A_{NF} + q_a$$

$$q^e_{AV} = (q^e_R + q^e_L)/2$$

THRUST COEFFICIENTS

$$Tc^e_R = T_{000_R} / (A_p\ q^e_R/2)$$

$$Tc^e_L = T_{000_L} / (A_p\ q^e_L/2)$$

$$Tc^e = 1/2\ (Tc^e_R + Tc^e_L)$$

$$Tc^e_{NF} = (T_{000_{NF}} / A_{NF}) / q^e_{NF}$$

$$POF1 = 1, \quad Tc^e > 0.99$$

$$= 1 + 100\ (Tc^e - 0.99), \quad .99 \geq Tc^e > .98$$

$$= 0, \quad Tc^e \leq .98$$

$$POF2 = 100\ (1 - Tc^{8}), \quad Tc^{8} > .99$$

$$= POF1, \quad Tc^{8} \leq .99$$

AIRSPEED

$$V_T = \sqrt{u^2 + v^2 + w^2}$$

SECTION IX

THRUST COMPUTATIONS

THRUST COMPUTATIONS

TURBOJET THRUST

$$T_j = T_{j_{100}} + T_{j_{N_G}} (N_G - 100) + T_{j_{N_{G2}}} (N_G - 100)^2$$

WING FAN POWER

$$P_F = P_{F_{100}} + P_{F_{N_G}} (N_G - 100) + P_{F_{N_{G2}}} (N_G - 100)^2$$

WING FAN THRUST BY SUCCESSIVE APPROXIMATIONS

$$F = -\rho^{\frac{1}{3}} \left[\frac{P_F/A_F}{\frac{C_p^s}{C_p S_0} + \frac{\Delta C_p^s}{C_p S_0}} \right]^{\frac{2}{3}}$$

$$G = -\frac{2}{3} \left[\frac{F}{\frac{C_p^s}{C_p S} + \frac{\Delta C_p^s}{C_p S_0}} \right]$$

$$q_s = q_s + 2T_{000}/A_F$$

T_{000} initially guessed = (2) (GW)

$$T_c^s = 2T_{000}/(A_F q^s)$$

$$R_q = 1 - T_c^s$$

START COMPUTATION CYCLE

$$c_F = 2T_{000}/A_F + F$$

$$\frac{\partial\left[C_p^*/C_{p_0}^*\right]}{\partial T_c^*}$$

[Computed by numerical differentiation of tables from Figure 73]

$$\left[\frac{\partial c_T}{\partial T_c^*}\right] = q^* - q_a T_c^* + G \frac{\partial\left[C_p^*/C_{p_0}^*\right]}{\partial T_c^*}$$

$$T_{c\,(COR)}^* = T_c^* - c_T \Big/ \left[\frac{\partial c_T}{\partial T_c^*}\right]$$

$$R_q = 1 - T_{c\,(COR)}^*$$

$$q^* = q_a R_q$$

$$T_{000} = \frac{A_T}{2} q^* T_c^*$$

CONTINUE CYCLE

SECTION X

TRIM COMPUTATIONS

The necessity for trimming the airplane, to initialize each time history with all acceleration components equal to zero, always requires repetitive hand calculation or graphical iteration for the non-linear configurations that are encountered in engineering practice. To obviate the tedium of trimming by hand, and to enhance the computer turn-around time, trimmed values for

$$\beta_v,\ \beta_s \text{ and } \delta_B$$

in VTOL flight are computed automatically by one of the programmed options.

The method of successive approximations, as opposed to an interation technique, is the most efficient procedure for computing the values of vector, stagger and nose fan bucket positions that will cause all acceleration components to vanish. These trimmed values are required at each time history initiation and, additionally, are desirable for performance information.

The successive approximation technique employs the following truncated Taylor's series formulae.

$$\begin{bmatrix} \frac{\partial \epsilon_x}{\partial \beta_v} & \frac{\partial \epsilon_x}{\partial \beta_s} & \frac{\partial \epsilon_x}{\partial \delta_B} \\ \frac{\partial \epsilon_z}{\partial \beta_v} & \frac{\partial \epsilon_z}{\partial \beta_s} & \frac{\partial \epsilon_z}{\partial \delta_B} \\ \frac{\partial \epsilon_M}{\partial \beta_v} & \frac{\partial \epsilon_M}{\partial \beta_s} & \frac{\partial \epsilon_M}{\partial \delta_B} \end{bmatrix} \begin{pmatrix} \Delta\beta_v \\ \Delta\beta_s \\ \Delta\delta_B \end{pmatrix} = \begin{pmatrix} -(F_{x_o} - GW \sin\theta) \\ -(F_{z_o} + GW \cos\theta) \\ -M_o \end{pmatrix}$$

$$\beta_{v_R} = \beta_{v_o} + \Delta\beta_v$$

$$\beta_{v_L} = \beta_{v_R}$$

$$\beta_{s_R} = \beta_{s_o} + \Delta\beta_s$$

$$\beta_{s_L} = \beta_{s_R}$$

$$\delta_B = \delta_{B_o} + \Delta\delta_B$$

$$\frac{\partial c_x}{\partial \delta_v} = A_f q^* \quad \text{(Computed by numerical differentiation of tables from Figure 67.)}$$

$$\frac{\partial c_x}{\partial \delta_s} = A_f q^* \quad \text{(Computed by numerical differentiation of tables from Figure 68.)}$$

$$\frac{\partial c_x}{\partial \delta_B} = A_{NF} q^*_{NF} \; C_x^{*}{}_{\delta_{NF}} \left(\frac{\partial K_{x_{NF}}}{\partial \delta_B} \right)$$

$$\frac{\partial c_z}{\partial \delta_v} = - A_f q^* \quad \text{(Computed by numerical differentiation of tables from Figure 69.)}$$

$$\frac{\partial c_z}{\partial \delta_s} = - A_f q^* \quad \text{(Computed by numerical differentiation of tables from Figure 70.)}$$

$$\frac{\partial c_z}{\partial \delta_B} = - A_{NF} q^*_{NF} \left[C_{n_{o_{NF}}} + C_{n_{\alpha_{NF}}} \right] \left(\frac{\partial K_{z_{NF}}}{\partial \delta_B} \right)$$

$$\frac{\partial c_M}{\partial \delta_v} = A_f D_f q^* \quad \text{(Computed by numerical differentiation of tables from Figure 71.)}$$

$$\frac{\partial c_M}{\partial \delta_s} = A_f D_f q^* \quad \text{(Computed by numerical differentiation of tables from Figure 72.)}$$

$$\frac{\partial c_M}{\partial \delta_B} = A_{NF} q^*_{NF} X_{NF} \left[C_{m_{o_{NF}}} + C_{n_{(\alpha NF)}} \right] \left(\frac{\partial K_{M_{NF}}}{\partial \delta_B} \right)$$

$$= - X_{NF} \frac{\partial c_z}{\partial \delta_B}$$

For conventional flight, the same mathematical technique is used to solve for trimmed values of angle of attack (α), horizontal tail incidence (δ_H), and thrust required (T_j).

$$\begin{bmatrix} \frac{\partial c_x}{\partial \alpha} & \frac{\partial c_x}{\partial \delta H} & \frac{\partial c_x}{\partial T_j} \\ \frac{\partial c_z}{\partial \alpha} & \frac{\partial c_z}{\partial \delta H} & \frac{\partial c_z}{\partial T_j} \\ \frac{\partial c_M}{\partial \alpha} & \frac{\partial c_M}{\partial \delta H} & \frac{\partial c_M}{\partial T_j} \end{bmatrix} \begin{Bmatrix} \Delta\alpha \\ \Delta\delta H \\ \Delta T_j \end{Bmatrix} = \begin{Bmatrix} -(F_{x_o} - GW \sin\theta) \\ -(F_{z_o} + GW \cos\theta) \\ -M_o \end{Bmatrix}$$

$$\alpha = \alpha_o + \Delta\alpha$$

$$\delta H = \delta H_o + \Delta\delta H$$

$$T_j = T_{j_o} + \Delta T_j$$

$$\frac{\partial c_x}{\partial \alpha} = A_y \, q_{avg} \frac{\partial C_x}{\partial \alpha} + AKTNT \, q_a \, S_W \frac{\partial C_{x_t}}{\partial \alpha}$$

$$\frac{\partial c_x}{\partial \delta_H} = AKTNT \, q_a \, S_W \frac{\partial C_{x_t}}{\partial \delta_H}$$

$$\frac{\partial c_x}{\partial T_j} = AKTS \cos(AIE)$$

$$\frac{\partial c_z}{\partial \alpha} = -A_y \, q_{avg} \frac{\partial C_N}{\partial \alpha} - AKTNT \, q_a \, S_W \frac{\partial C_{N_t}}{\partial \alpha}$$

$$\frac{\partial c_z}{\partial \delta_H} = -AKTNT \, q_a \, S_W \frac{\partial C_{N_t}}{\partial \delta_H}$$

$$\frac{\partial c_g}{\partial T_j} = -AKTS \; Sin(AIE)$$

$$\frac{\partial c_M}{\partial \alpha} = A_F \; D_F \; q_{avg} \frac{\partial C_M}{\partial \alpha} - AKTNT \; q_a \; S_W \; \bar{c} \left(\ell_t \frac{\partial C_{M_t}}{\partial \alpha} + Z_t \frac{\partial C_{x_t}}{\partial \alpha} \right)$$

$$\frac{\partial c_M}{\delta_H} = - AKTNT \; q_a \; S_W \; \bar{c} \left(\ell_t \frac{\partial C_{M_t}}{\partial \delta_H} + Z_t \frac{\partial C_{x_t}}{\partial \delta_H} \right)$$

$$\frac{\partial c_M}{\partial T_j} = AKTS \; [ZJ \; Cos(AIE) - ALJ \; Sin(AIE)]$$

$\frac{\partial C_x}{\partial \alpha}$ (Computed by numerical differentiation of tables from Figure 78.)-

$$\frac{\partial C_{x_t}}{\partial \alpha} = \left(1 - \frac{\partial \epsilon}{\partial \alpha}\right) C_{N_t} - \frac{S_t}{S_W} \left(\frac{\partial C_{D_t}}{\partial \alpha} Cos(\epsilon - \alpha) + \frac{\partial C_{L_t}}{\partial \alpha} Sin(\epsilon - \alpha) \right)$$

$$\frac{\partial C_{x_t}}{\partial \delta_H} = - \frac{S_t}{S_W} \left[\frac{\partial C_{D_t}}{\partial \delta_H} Cos(\epsilon - \alpha) + \frac{\partial C_{L_t}}{\partial \delta_H} sin(\epsilon - \alpha) \right]$$

$$\frac{\partial C_{N_t}}{\partial \alpha} = \left(1 - \frac{\partial \epsilon}{\partial \alpha}\right) C_{x_t} + \frac{S_t}{S_W} \left[- \frac{\partial C_{D_t}}{\partial \alpha} Sin(\epsilon - \alpha) + \frac{\partial C_{L_t}}{\partial \alpha} Cos (\epsilon - \alpha) \right]$$

$$\frac{\partial C_{N_t}}{\partial \delta_H} = \frac{S_t}{S_W} \left[- \frac{\partial C_{D_t}}{\partial \delta_H} Sin(\epsilon - \alpha) + \frac{\partial C_{L_t}}{\partial \delta_H} Cos (\epsilon - \alpha) \right]$$

$\frac{\partial C_N}{\partial \alpha}$ (Computed by numerical differentiation of tables from Figure 79.)

$\frac{\partial C_M}{\partial \alpha}$ (Computed by numerical differentiation of tables from Figure 77.)

$\left(1 - \frac{\partial \epsilon}{\partial \alpha}\right)$ (Computed by numerical differentiation of tables from Figure 66.)

$$\frac{\partial C_{L_t}}{\partial \alpha} = C_{L_{\alpha_t}} \left(1 - \frac{\partial \epsilon}{\partial \alpha}\right)$$

$$\frac{\partial C_{D_t}}{\partial \alpha} = 2(CDCL2T)\, C_{L_T} \frac{\partial C_{L_T}}{\partial \alpha}$$

$$\frac{\partial C_{L_t}}{\partial \delta_H} = C_{L_{\alpha_t}}$$

$$\frac{\partial C_{D_t}}{\partial \delta_H} = 2(CDCL2T)\, C_{L_T} \frac{\partial C_{L_t}}{\partial \delta_H}$$

SECTION XI
GEOMETRIC DATA

GW	9200	lb
S_w	260	ft^2
b_w	29.83	ft
$\bar{c}$	9.4	ft
S_t	52.86	ft^2
$l_t/\bar{c}$	2.192	
$z_t/\bar{c}$	.8319	
A_F	42.6	ft^2
D_F	5.2	ft
Y_F	5.07	ft
A_{HF}	7.07	ft^2
X_{HF}	15.6	ft
l_j	14.02	ft
z_j	1.531	ft
i_e	.104	rad.
I_x	4252	slug-ft^2
I_y	15139	slug-ft^2
I_z	17418	slug-ft^2
I_x - Fan	30.2	slug-ft^2
I_z - Fan	15	slug-ft^2
m_F	15	slug

SECTION XII

AERODYNAMIC COEFFICIENT CURVES

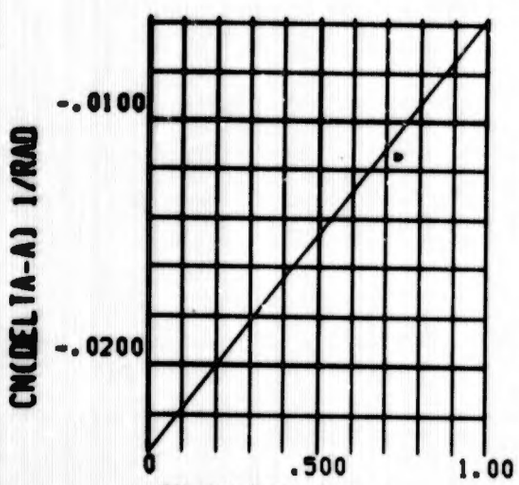

FIG 55 YAWING MOMENT COEFF. INCREMENT WITH AILERON ANGLE

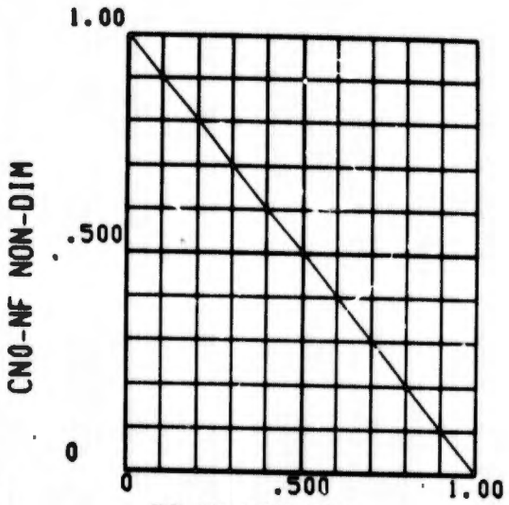

FIG 56 NORMAL FORCE COEFF. DUE TO THE NOSE FAN

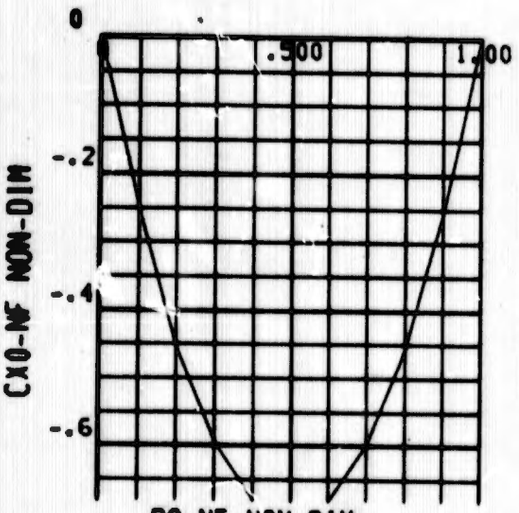

FIG 57 AXIAL FORCE COEFF. DUE TO THE NOSE FAN

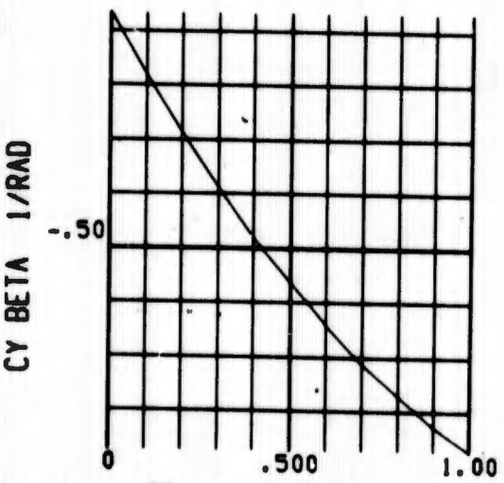

FIG 58 SIDE FORCE COEFF. STABILITY DERIVATIVE

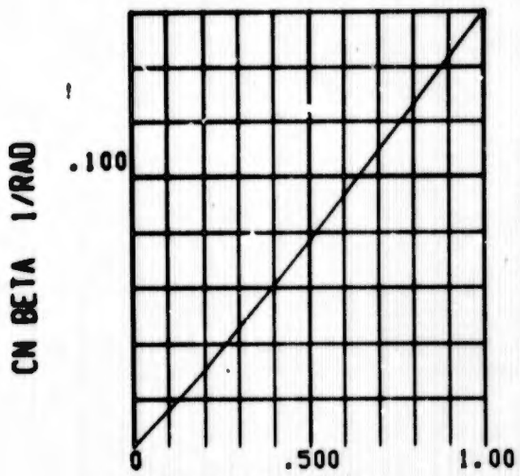

FIG 59 DIRECTIONAL STABILITY

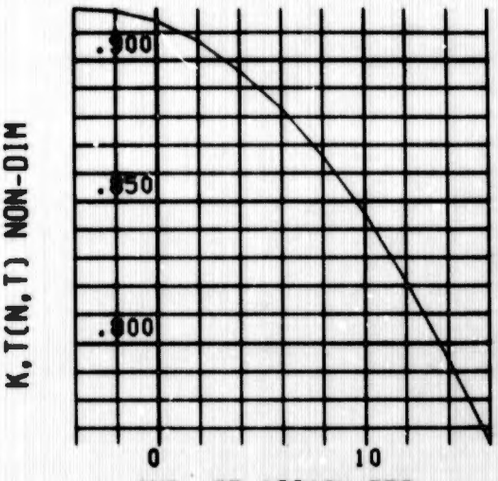

FIG 60 HORIZONTAL TAIL EFFICIENCY FACTOR

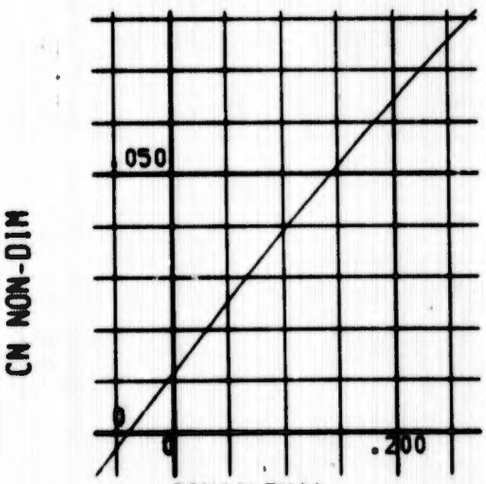

FIG 61 NORMAL FORCE COEFF. INCREMENT W/ SIN(ALPHA), HOVER

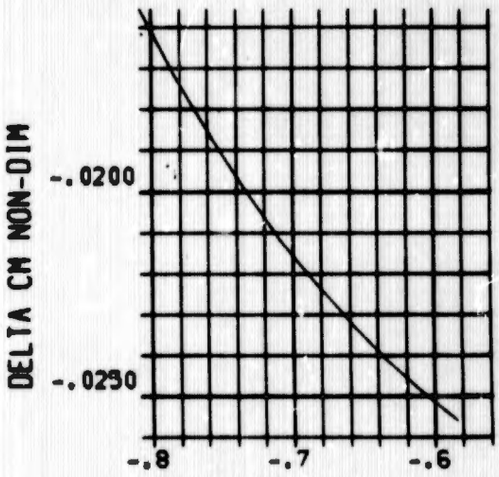

FIG 62 PITCHING MOMENT COEFF. WITH SIN(ALPHA-50), HOVER

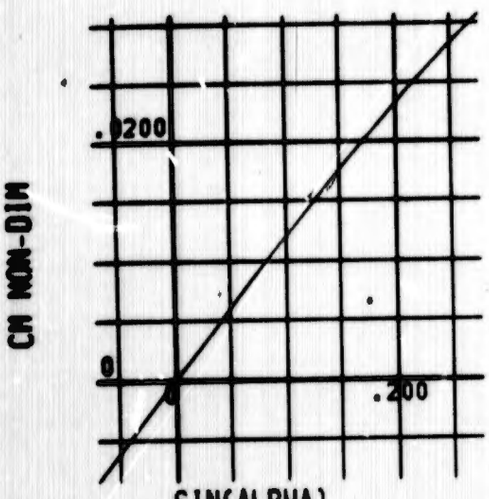

FIG 63 PITCHING MOMENT COEFF. INCREMENT W/ SIN(ALPHA), HOVER

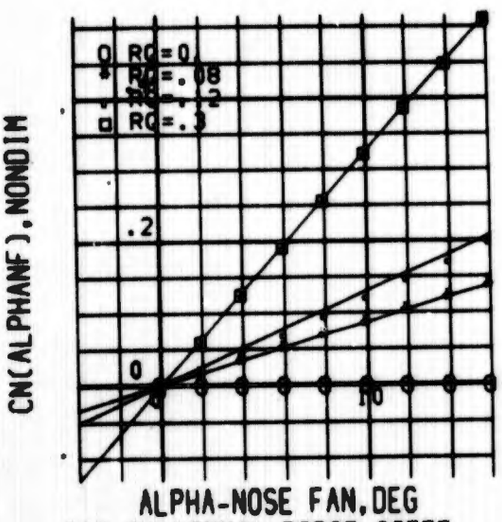

FIG 64 NORMAL FORCE COEFF. INCREMENT WITH ALPHA-NOSE FAN

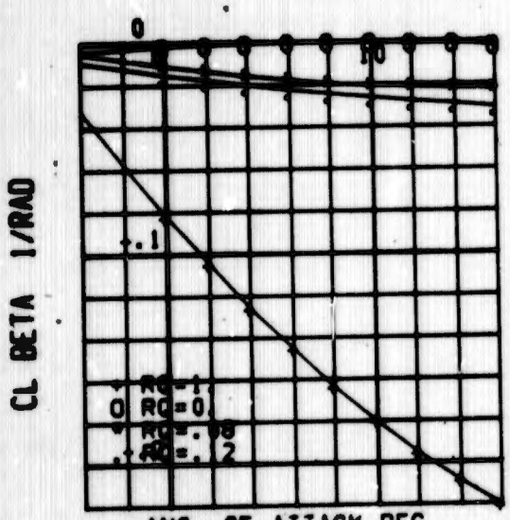

FIG 65 EFFECTIVE DIHEDRAL

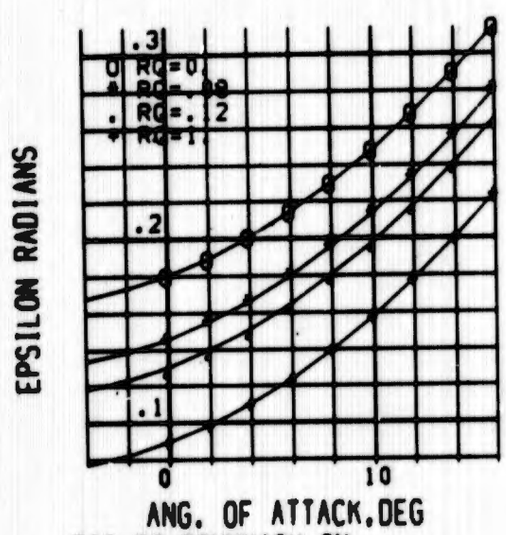

FIG 66 DOWNWASH ON HORIZONTAL TAIL

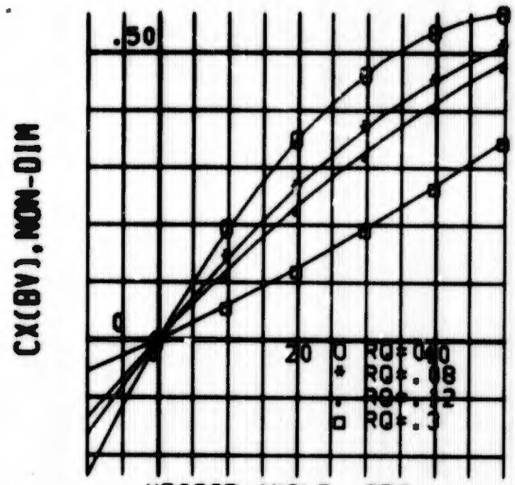

FIG 67 AXIAL FORCE COEFF. INCREMENT WITH VECTOR ANGLE

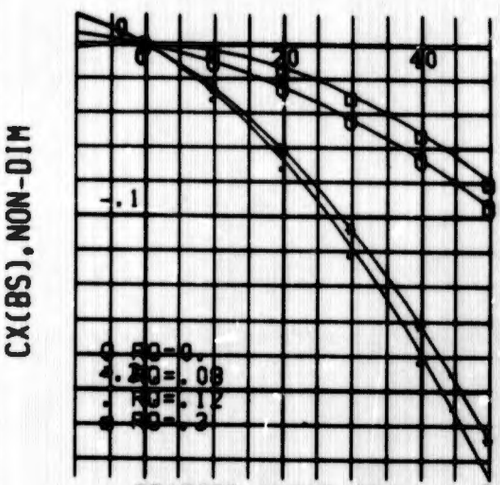

FIG 68 AXIAL FORCE COEFF. INCREMENT WITH STAGGER ANGLE

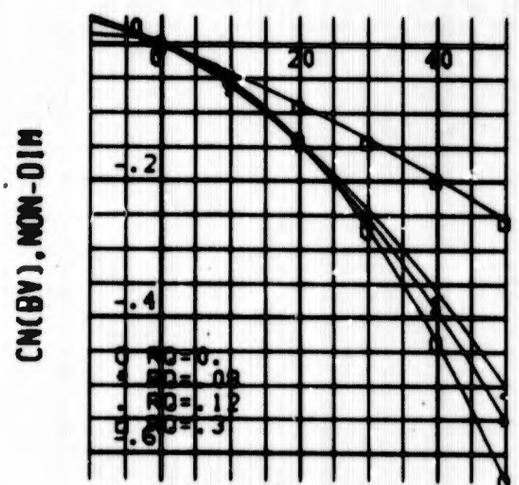

FIG 69 NORMAL FORCE COEFF. INCREMENT WITH VECTOR ANGLE

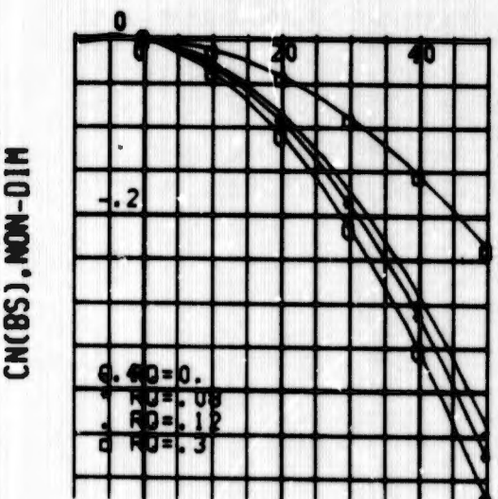

FIG 70 NORMAL FORCE COEFF. INCREMENT WITH STAGGER ANGLE

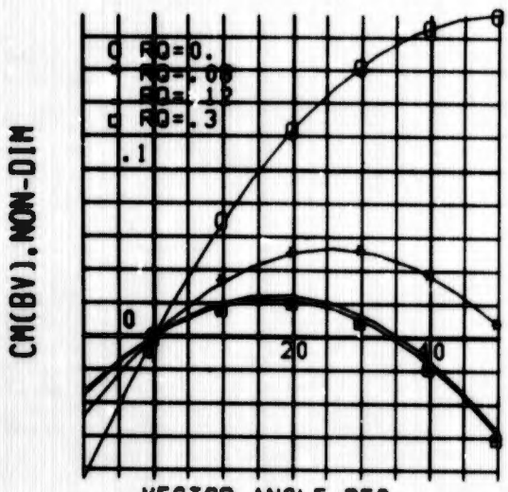

VECTOR ANGLE,DEG

FIG 71 PITCHING MOMENT COEFF. INCREMENT WITH VECTOR ANGLE

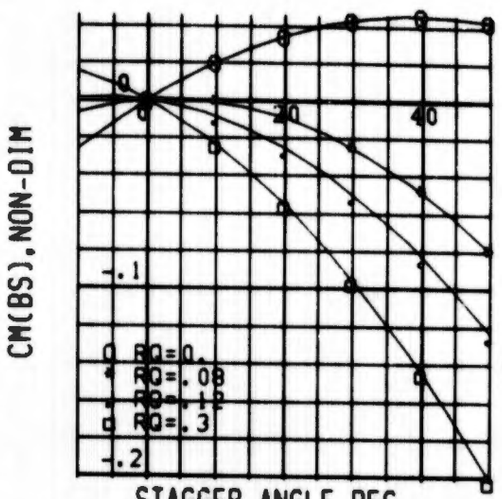

STAGGER ANGLE,DEG

FIG 72 PITCHING MOMENT COEFF. INCREMENT WITH STAGGER ANGLE

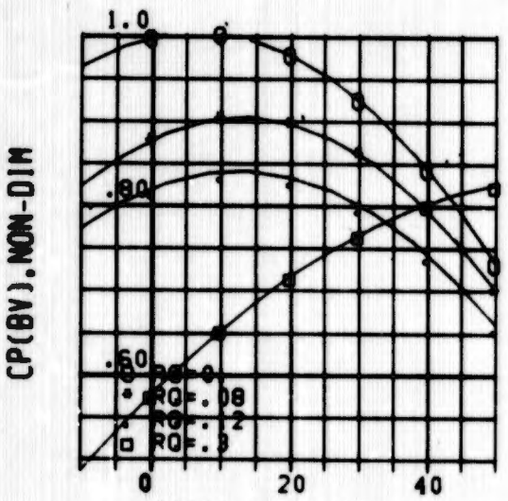

VECTOR ANGLE,DEG

FIG 73 POWER COEFFICIENT INCREMENT WITH VECTOR ANGLE

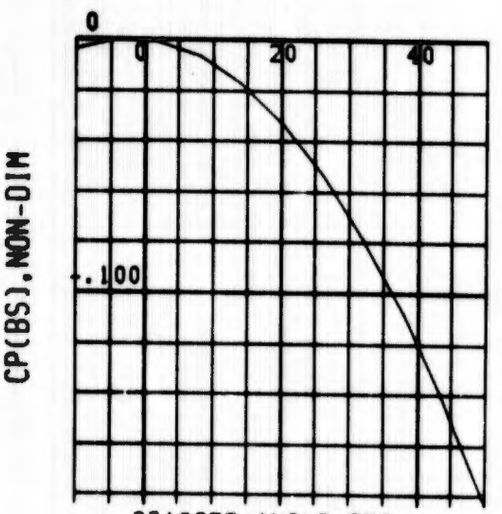

STAGGER ANGLE,DEG

FIG 74 POWER COEFFICIENT INCREMENT WITH STAGGER ANGLE

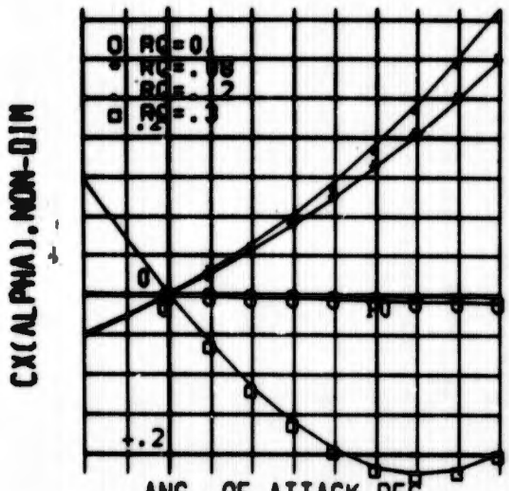

ANG. OF ATTACK,DEG

FIG 75 AXIAL FORCE COEFF. VERSUS ALPHA, VECTOR=-10

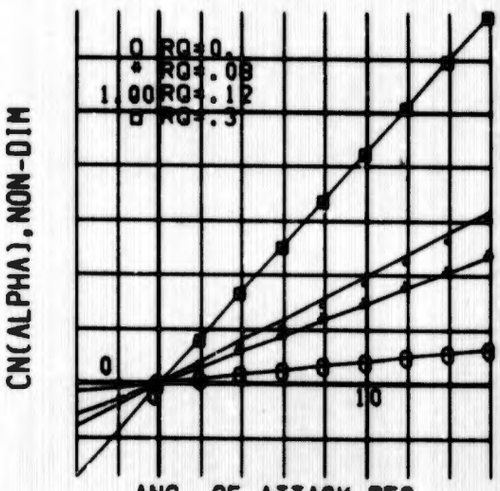

ANG. OF ATTACK,DEG

FIG 76 NORMAL FORCE COEFF. VERSUS ALPHA, VECTOR=-10

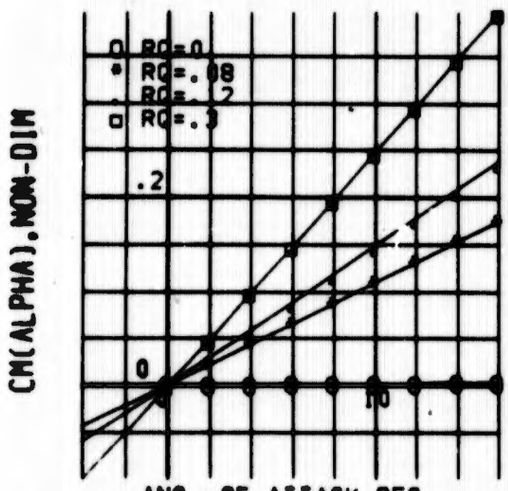

ANG. OF ATTACK,DEG

FIG 77 PITCHING MOMENT COEFF. INCREMENT WITH ALPHA

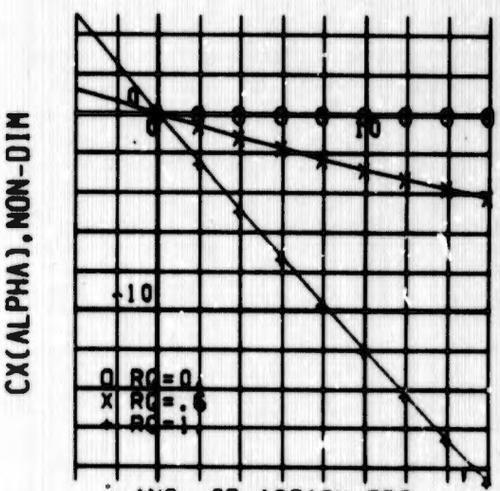

ANG. OF ATTACK,DEG

FIG 78 AXIAL FORCE COEFF. VERSUS ALPHA, VECTOR=0

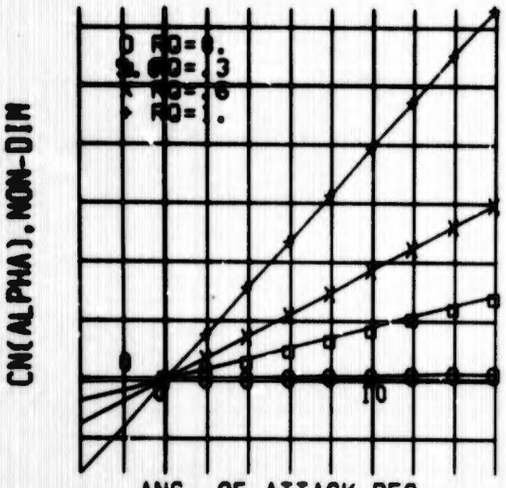

FIG 79 NORMAL FORCE COEFF.
VERSUS ALPHA, VECTOR=0

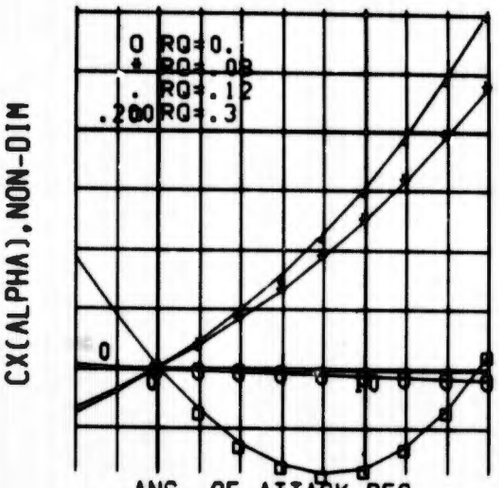

FIG 80 AXIAL FORCE COEFF.
VERSUS ALPHA, VECTOR=10

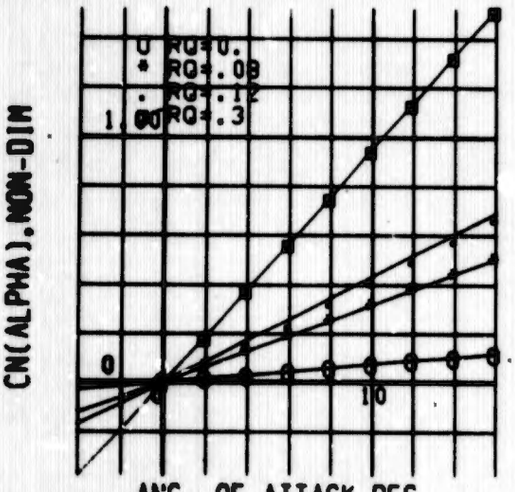

FIG 81 NORMAL FORCE COEFF.
VERSUS ALPHA, VECTOR=10

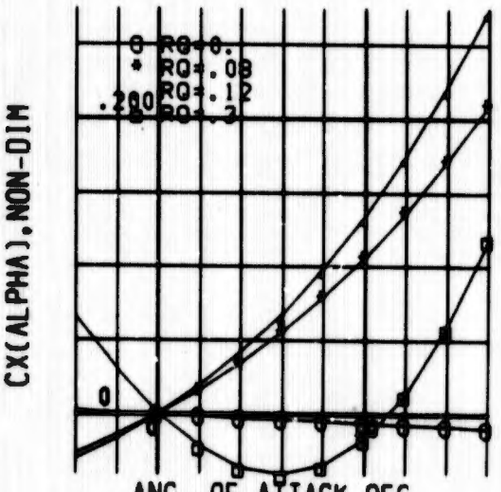

FIG 82 AXIAL FORCE COEFF.
VERSUS ALPHA, VECTOR=20

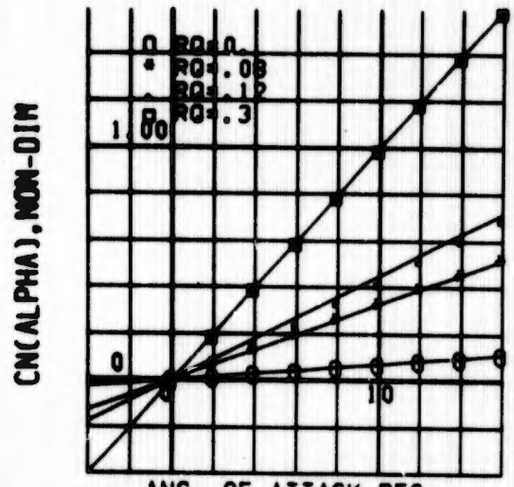

FIG 83 NORMAL FORCE COEFF. VERSUS ALPHA, VECTOR=20

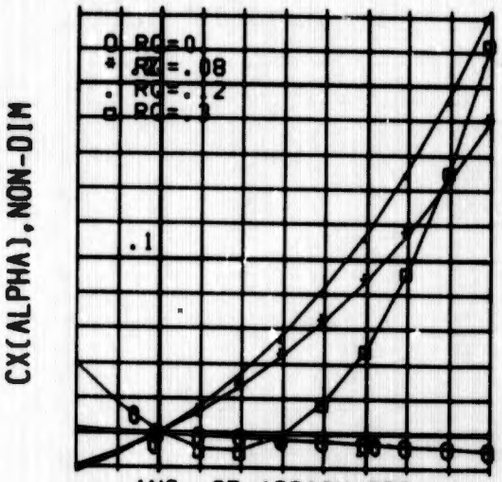

FIG 84 AXIAL FORCE COEFF. VERSUS ALPHA, VECTOR=30

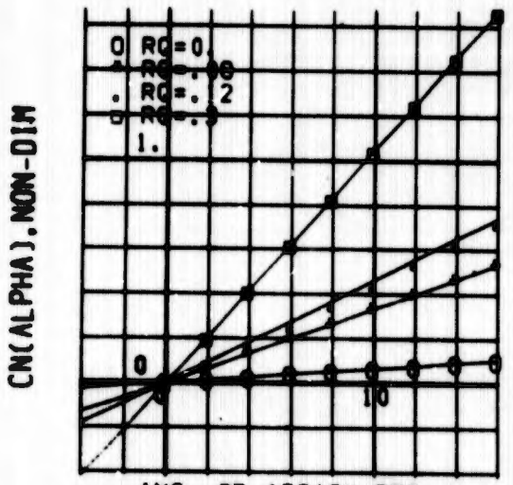

FIG 85 NORMAL FORCE COEFF. VERSUS ALPHA, VECTOR=30

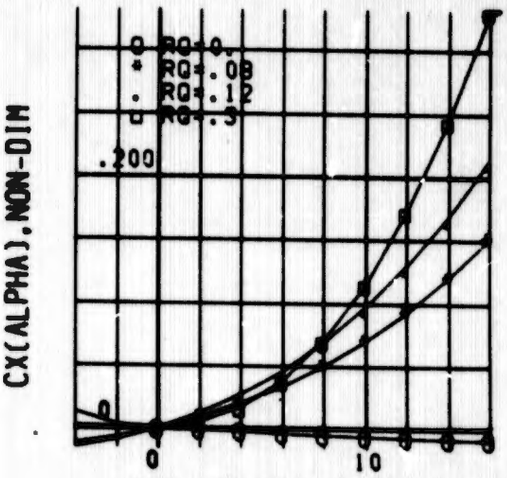

FIG 86 AXIAL FORCE COEFF. VERSUS ALPHA, VECTOR=40

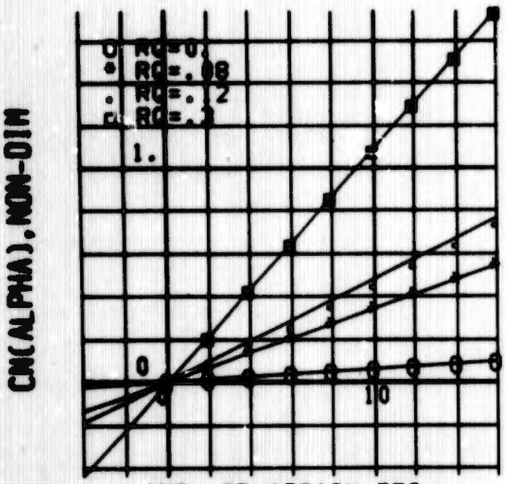

FIG 87 NORMAL FORCE COEFF.
VERSUS ALPHA, VECTOR=40

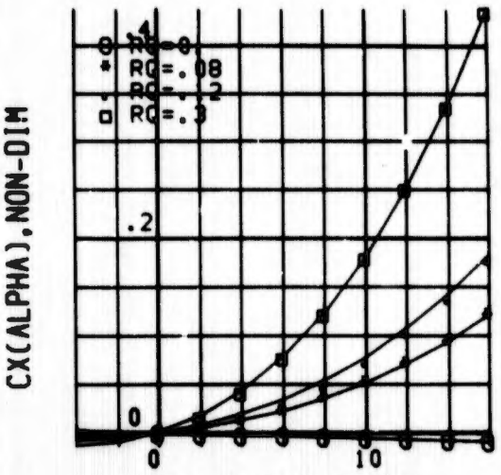

FIG 88 AXIAL FORCE COEFF.
VERSUS ALPHA, VECTOR=50

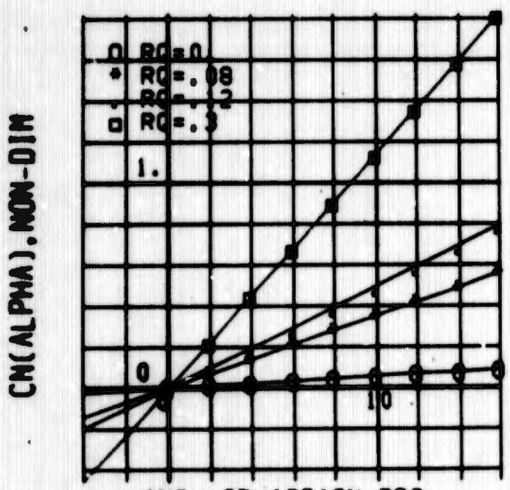

FIG 89 NORMAL FORCE COEFF.
VERSUS ALPHA, VECTOR=50

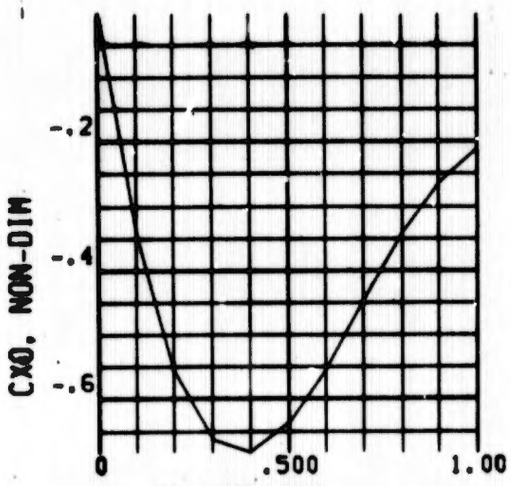

FIG 90 AXIAL FORCE COEFF.
ALPHA=VECTOR=STAGGER=0.

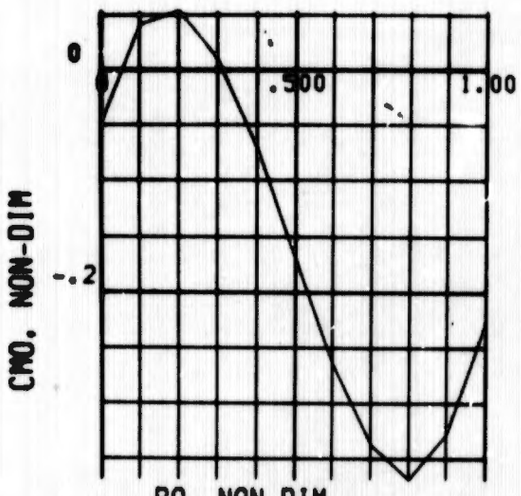

FIG 91 PITCHING MOMENT COEFF.
ALPHA=VECTOR=STAGGER=0.

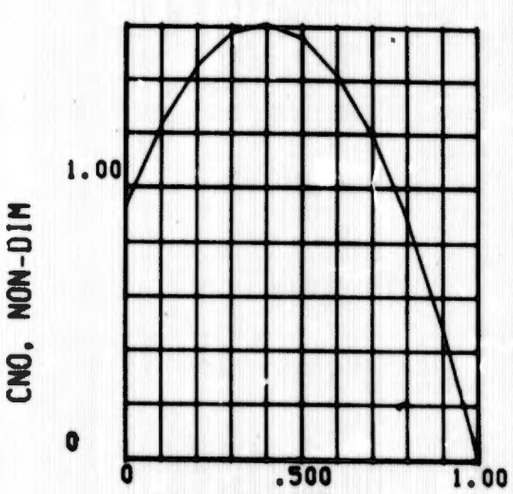

FIG 92 NORMAL FORCE COEFF.
ALPHA=VECTOR=STAGGER=0.

SECTION XIII

AERODYNAMIC CONSTANTS

$C_{L_{\alpha_t}}$	3.037	Rad^{-1}
$C_{L_{\delta_e}}$	1.318	Rad^{-1}
$C_{D_{\alpha_t}}$	.0150	Non-Dim.
$C_{D_{C_{L_t}^2}}$	0.1	Non-Dim.
$C_{y_{\delta_r}}$	-0.0344	Rad^{-1}
$C_{y_{\delta_a}}$	0.1117	Rad^{-1}
$C_{n_{\delta_r}}$	-.0699	Rad^{-1}
$C_{n_{\delta_{a(T_c^s=0)}}}$	-.00573	Rad^{-1}
$\frac{\partial C_{n_{\delta_a}}}{\partial T_c^s}$	-.0178	Rad^{-1}
$C_{L_{\delta_f}}$	.0143	Rad^{-1}
$C_{L_{\delta_s}}$	.0504	Rad^{-1}
C_{y_r}	.625	Rad^{-1}
C_{L_q}	3.44	Rad^{-1}
C_{L_p}	-.31	Rad^{-1}

C_{ℓ_r}	.15	Rad^{-1}
C_{m_β}	-.356	Rad^{-1}
C_{m_q}	-6.9	Rad^{-1}
C_{n_r}	-0.4	Rad^{-1}
C_{n_p}	-.02	Rad^{-1}
$C_{m_{\dot{\alpha}}}$	-2.296	Rad^{-1}
$C_{L_{\dot{\alpha}}}$	1.148	Rad^{-1}
$\delta Y/\delta v$	-31.8	Lb/Ft./Sec.
$C_D S_W$	317.	$Ft.^2$
$\partial Y/\partial r_{NF}$	-61.328	Lb./Ft./Sec.
$\partial N/\partial \lvert u \rvert$	3.0	Lb./Ft./Sec.
$\partial N/\partial \lvert v \rvert$	10.	Lb./Ft./Sec.
$\partial L/\partial \lvert v \rvert$	-134.	Lb./Ft./Sec.
$\partial L/\partial D$	-645.7	Ft-Lb/Rad/Sec
$\partial m/\partial u$	134.	Lb-Sec.
$\partial C^s_m/\partial Q^s$	35.5	$Ft.^2/Lb.$
$\partial n/\partial v$	47.	Lb-Sec
$\partial n/\partial r_F$	-645.7	Ft-Lb/Rad/Sec

$\partial n / \partial (x^2_{RF} r)$	-4.38	Lb/Ft-Rad/Sec
$\partial n / \partial \left[\frac{\rho V_t^2 v}{2}\right]$	560.	$Ft.^3$
K_{t_s}	1.	Non-Dim.
$K_{n_{RF}} = -1.154\ \beta_\delta + 1.467\ \beta_\delta^2 - .32\ \beta_\delta^3$		Non-Dim.
$K_{x_{RF}} = 2.99\ \beta_\delta - 2.718\ \beta_\delta^2 + .699\ \beta_\delta^3$		Non-Dim.
β_δ	$0 \leq \beta_\delta \leq 2.092$	Rad

Appendix II

FAILURE MODE TIME HISTORIES

APPENDIX II
FAILURE MODE TIME HISTORIES

This section contains time history plots of the aircraft failure modes discussed in the body of the text.

These time histories were generated by digital computer integration of the differential equations developed in Appendix I.

The computer program options allow time histories to be plotted, printed, punched and/or saved on an external storage device. The following time histories were plotted by use of the Stromberg-Carlson SC4020 CRT plotter but the computer program is not restricted to this specific machine.

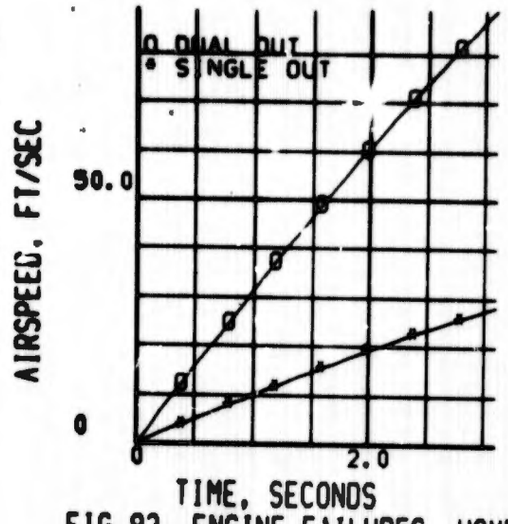

FIG 93 ENGINE FAILURES, HOVER AIRPLANE AIRSPEED

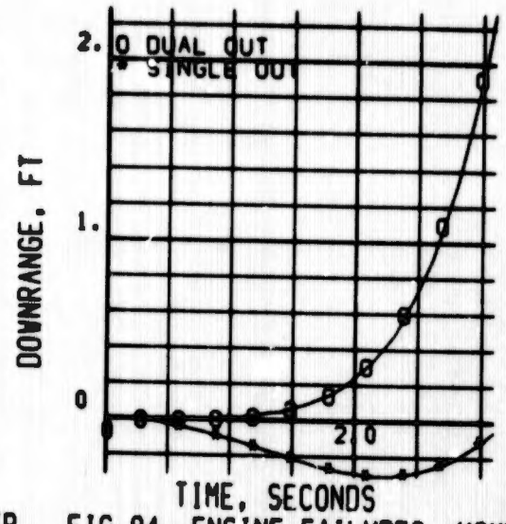

FIG 94 ENGINE FAILURES, HOVER AIRPLANE DOWNRANGE DISTANCE

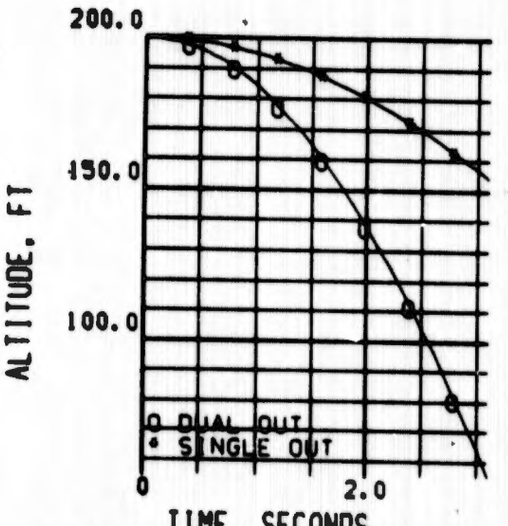

FIG 95 ENGINE FAILURES, HOVER AIRPLANE ALTITUDE

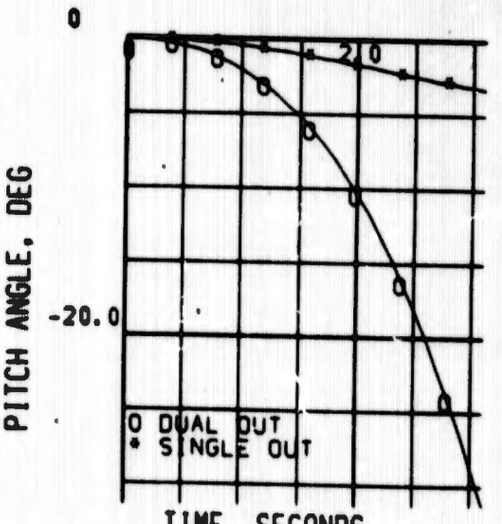

FIG 96 ENGINE FAILURES, HOVER AIRPLANE PITCH ANGLE

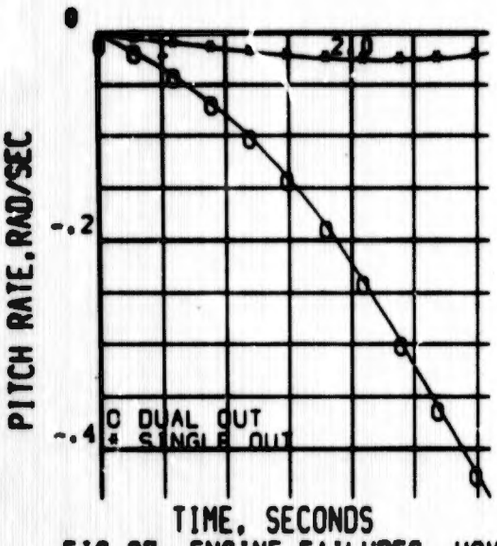

FIG 97 ENGINE FAILURES, HOVER AIRPLANE PITCH RATE

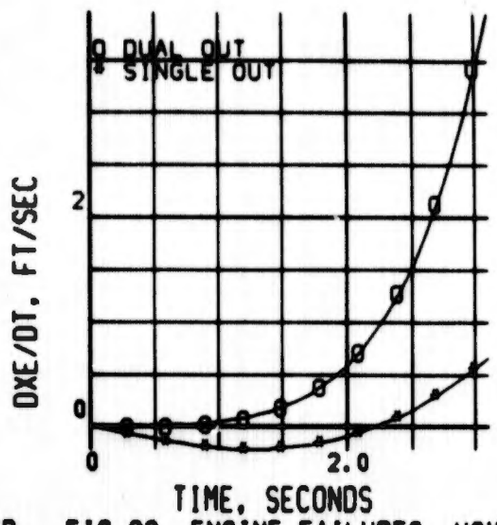

FIG 98 ENGINE FAILURES, HOVER AIRPLANE DOWNRANGE SPEED

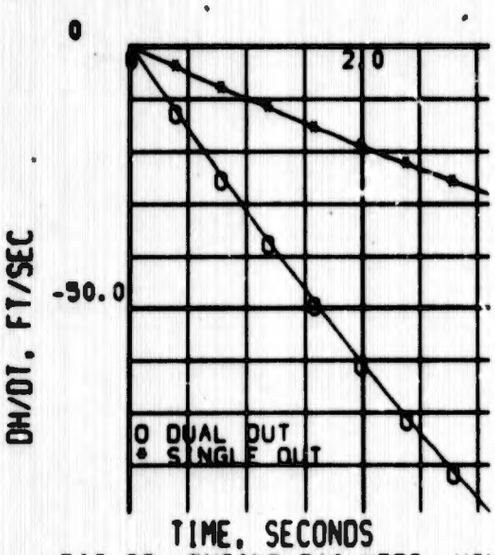

FIG 99 ENGINE FAILURES, HOVER AIRPLANE CLIMB RATE

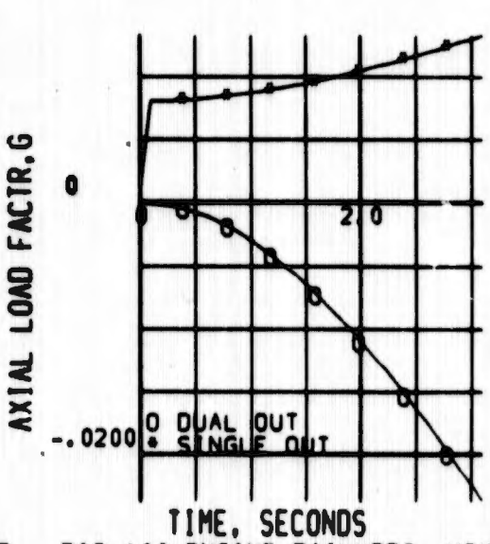

FIG 100 ENGINE FAILURES, HOVER AIRPLANE AXIAL LOAD FACTOR

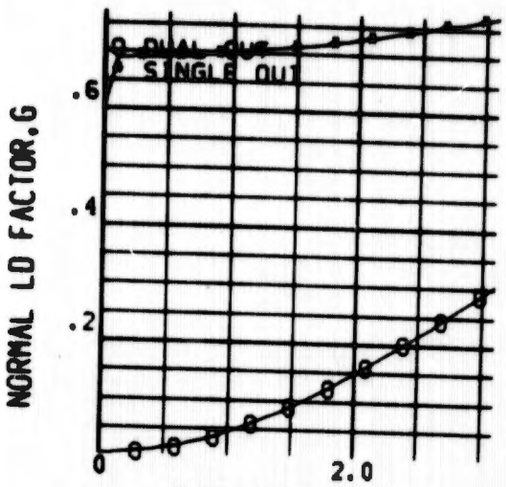

FIG 101 ENGINE FAILURES, HOVER
AIRPLANE NORMAL LOAD FACTOR

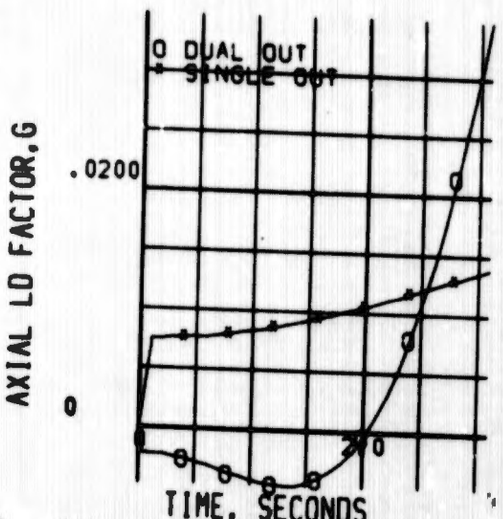

FIG 102 ENGINE FAILURES, HOVER
COCKPIT AXIAL LOAD FACTOR

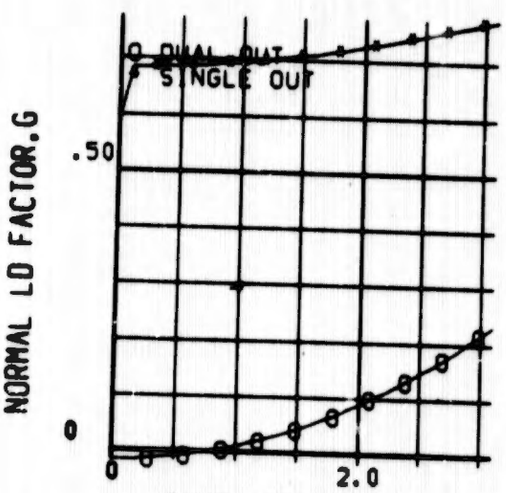

FIG 103 ENGINE FAILURES, HOVER
.COCKPIT NORMAL LOAD FACTOR

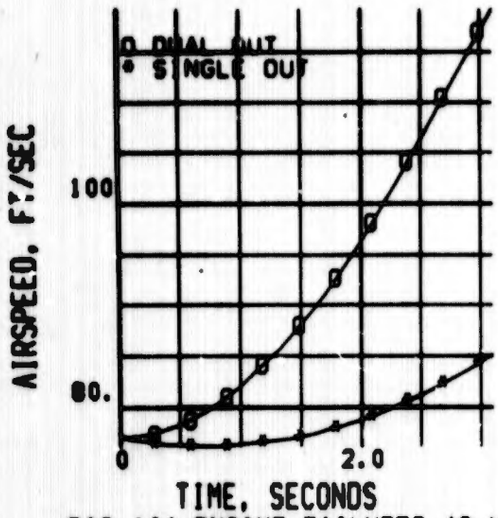

FIG 104 ENGINE FAILURES, 46 KT AIRPLANE AIRSPEED

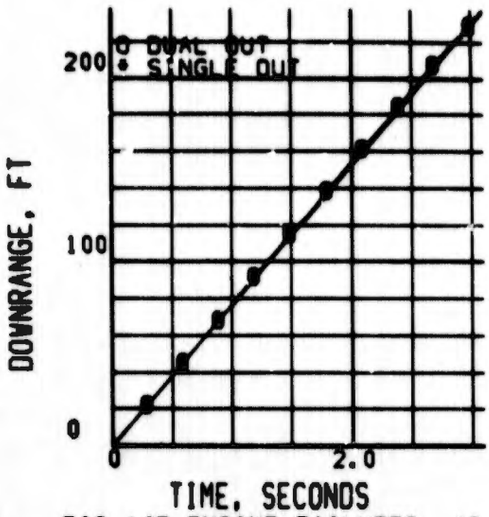

FIG 105 ENGINE FAILURES, 46 KT AIRPLANE DOWNRANGE DISTANCE

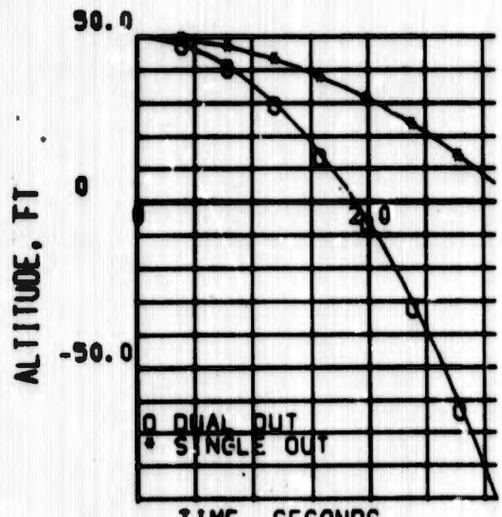

FIG 106 ENGINE FAILURES, 46 KT AIRPLANE ALTITUDE

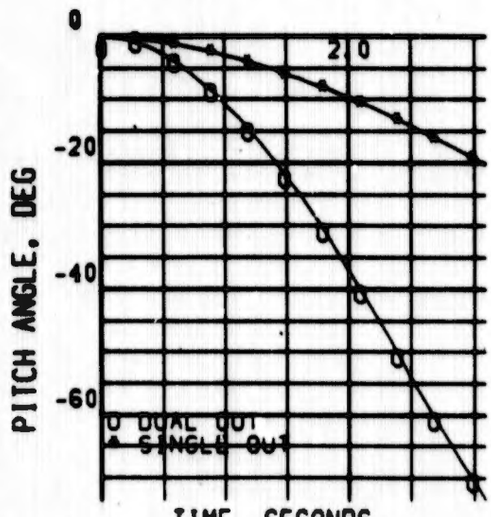

FIG 107 ENGINE FAILURES, 46 KT AIRPLANE PITCH ANGLE

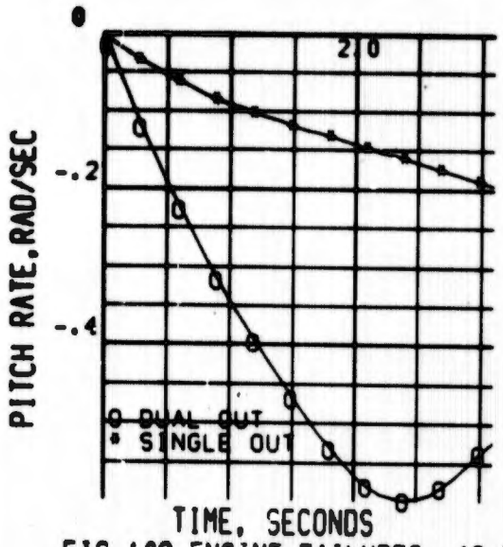

FIG 108 ENGINE FAILURES, 46 KT AIRPLANE PITCH RATE

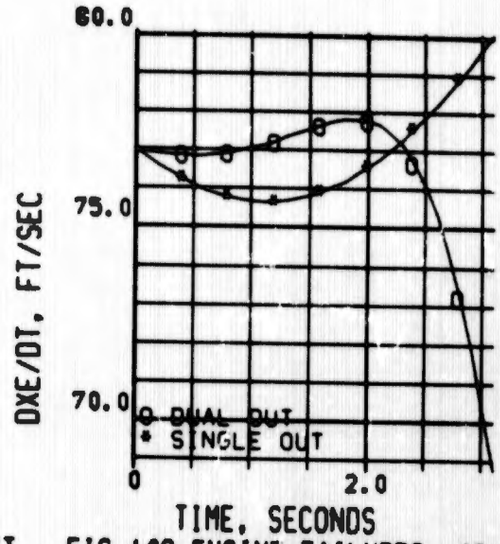

FIG 109 ENGINE FAILURES, 46 KT AIRPLANE DOWNRANGE SPEED

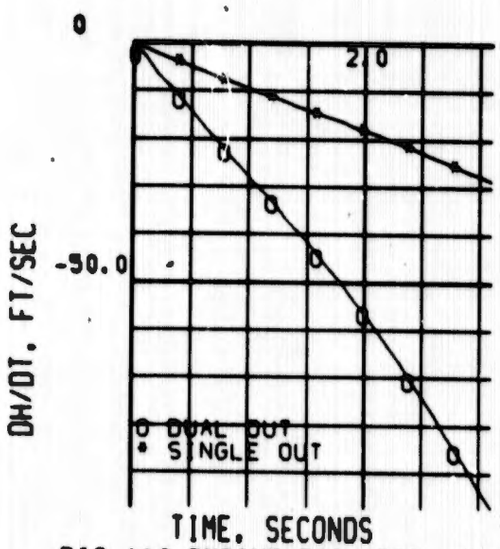

FIG 110 ENGINE FAILURES, 46 KT AIRPLANE CLIMB RATE

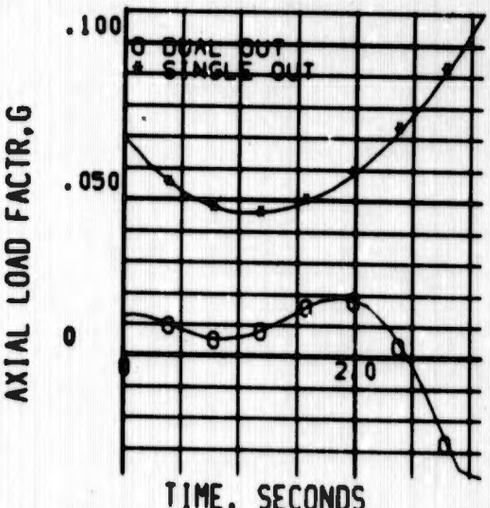

FIG 111 ENGINE FAILURES, 46 KT AIRPLANE AXIAL LOAD FACTOR

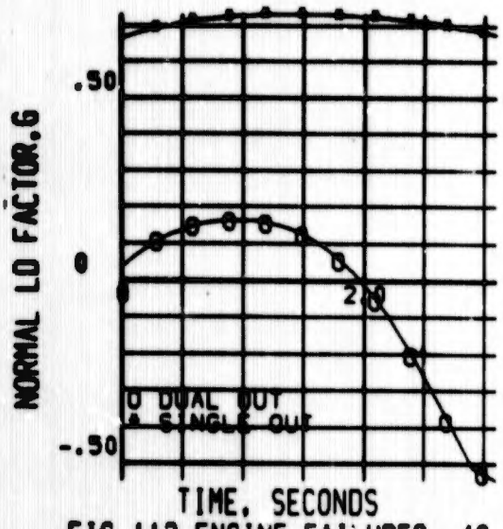

FIG 112 ENGINE FAILURES, 46 KT
AIRPLANE NORMAL LOAD FACTOR

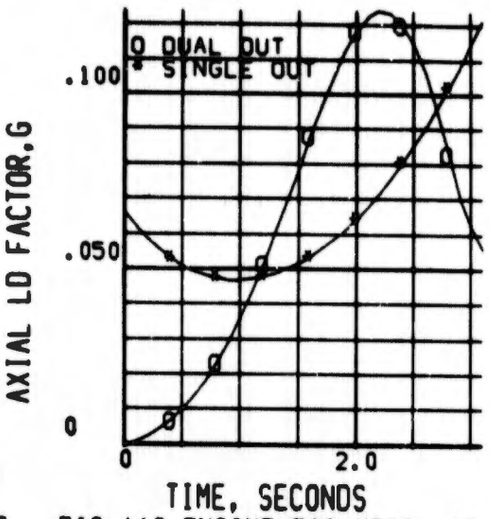

FIG 113 ENGINE FAILURES, 46 KT
COCKPIT AXIAL LOAD FACTOR

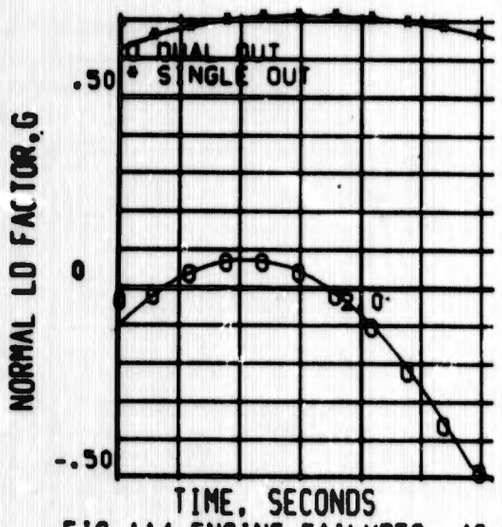

FIG 114 ENGINE FAILURES, 46 KT
COCKPIT NORMAL LOAD FACTOR

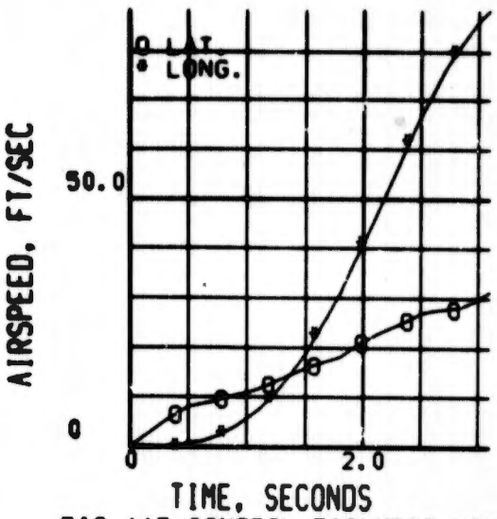

FIG 115 CONTROL FAILURES, HOVER AIRPLANE AIRSPEED

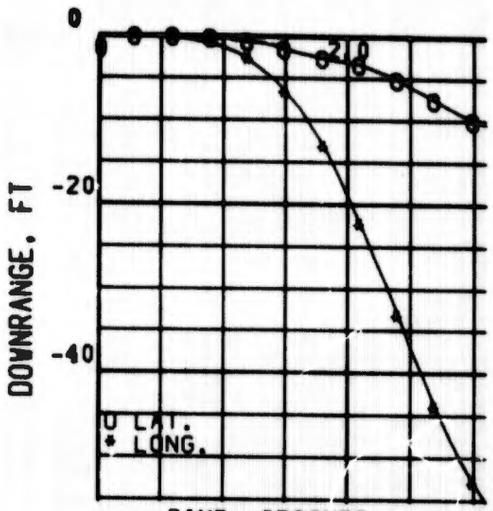

FIG 116 CONTROL FAILURES, HOVER AIRPLANE DOWNRANGE DISTANCE

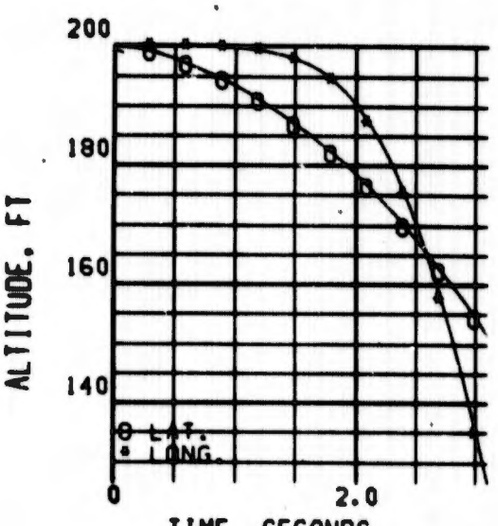

FIG 117 CONTROL FAILURES, HOVER AIRPLANE ALTITUDE

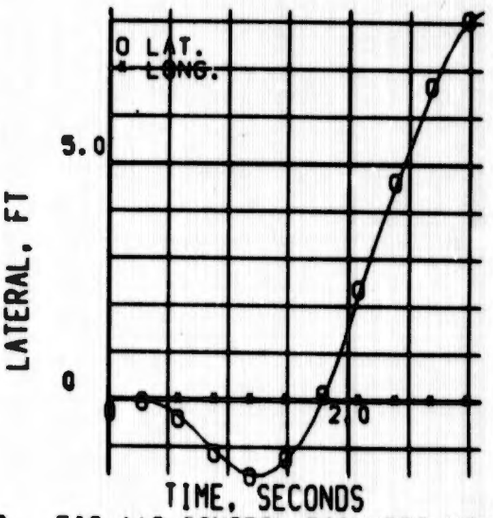

FIG 118 CONTROL FAILURES, HOVER AIRPLANE LATERAL DISTANCE

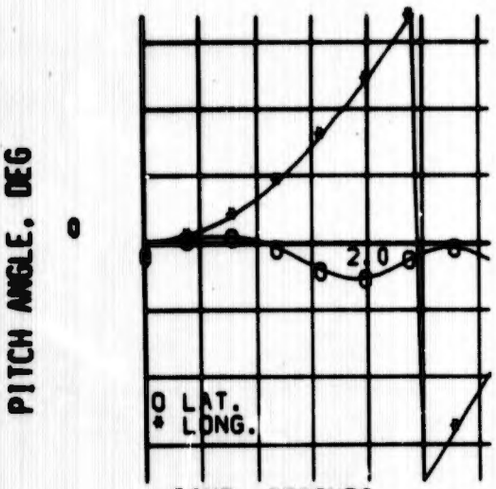

FIG 119 CONTROL FAILURES, HOVER AIRPLANE PITCH ANGLE

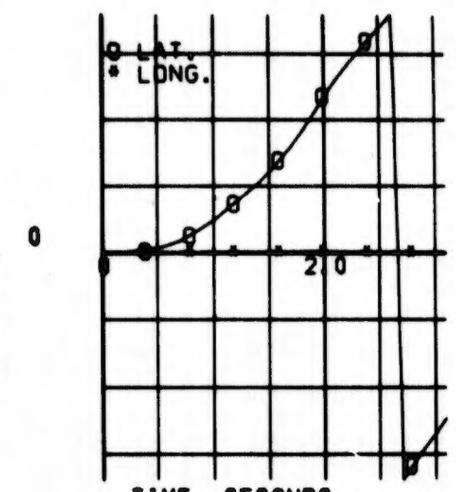

FIG 120 CONTROL FAILURES, HOVER AIRPLANE YAW ANGLE

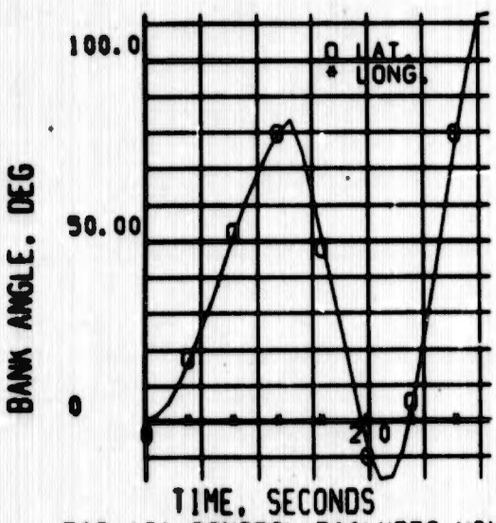

FIG 121 CONTROL FAILURES, HOVER AIRPLANE BANK ANGLE

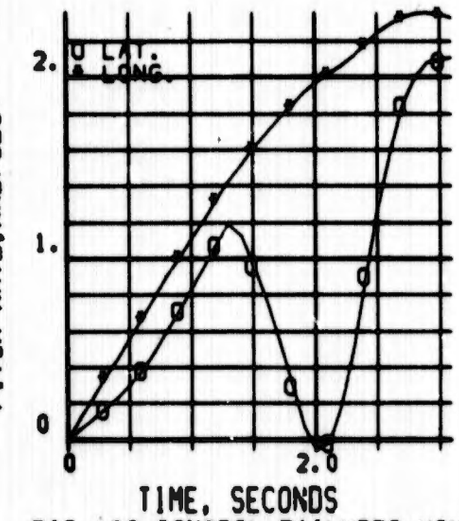

FIG 122 CONTROL FAILURES, HOVER AIRPLANE PITCH RATE

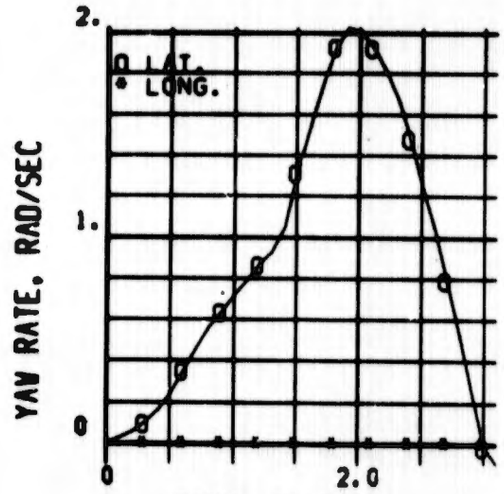

FIG 123 CONTROL FAILURES, HOVER AIRPLANE YAW RATE

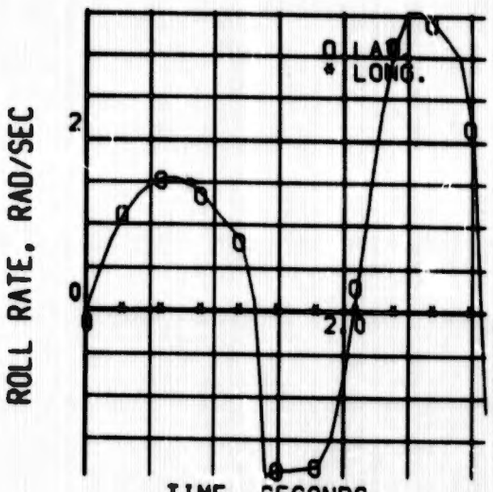

FIG 124 CONTROL FAILURES, HOVER AIRPLANE ROLL RATE

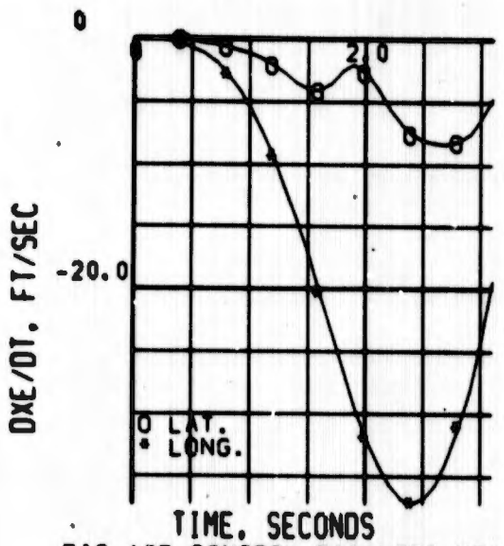

FIG 125 CONTROL FAILURES, HOVER AIRPLANE DOWNRANGE SPEED

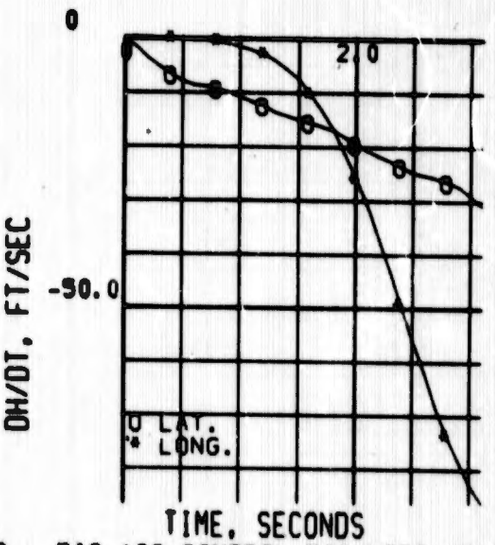

FIG 126 CONTROL FAILURES, HOVER AIRPLANE CLIMB RATE

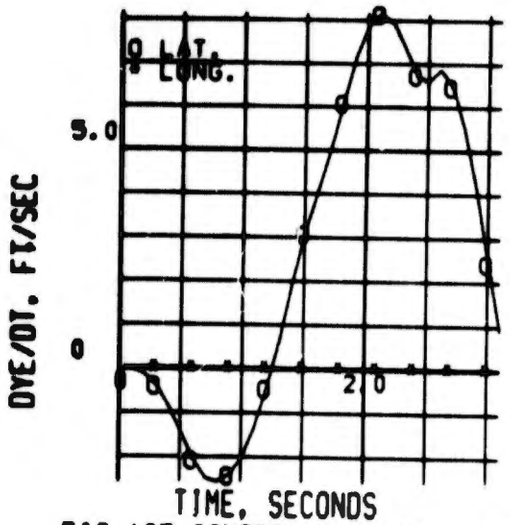

FIG 127 CONTROL FAILURES, HOVER AIRPLANE LATERAL SPEED

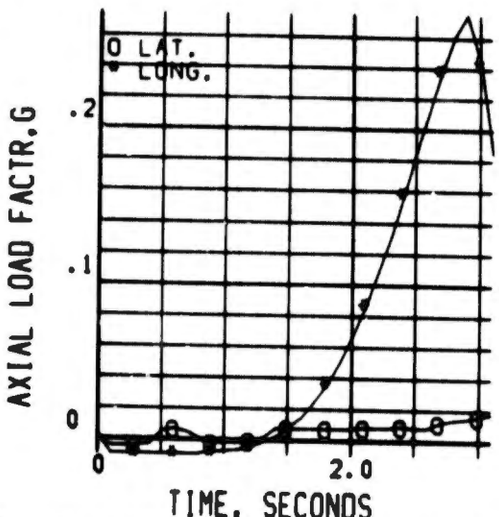

FIG 128 CONTROL FAILURES, HOVER AIRPLANE AXIAL LOAD FACTOR

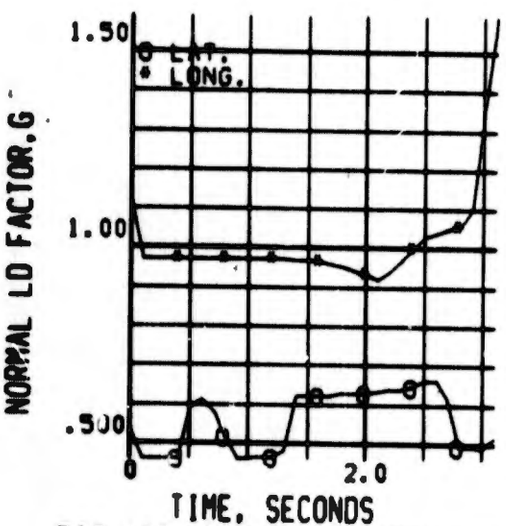

FIG 129 CONTROL FAILURES, HOVER AIRPLANE NORMAL LOAD FACTOR

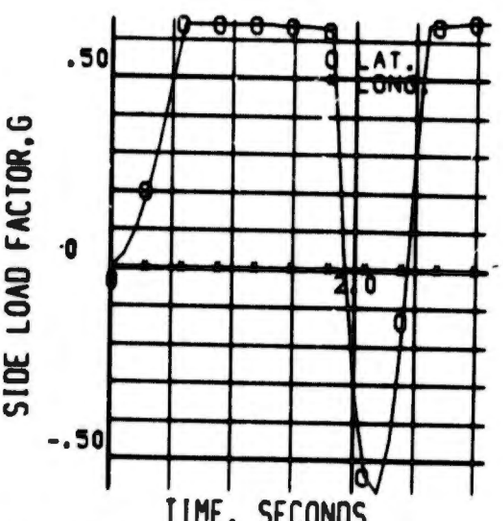

FIG 130 CONTROL FAILURES, HOVER AIRPLANE SIDE LOAD FACTOR

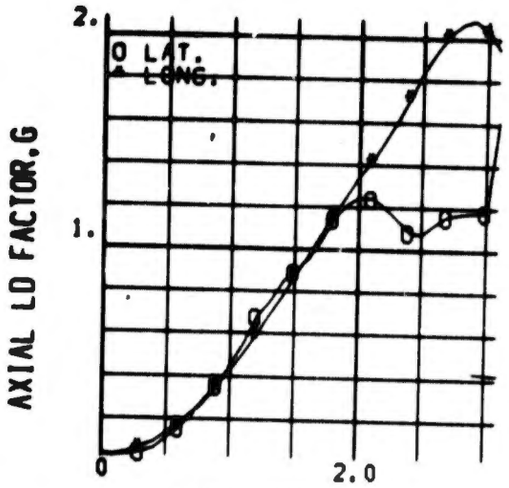

FIG 131 CONTROL FAILURES, HOVER
COCKPIT AXIAL LOAD FACTOR

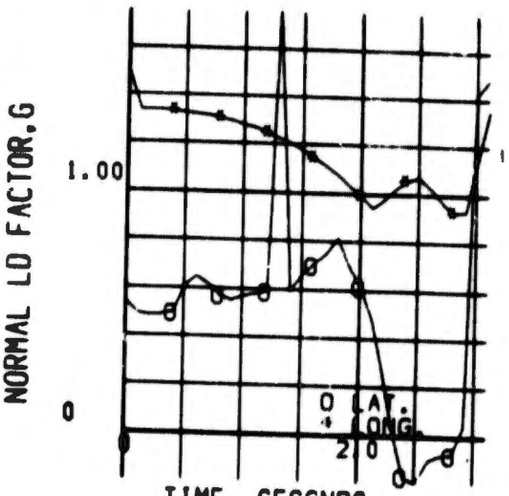

FIG 132 CONTROL FAILURES, HOVER
COCKPIT NORMAL LOAD FACTOR

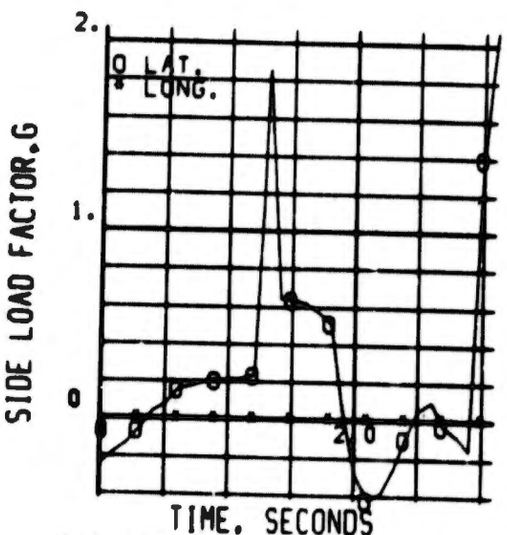

FIG 133 CONTROL FAILURES, HOVER
COCKPIT SIDE LOAD FACTOR

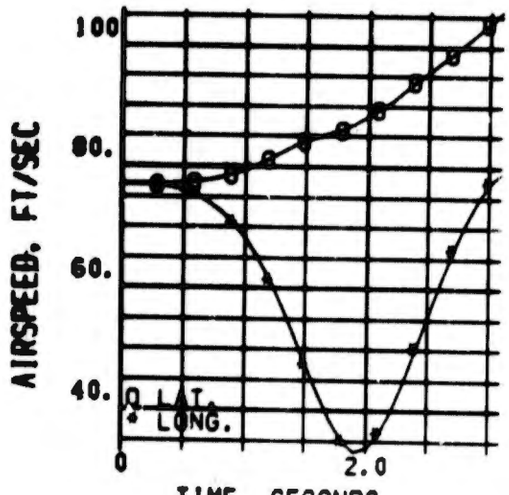

FIG 134 CONTROL FAILURES, 46 KT AIRPLANE AIRSPEED

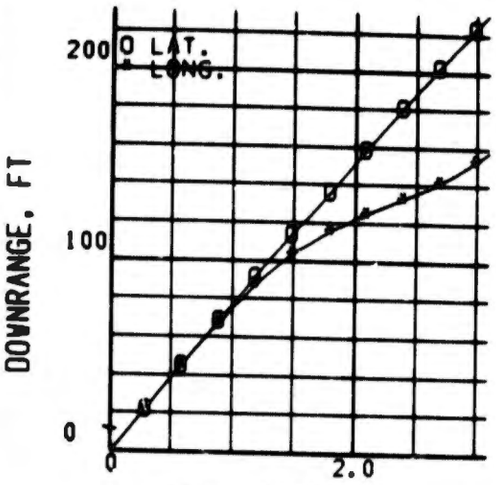

FIG 135 CONTROL FAILURES, 46 KT AIRPLANE DOWNRANGE DISTANCE

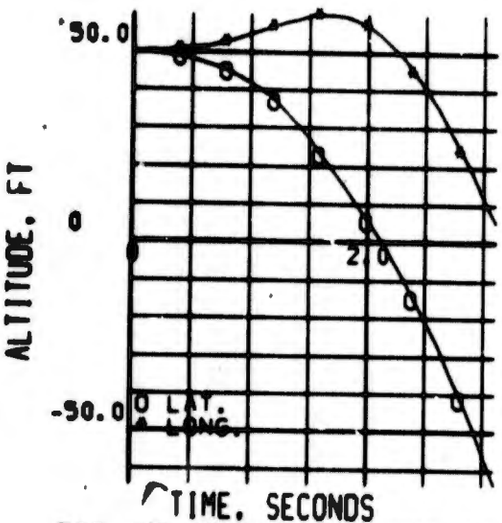

FIG 136 CONTROL FAILURES, 46 KT AIRPLANE ALTITUDE

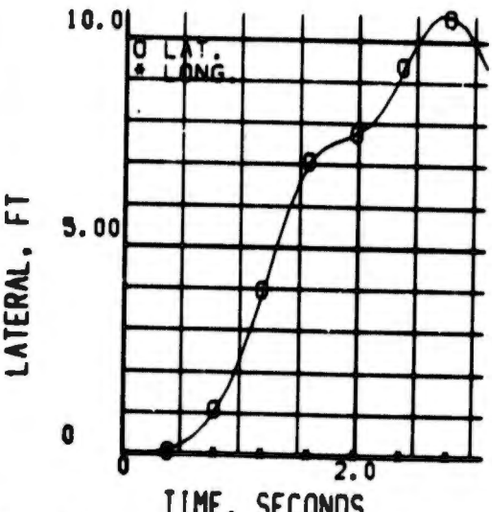

FIG 137 CONTROL FAILURES, 46 KT AIRPLANE LATERAL DISTANCE

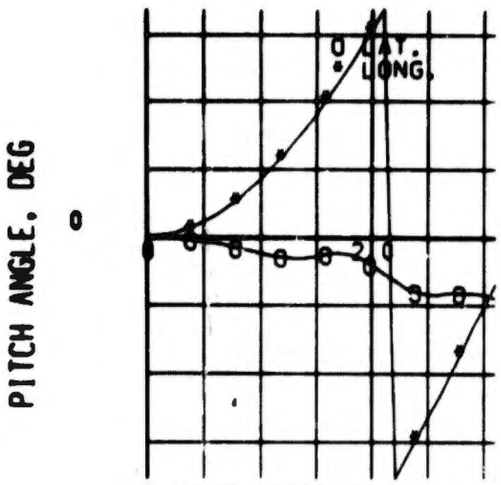

FIG 138 CONTROL FAILURES, 46 KT AIRPLANE PITCH ANGLE

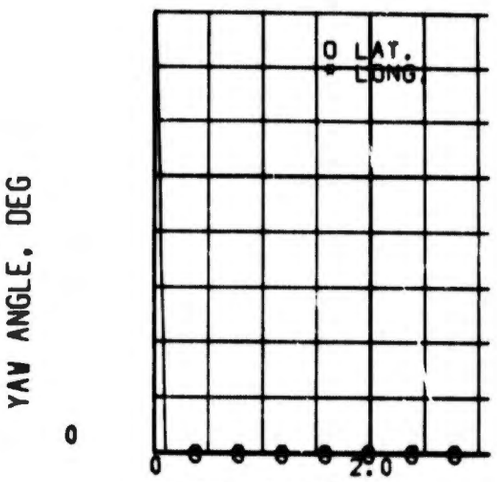

FIG 139 CONTROL FAILURES, 46 KT AIRPLANE YAW ANGLE

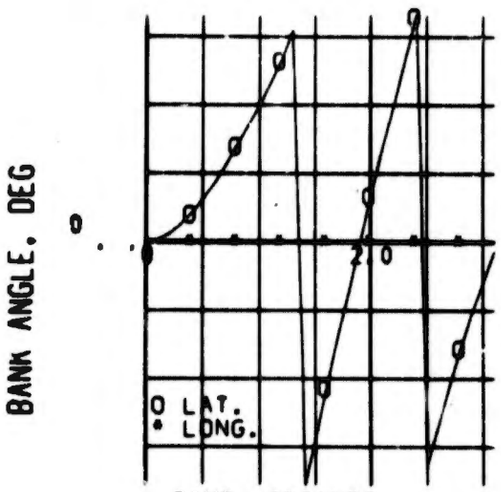

FIG 140 CONTROL FAILURES, 46 KT AIRPLANE BANK ANGLE

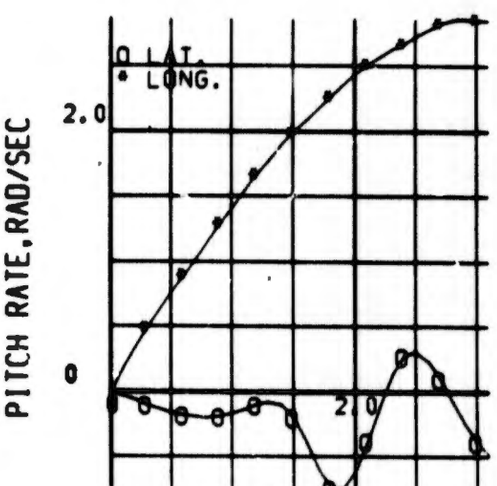

FIG 141 CONTROL FAILURES, 46 KT AIRPLANE PITCH RATE

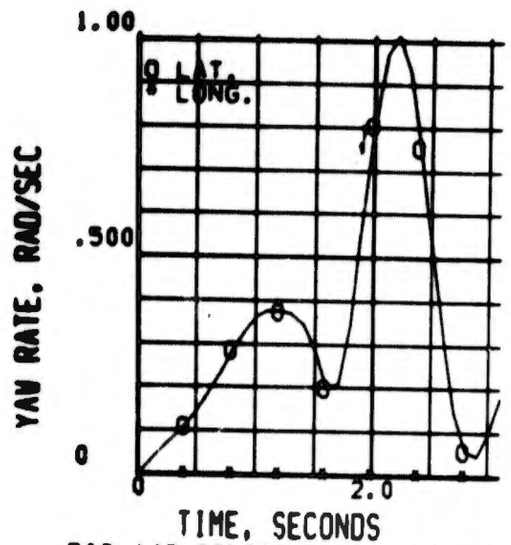

FIG 142 CONTROL FAILURES, 46 KT AIRPLANE YAW RATE

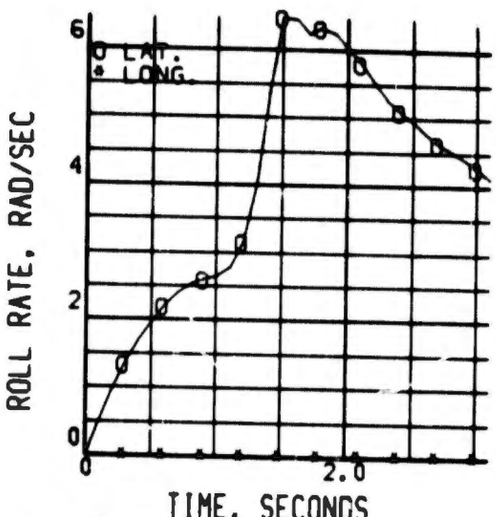

FIG 143 CONTROL FAILURES, 46 KT AIRPLANE ROLL RATE

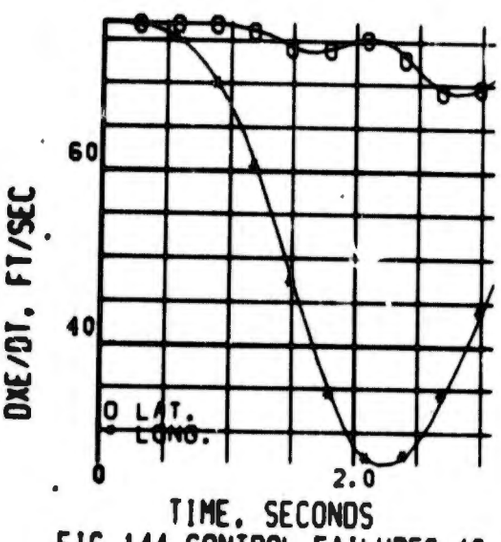

FIG 144 CONTROL FAILURES, 46 KT AIRPLANE DOWNRANGE SPEED

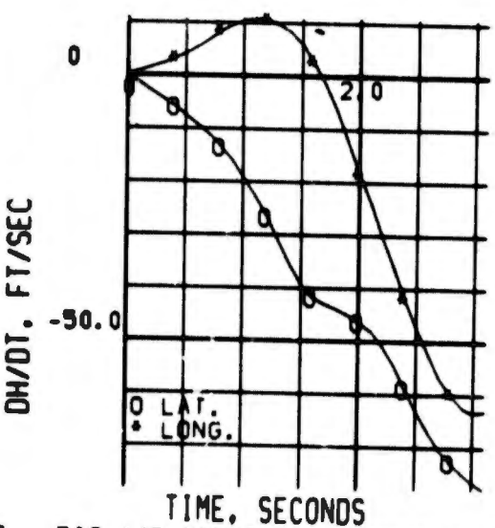

FIG 145 CONTROL FAILURES, 46 KT AIRPLANE CLIMB RATE

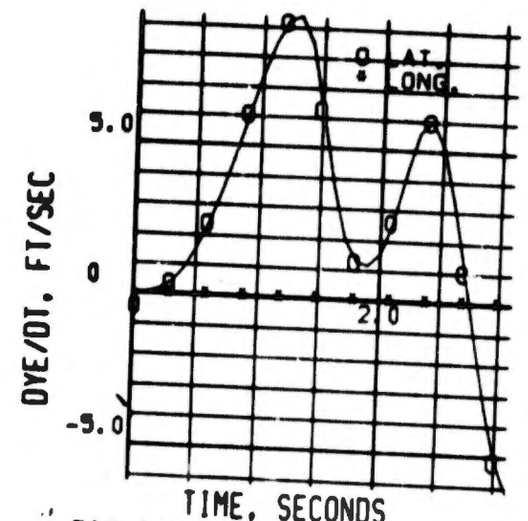

FIG 146 CONTROL FAILURES, 46 KT AIRPLANE LATERAL SPEED

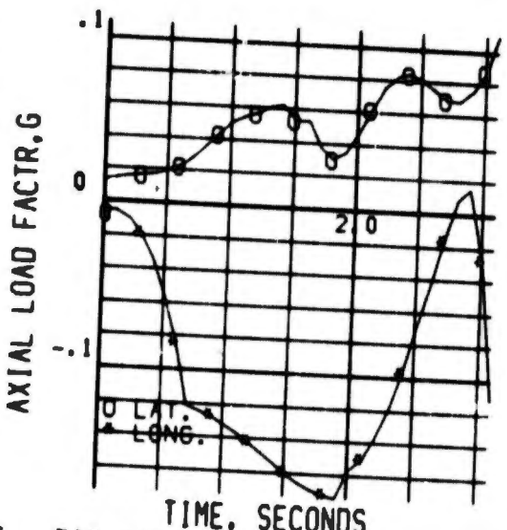

FIG 147 CONTROL FAILURES, 46 KT AIRPLANE AXIAL LOAD FACTOR

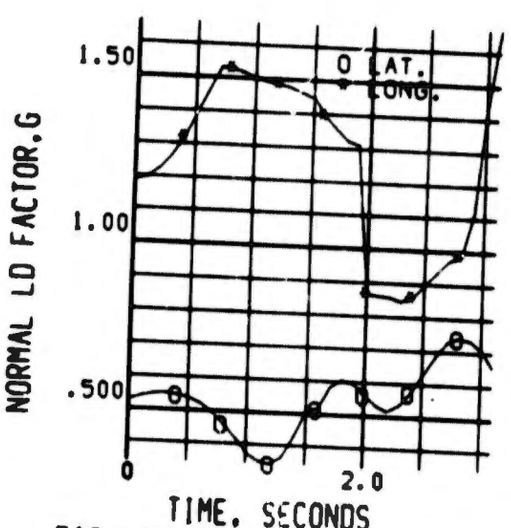

FIG 148 CONTROL FAILURES, 46 KT AIRPLANE NORMAL LOAD FACTOR

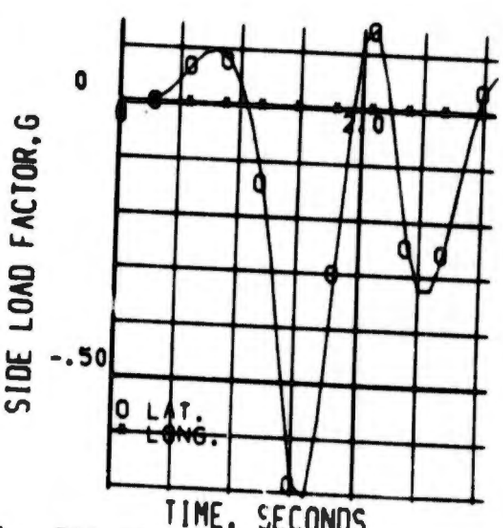

FIG 149 CONTROL FAILURES, 46 KT AIRPLANE SIDE LOAD FACTOR

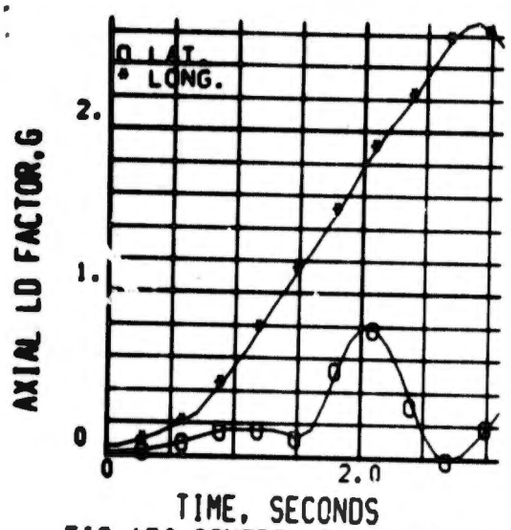

FIG 150 CONTROL FAILURES, 46 KT
COCKPIT AXIAL LOAD FACTOR

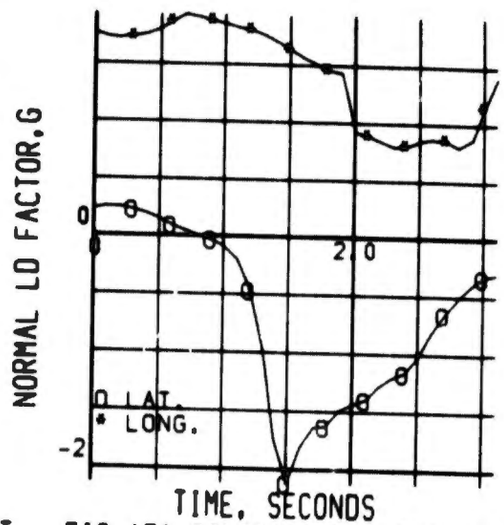

FIG 151 CONTROL FAILURES, 46 KT
COCKPIT NORMAL LOAD FACTOR

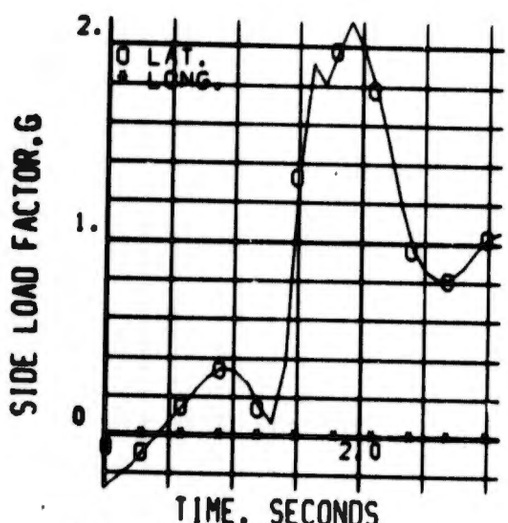

FIG 152 CONTROL FAILURES, 46 KT
COCKPIT SIDE LOAD FACTOR

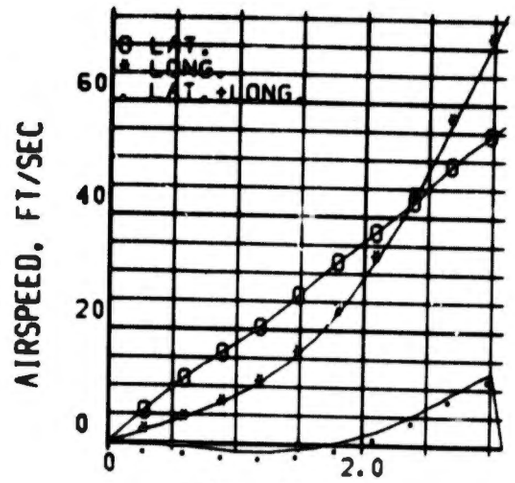

FIG 153 ENGINE.CONTROL FAILURE HOVER, AIRPLANE AIRSPEED

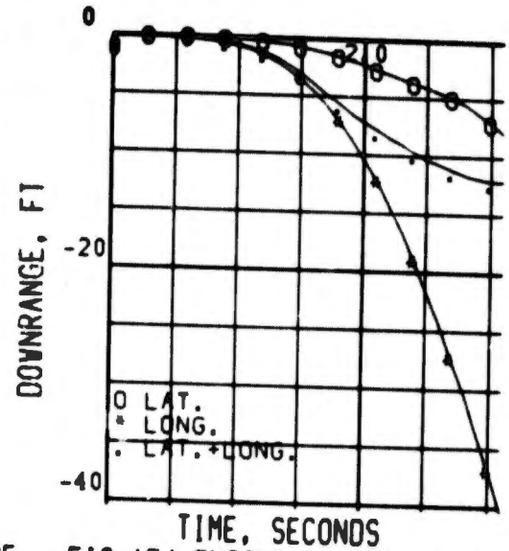

FIG 154 ENGINE.CONTROL FAILURE HOVER, AIRPLANE DOWNRANGE DIST

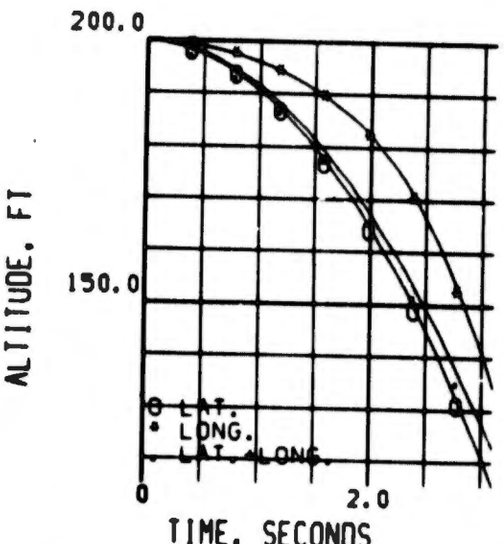

FIG 155 ENGINE.CONTROL FAILURE HOVER, AIRPLANE ALTITUDE

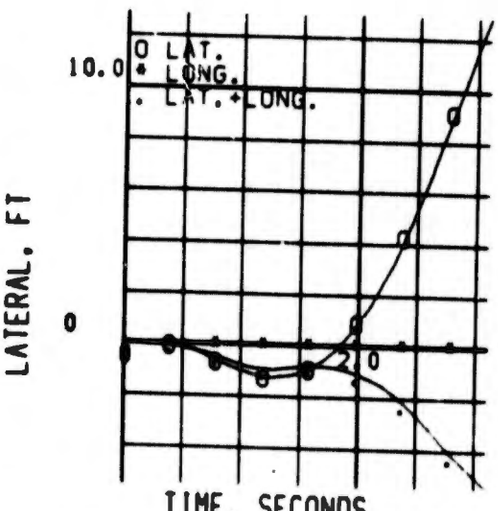

FIG 156 ENGINE.CONTROL FAILURE HOVER, AIRPLANE LATERAL DIST

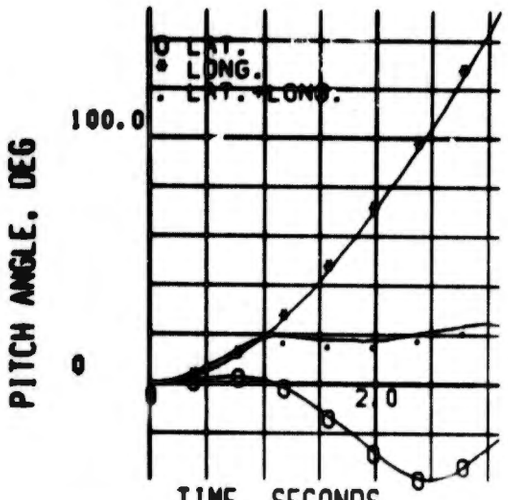

FIG 157 ENGINE,CONTROL FAILURE HOVER, AIRPLANE PITCH ANGLE

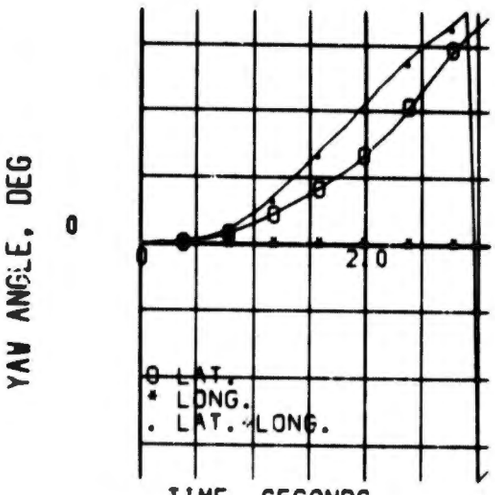

FIG 158 ENGINE,CONTROL FAILURE HOVER, AIRPLANE YAW ANGLE

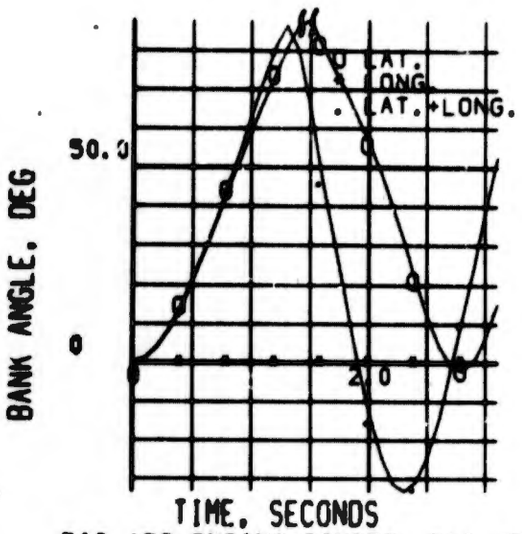

FIG 159 ENGINE,CONTROL FAILURE HOVER, AIRPLANE BANK ANGLE

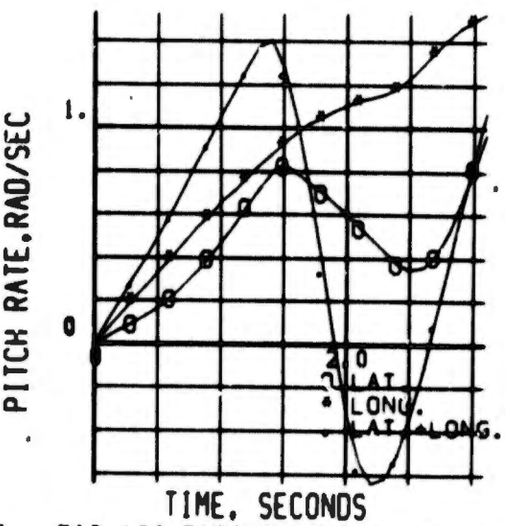

FIG 160 ENGINE,CONTROL FAILURE HOVER, AIRPLANE PITCH RATE

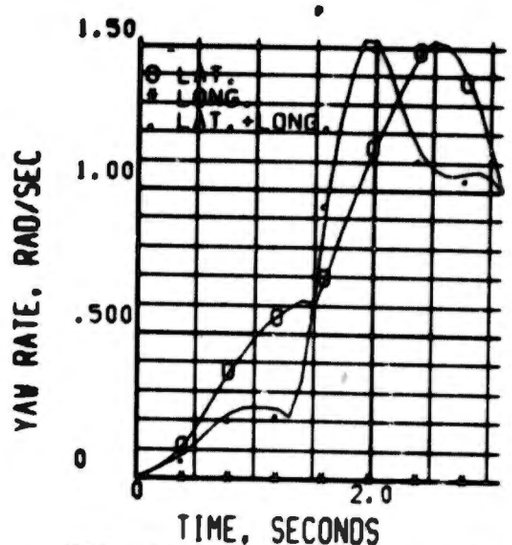

FIG 161 ENGINE.CONTROL FAILURE HOVER AIRPLANE YAW RATE

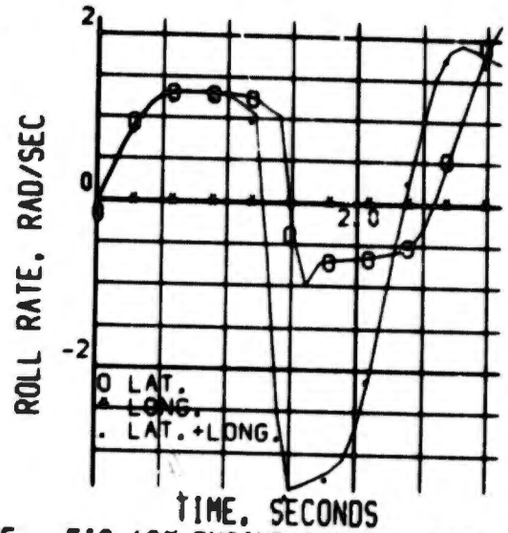

FIG 162 ENGINE.CONTROL FAILURE HOVER, AIRPLANE ROLL RATE

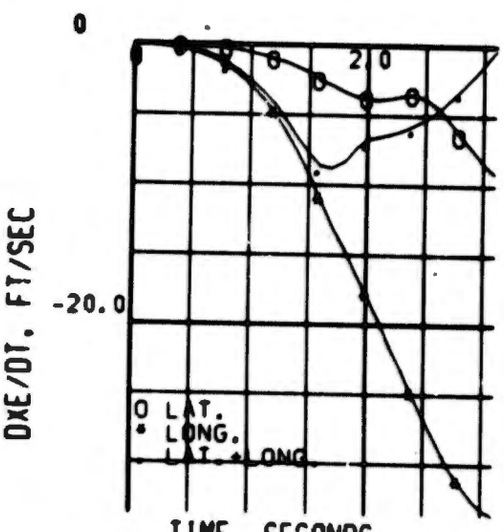

FIG 163 ENGINE.CONTROL FAILURE HOVER, AIRPLANE DOWNRNGE SPEED

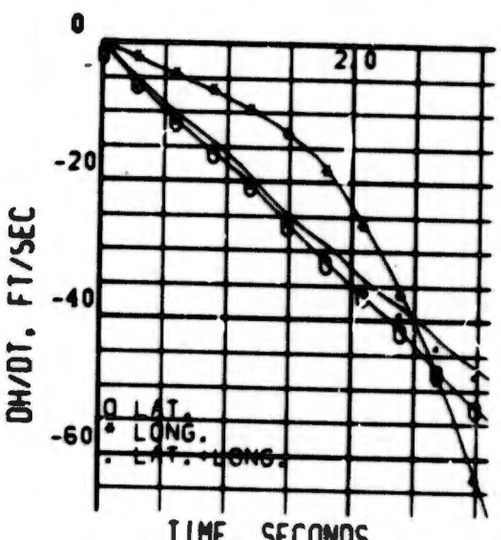

FIG 164 ENGINE.CONTROL FAILURE HOVER, AIRPLANE CLIMB RATE

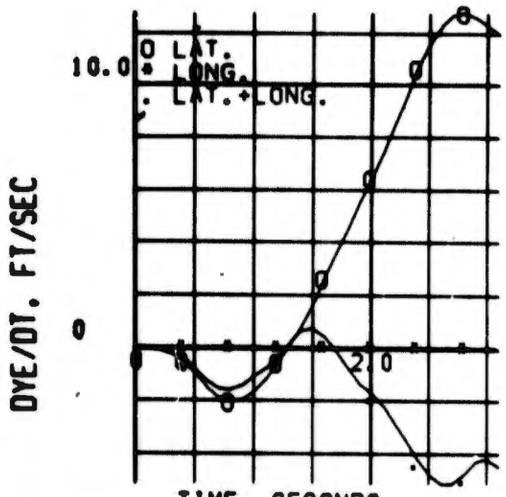

FIG 165 ENGINE,CONTROL FAILURE HOVER, AIRPLANE LATERAL SPEED

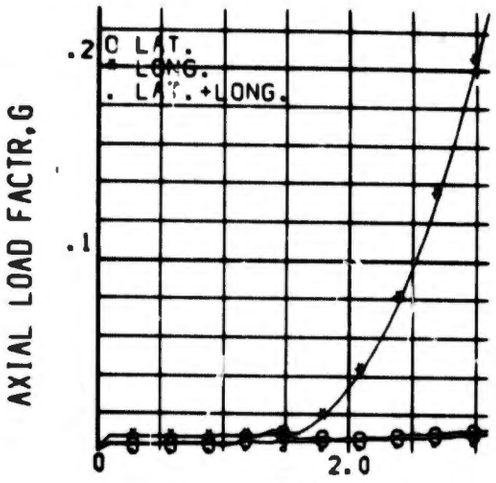

FIG 166 ENGINE,CONTROL FAILURE HOVER, AIRPLANE LOAD FACTOR

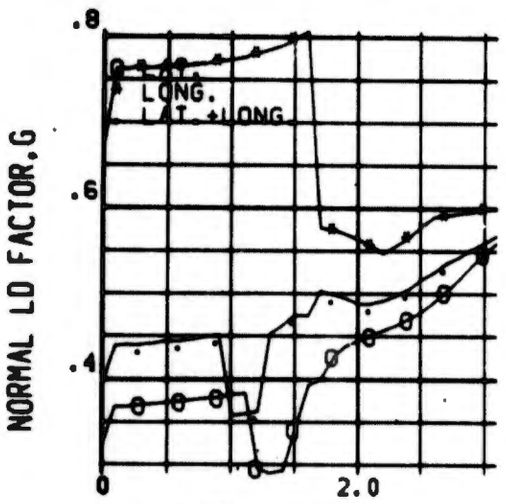

FIG 167 ENGINE,CONTROL FAILURE HOVER, AIRPLANE LOAD FACTOR

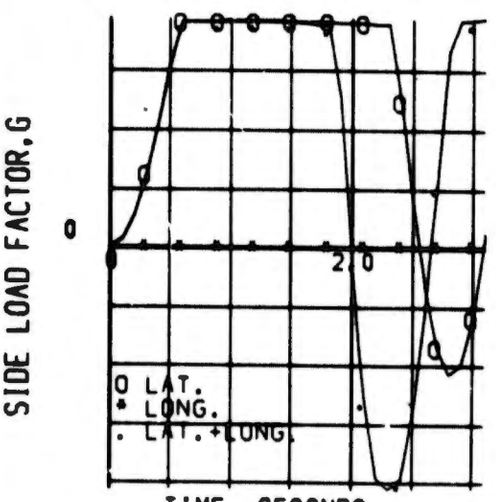

FIG 168 ENGINE,CONTROL FAILURE HOVER, AIRPLANE LOAD FACTOR

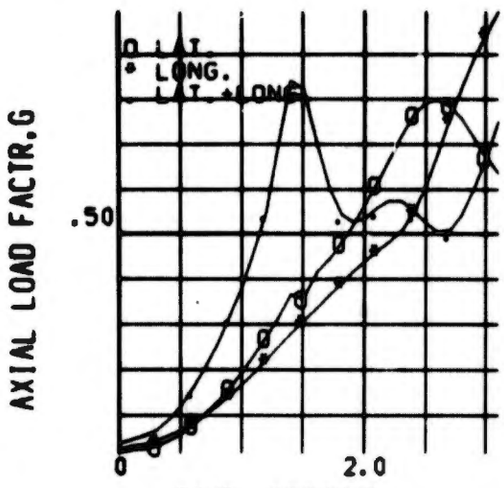

FIG 169 ENGINE.CONTROL FAILURE HOVER, COCKPIT LOAD FACTOR

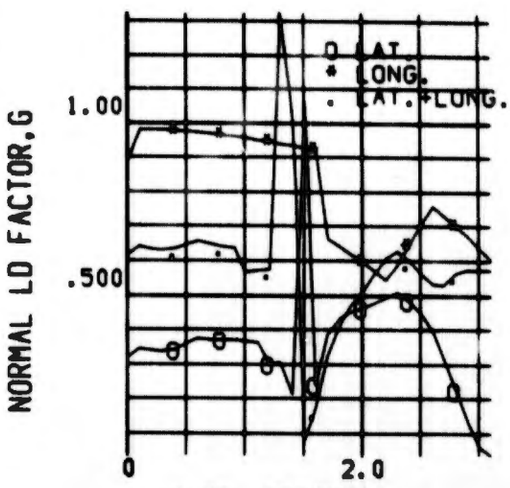

FIG 170 ENGINE.CONTROL FAILURE HOVER, COCKPIT LOAD FACTOR

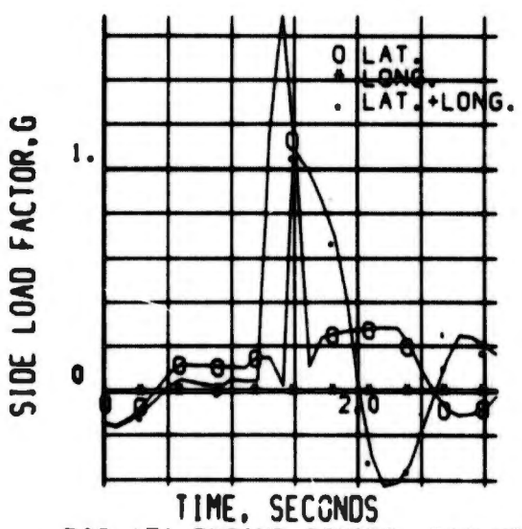

FIG 171 ENGINE.CONTROL FAILURE HOVER, COCKPIT LOAD FACTOR

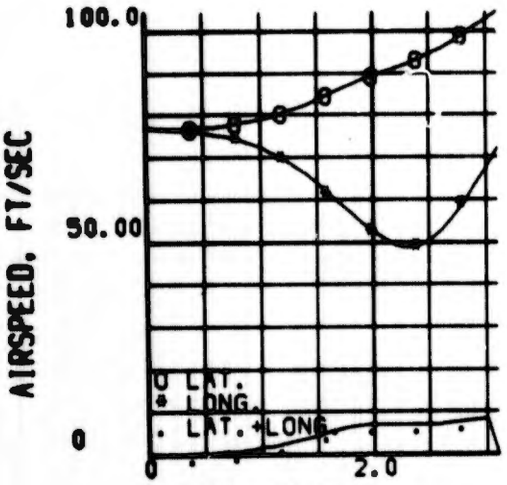

FIG 172 ENGINE,CONTROL FAILURE
46 KT, AIRPLANE AIRSPEED

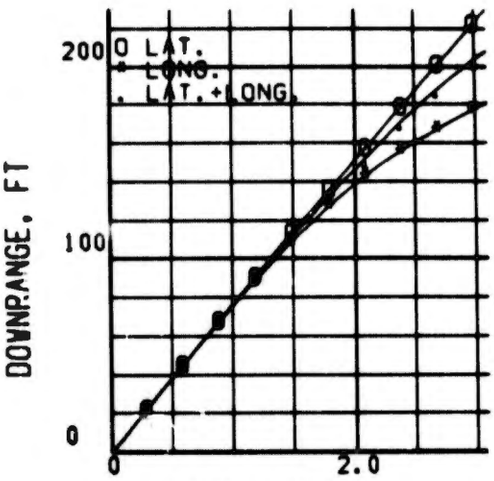

FIG 173 ENGINE,CONTROL FAILURE
46 KT, AIRPLANE DOWNRANGE DIST

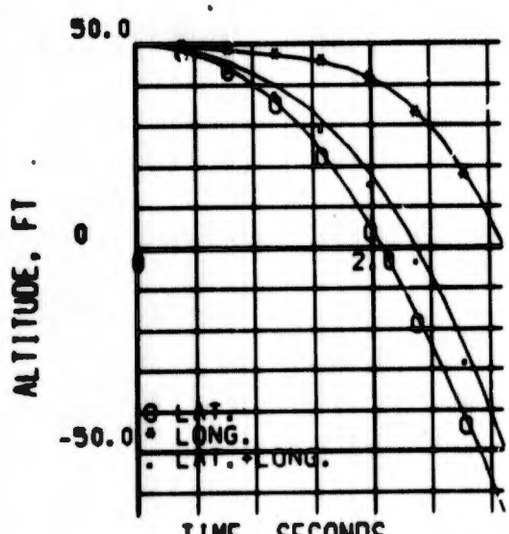

FIG 174 ENGINE,CONTROL FAILURE
46 KT, AIRPLANE ALTITUDE

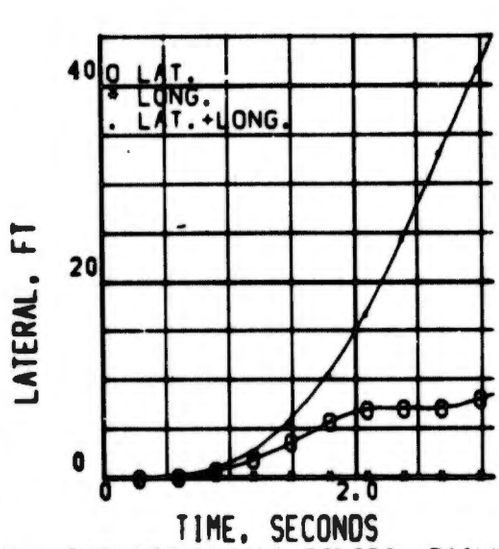

FIG 175 ENGINE,CONTROL FAILURE
46 KT, AIRPLANE LATERAL DIST

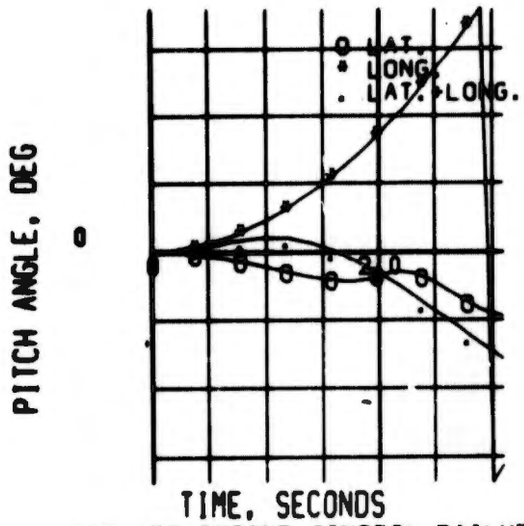

FIG 176 ENGINE, CONTROL FAILURE
46 KT, AIRPLANE PITCH ANGLE

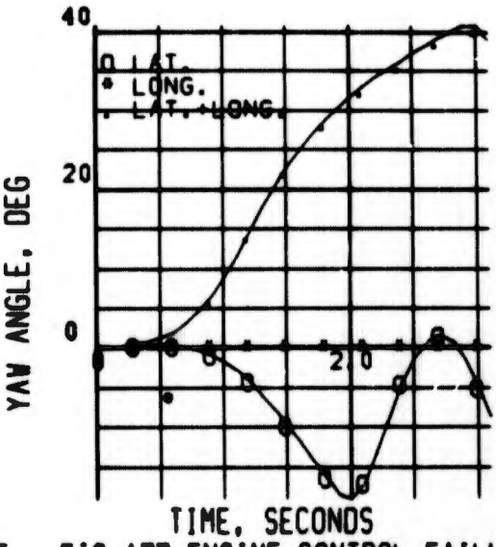

FIG 177 ENGINE, CONTROL FAILURE
46 KT, AIRPLANE YAW ANGLE

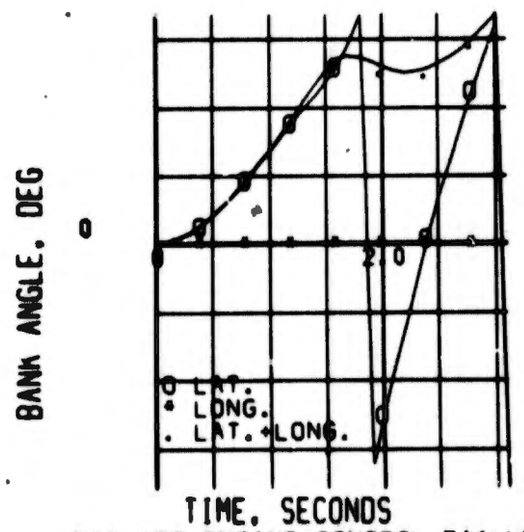

FIG 178 ENGINE, CONTROL FAILURE
46 KT, AIRPLANE BANK ANGLE

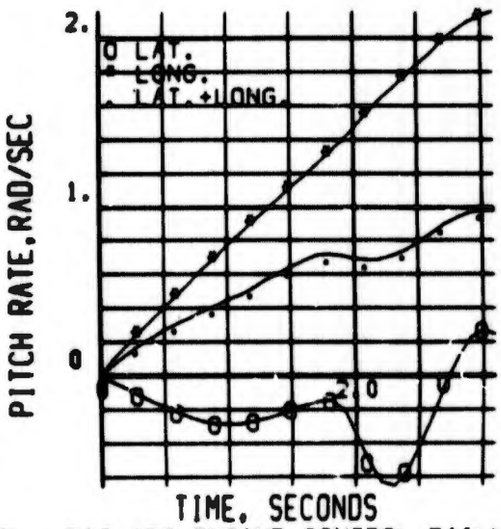

FIG 179 ENGINE, CONTROL FAILURE
46 KT, AIRPLANE PITCH RATE

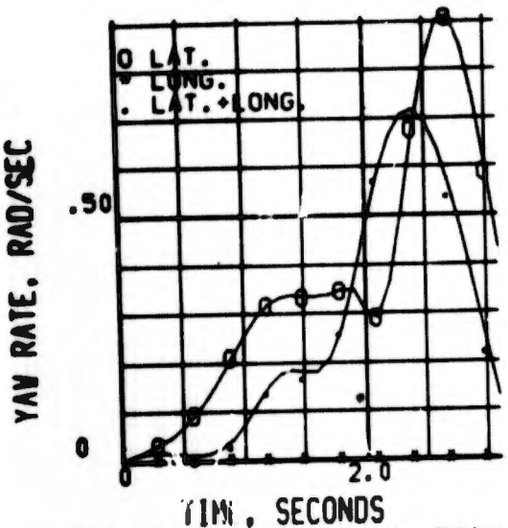

FIG 180 ENGINE.CONTROL FAILURE
46 KT.AIRPLANE YAW RATE

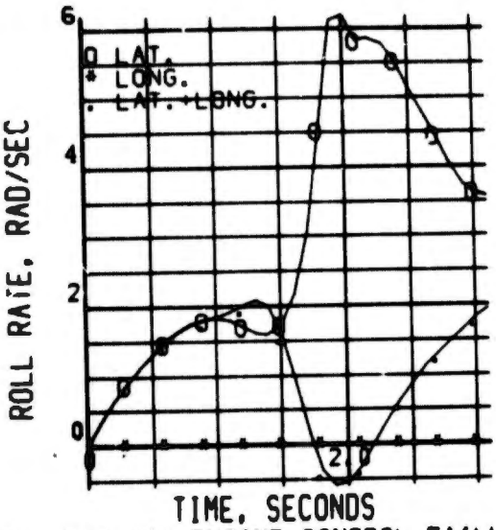

FIG 181 ENGINE.CONTROL FAILURE
46 KT, AIRPLANE ROLL RATE

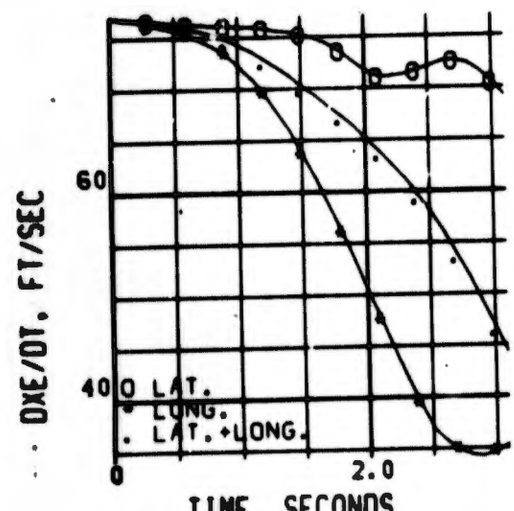

FIG 182 ENGINE.CONTROL FAILURE
46 KT, AIRPLANE DOWNRNGE SPEED

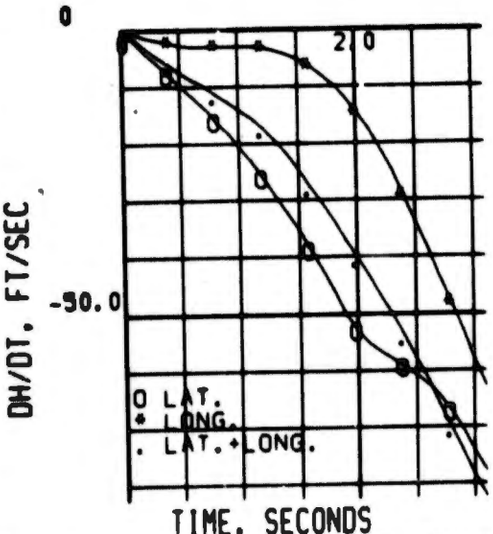

FIG 183 ENGINE.CONTROL FAILURE
46 KT, AIRPLANE CLIMB RATE

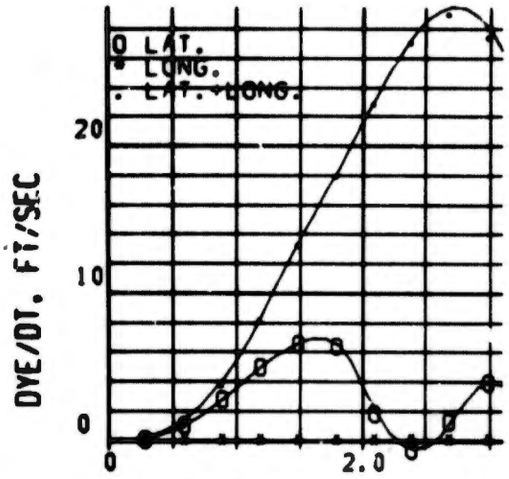

FIG 184 ENGINE,CONTROL FAILURE
46 KT, AIRPLANE LATERAL SPEED

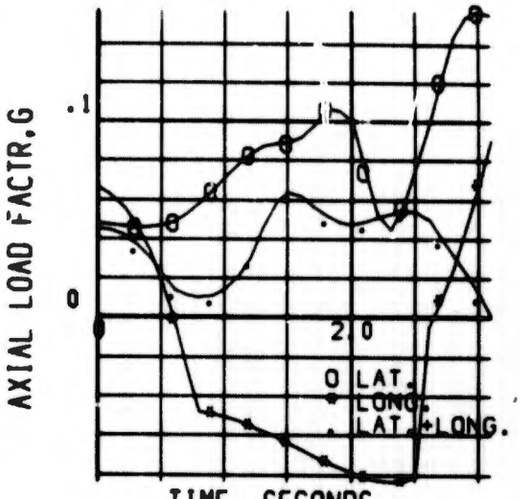

FIG 185 ENGINE,CONTROL FAILURE
46 KT, AIRPLANE LOAD FACTOR

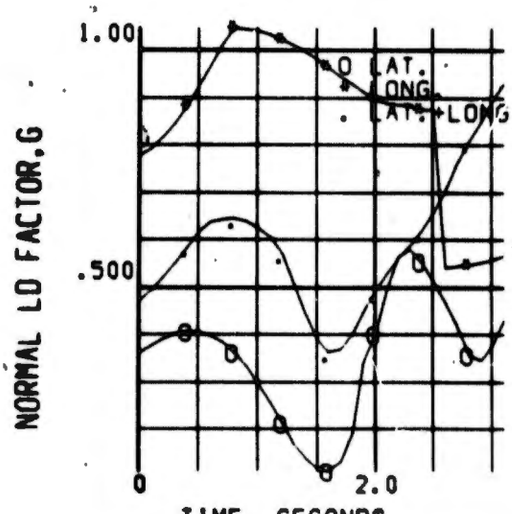

FIG 186 ENGINE,CONTROL FAILURE
46 KT, AIRPLANE LOAD FACTOR

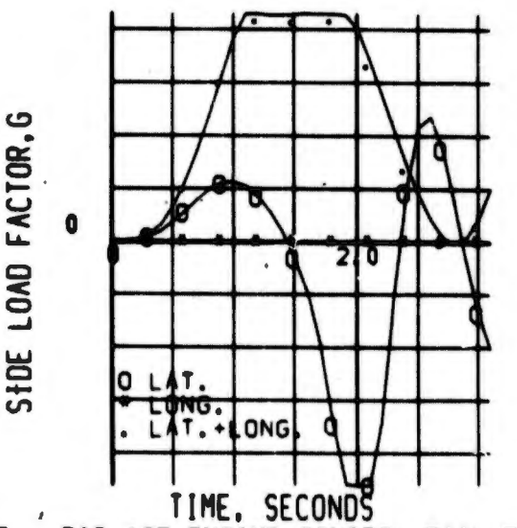

FIG 187 ENGINE,CONTROL FAILURE
46 KT, AIRPLANE LOAD FACTOR

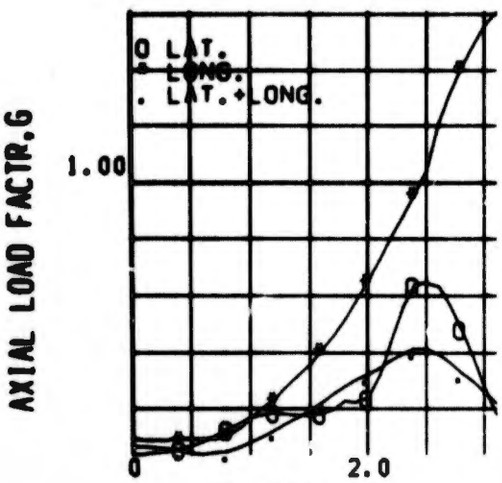

FIG 188 ENGINE.CONTROL FAILURE
46 KT, COCKPIT LOAD FACTOR

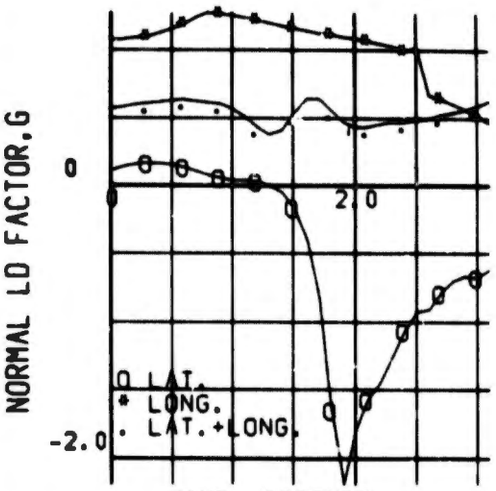

FIG 189 ENGINE.CONTROL FAILURE
46 KT, COCKPIT LOAD FACTOR

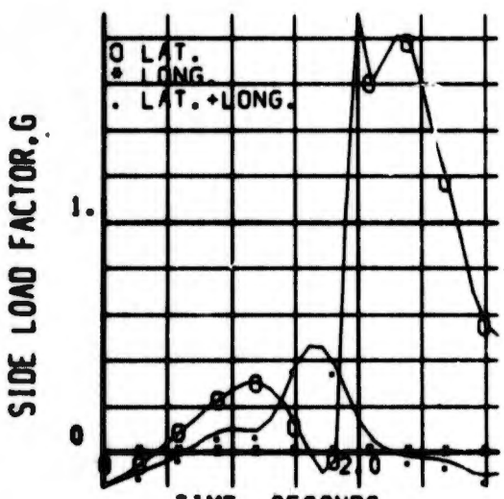

FIG 190 ENGINE.CONTROL FAILURE
46 KT, COCKPIT LOAD FACTOR

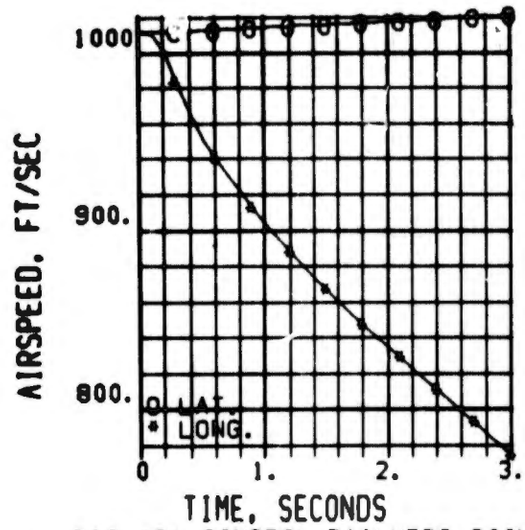

FIG 191 CONTROL FAILURES, 600KT AIRPLANE AIRSPEED

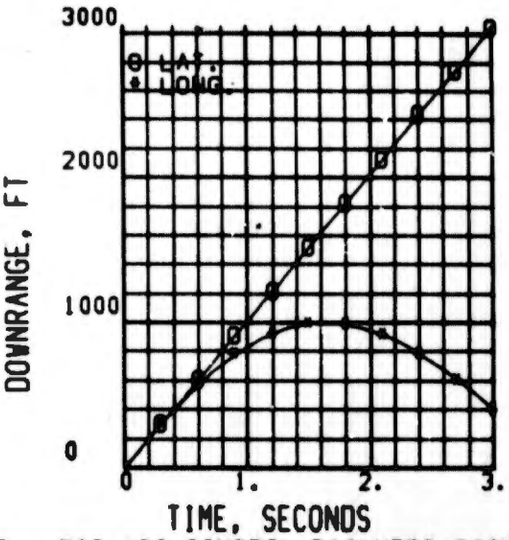

FIG 192 CONTROL FAILURES, 600KT AIRPLANE DOWNRANGE DISTANCE

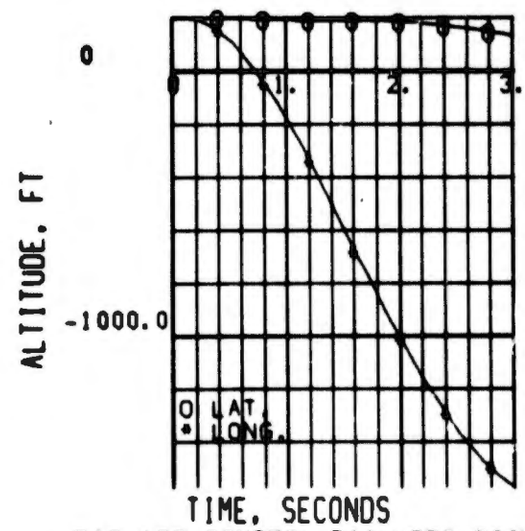

FIG 193 CONTROL FAILURES, 600KT AIRPLANE ALTITUDE

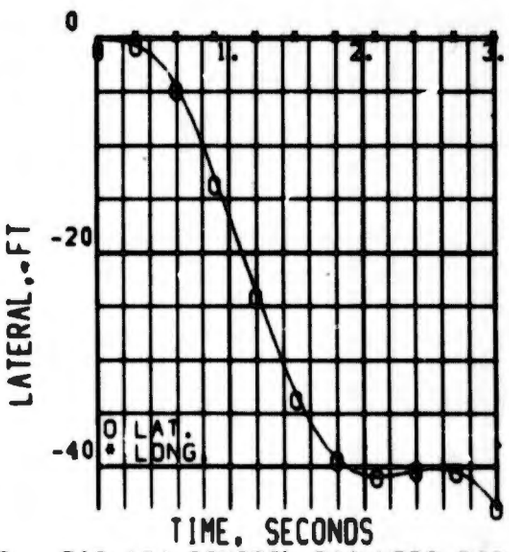

FIG 194 CONTROL FAILURES, 600KT AIRPLANE LATERAL DISTANCE

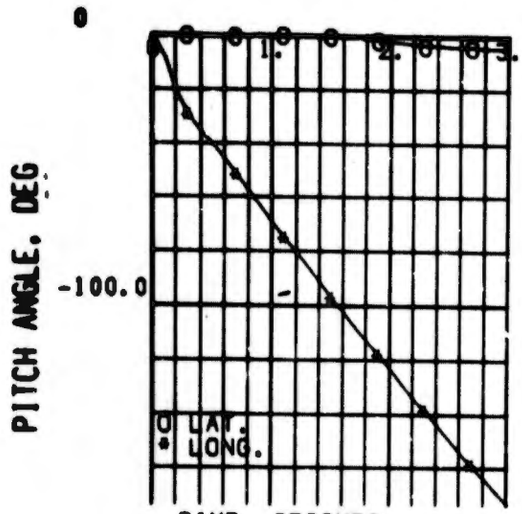

FIG 195 CONTROL FAILURES, 600KT AIRPLANE PITCH ANGLE

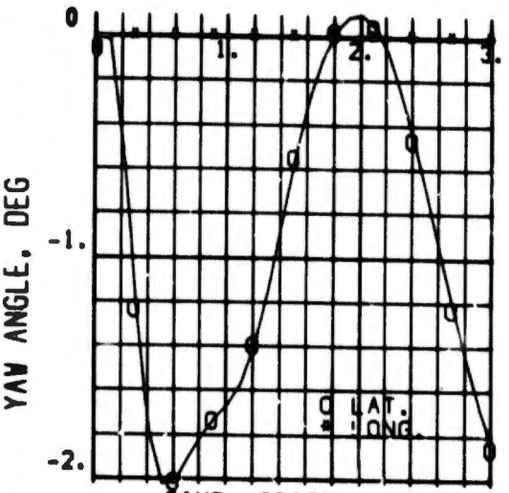

FIG 196 CONTROL FAILURES, 600KT AIRPLANE YAW ANGLE

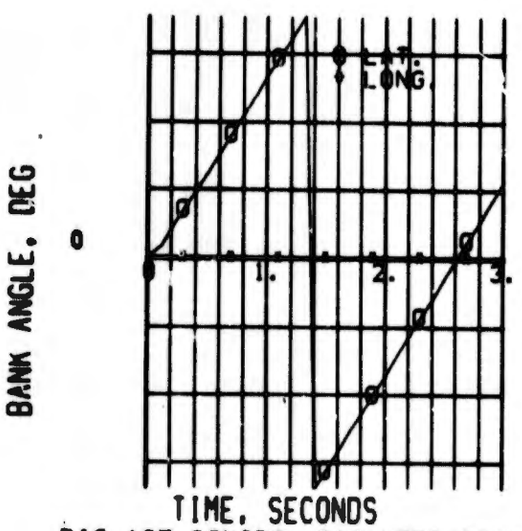

FIG 197 CONTROL FAILURES, 600KT AIRPLANE BANK ANGLE

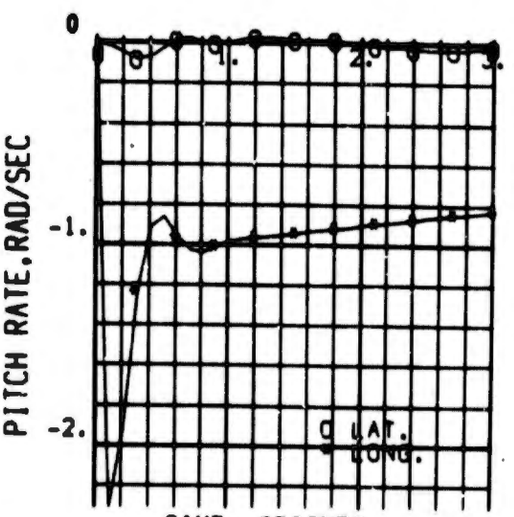

FIG 198 CONTROL FAILURES, 600KT AIRPLANE PITCH RATE

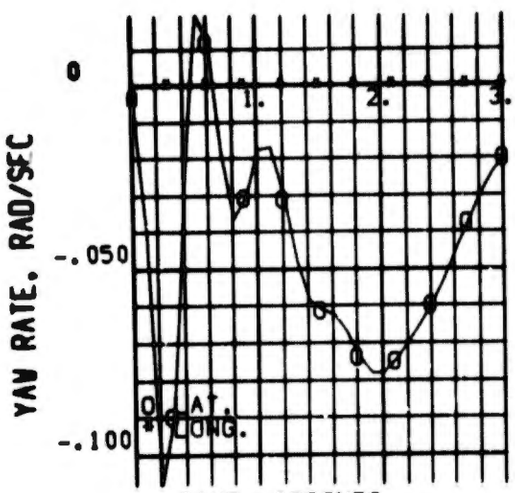

FIG 199 CONTROL FAILURES, 600KT AIRPLANE YAW RATE

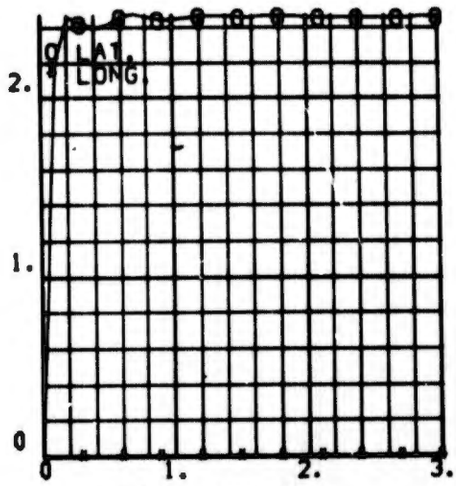

FIG 200 CONTROL FAILURES, 600KT AIRPLANE ROLL RATE

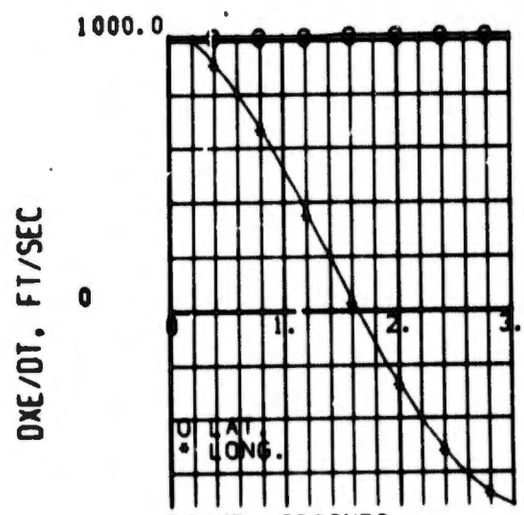

FIG 201 CONTROL FAILURES, 600KT AIRPLANE DOWNRANGE SPEED

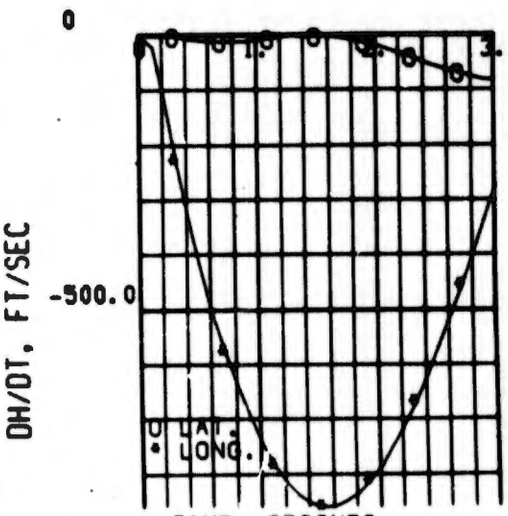

FIG 202 CONTROL FAILURES, 600KT AIRPLANE CLIMB RATE

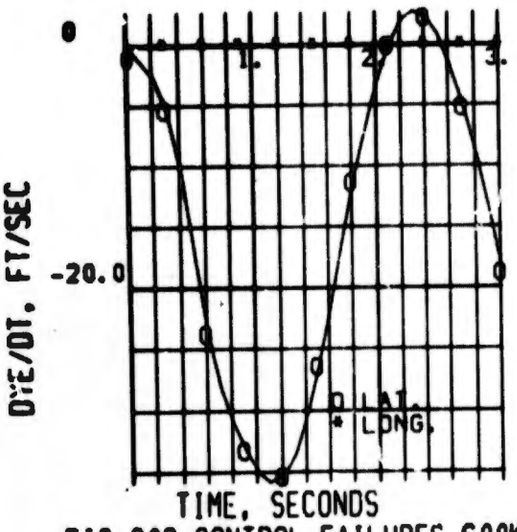

FIG 203 CONTROL FAILURES, 600KT
AIRPLANE LATERAL SPEED

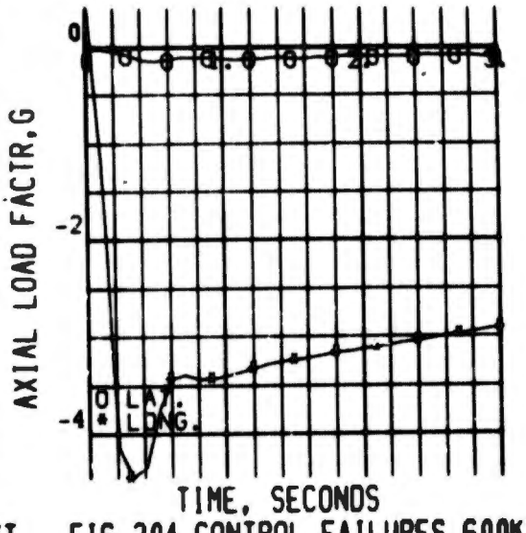

FIG 204 CONTROL FAILURES, 600KT
AIRPLANE AXIAL LOAD FACTOR

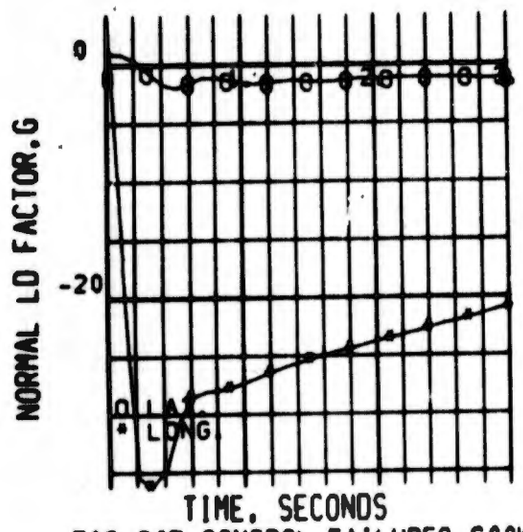

FIG 205 CONTROL FAILURES, 600KT
AIRPLANE NORMAL LOAD FACTOR

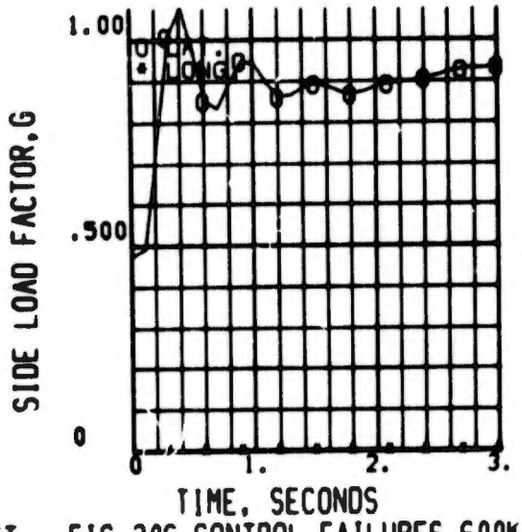

FIG 206 CONTROL FAILURES, 600KT
AIRPLANE SIDE LOAD FACTOR

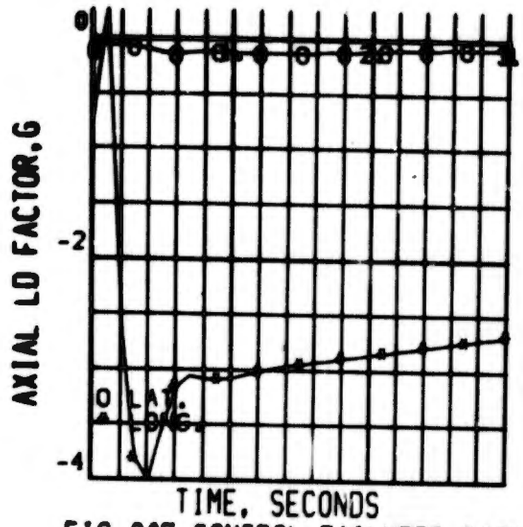

FIG 207 CONTROL FAILURES,600KT
COCKPIT AXIAL LOAD FACTOR

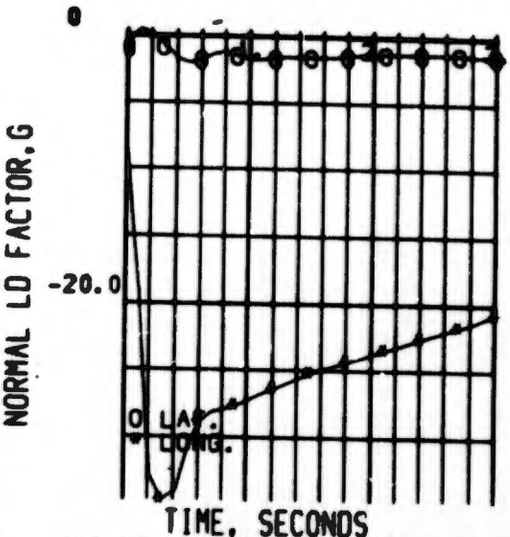

FIG 208 CONTROL FAILURES,600KT
COCKPIT NORMAL LOAD FACTOR

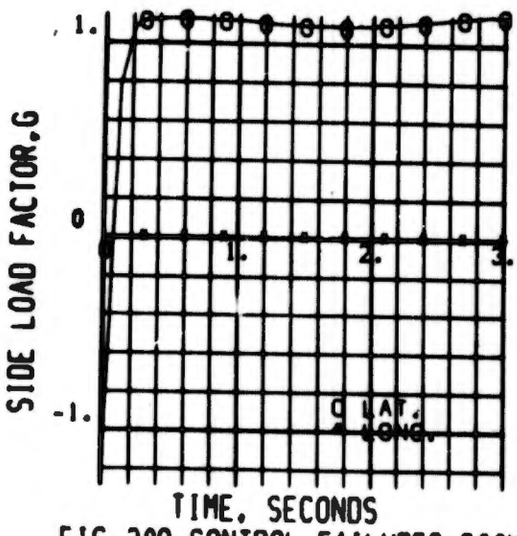

FIG 209 CONTROL FAILURES,600KT
COCKPIT SIDE LOAD FACTOR

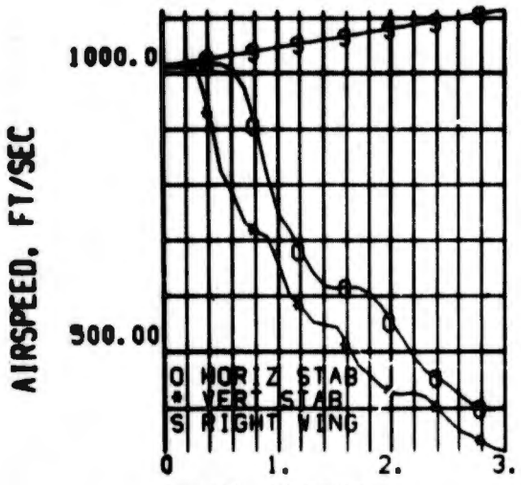

FIG 210 STRUCTURAL FAILURES
600 KT, AIRPLANE AIRSPEED

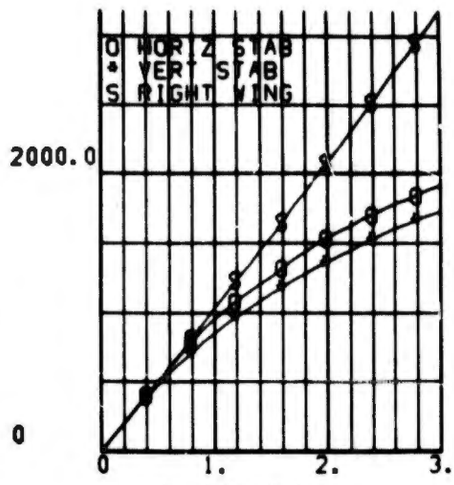

FIG 211 STRUCTURAL FAILURES
600 KT, AIRPLANE DOWNRANGE DIST

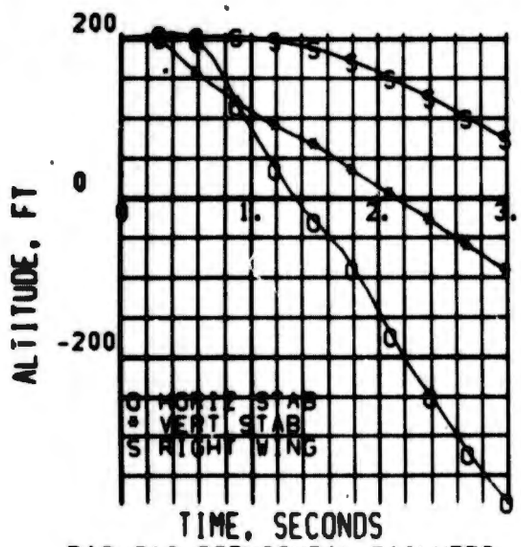

FIG 212 STRUCTURAL FAILURES
600 KT, AIRPLANE ALTITUDE

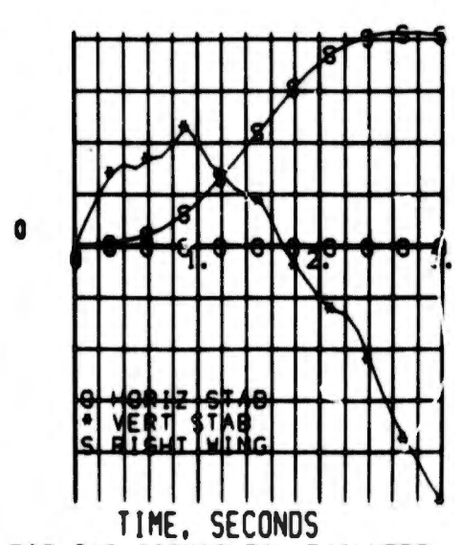

FIG 213 STRUCTURAL FAILURES
600 KT, AIRPLANE LATERAL DIST

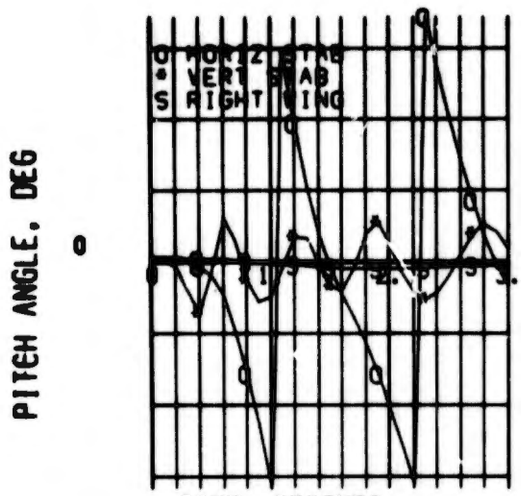

FIG 214 STRUCTURAL FAILURES
600 KT, AIRPLANE PITCH ANGLE

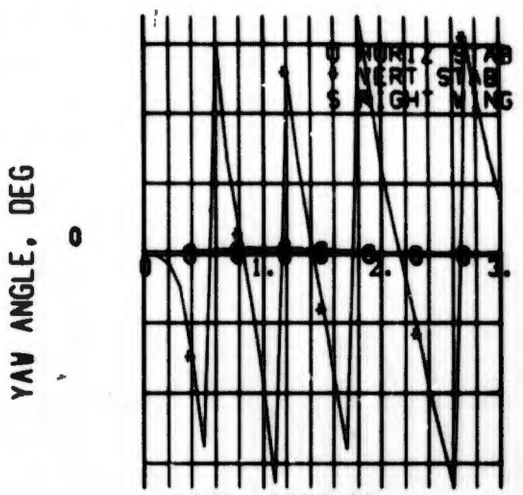

FIG 215 STRUCTURAL FAILURES
600 KT, AIRPLANE YAW ANGLE

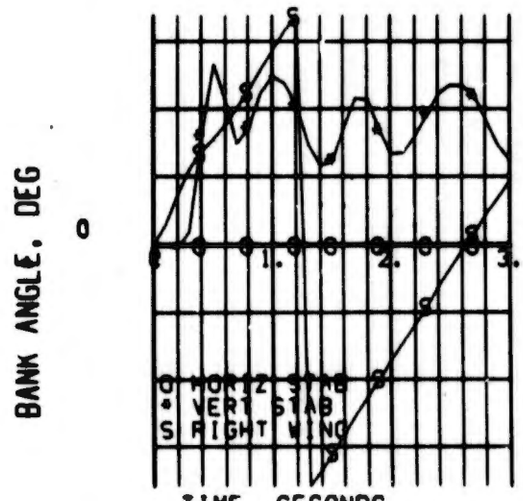

FIG 216 STRUCTURAL FAILURES
600 KT, AIRPLANE BANK ANGLE

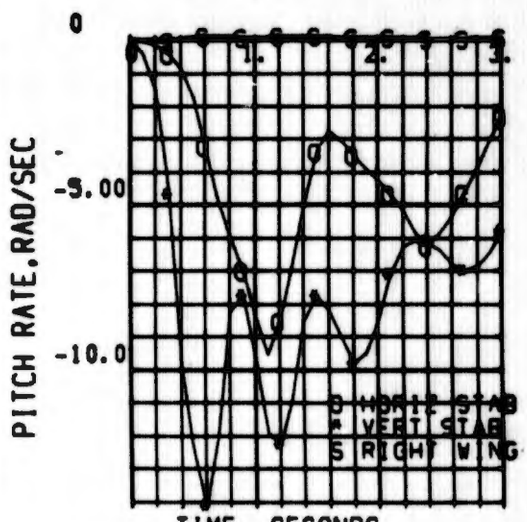

FIG 217 STRUCTURAL FAILURES
600 KT, AIRPLANE PITCH RATE

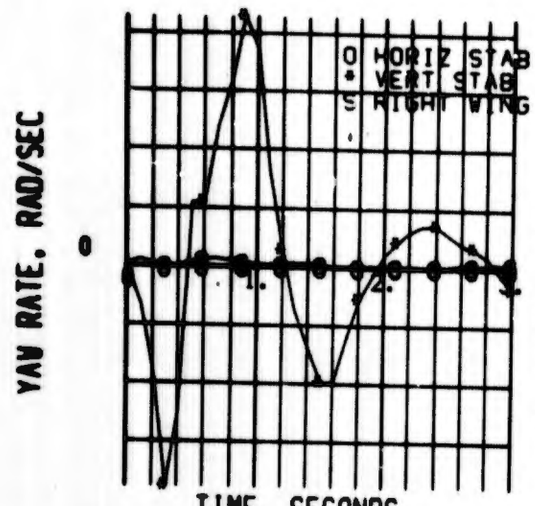

FIG 218 STRUCTURAL FAILURES
600 KT, AIRPLANE YAW RATE

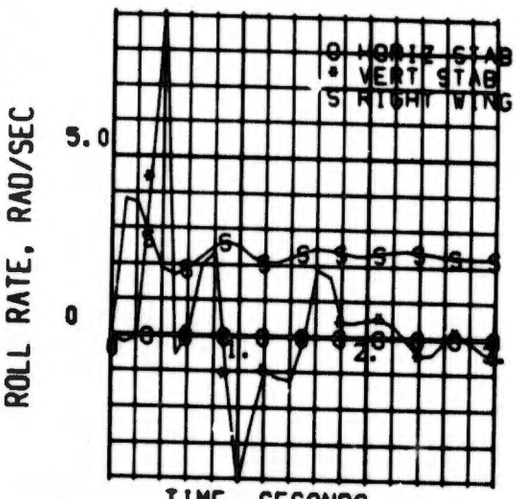

FIG 219 STRUCTURAL FAILURES
600 KT, AIRPLANE ROLL RATE

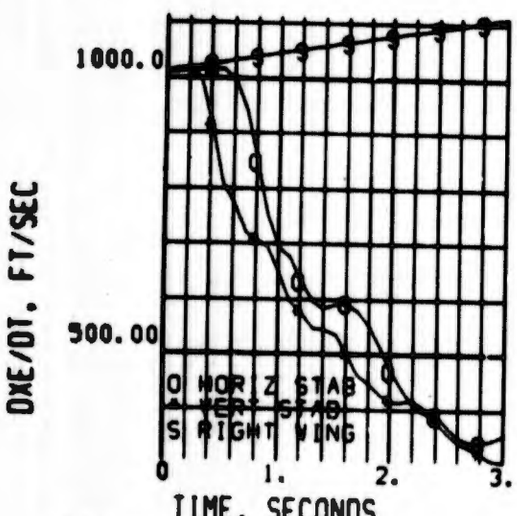

FIG 220 STRUCTURAL FAILURES
600 KT, AIRPLANE DOWNRNGE SPEED

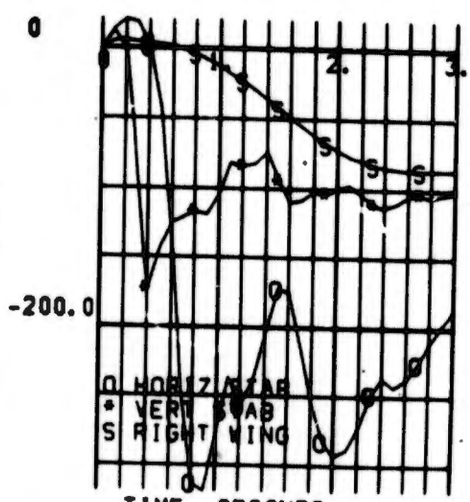

FIG 221 STRUCTURAL FAILURES
600 KT, AIRPLANE CLIMB RATE

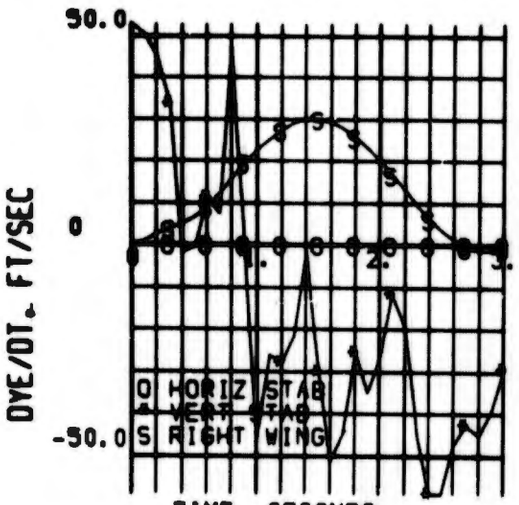

FIG 222 STRUCTURAL FAILURES
600 KT, AIRPLANE LATERAL SPEED

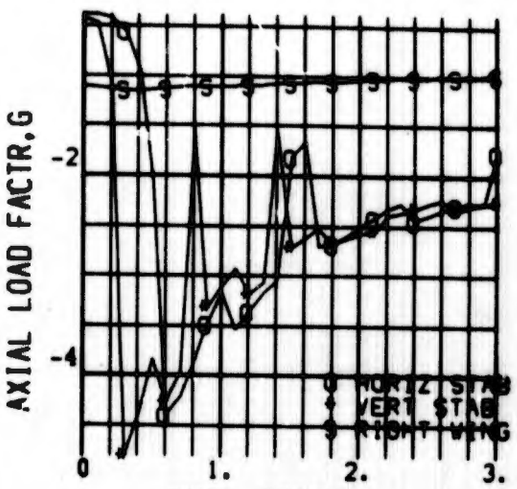

FIG 223 STRUCTURAL FAILURES
600 KT, AIRPLANE LOAD FACTOR

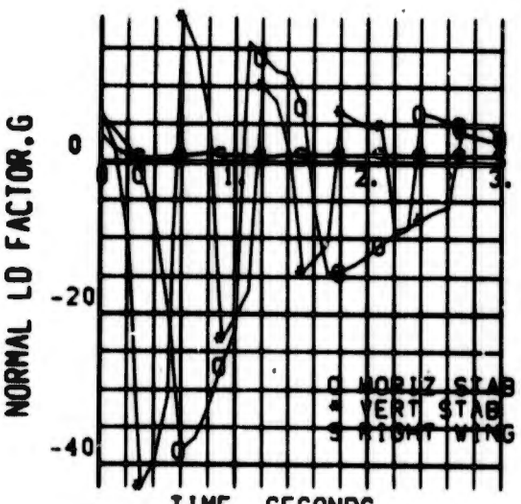

FIG 224 STRUCTURAL FAILURES
600 KT, AIRPLANE LOAD FACTOR

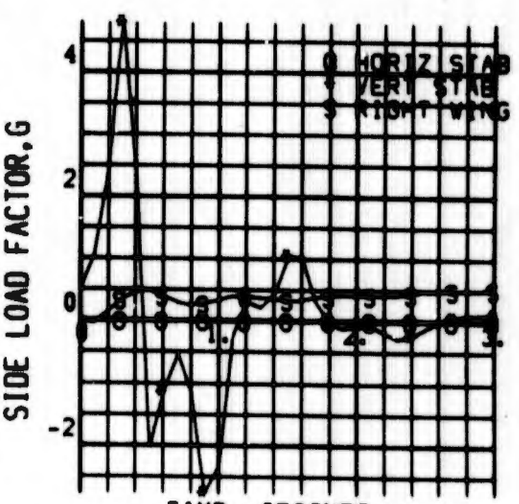

FIG 225 STRUCTURAL FAILURES
600 KT, AIRPLANE LOAD FACTOR

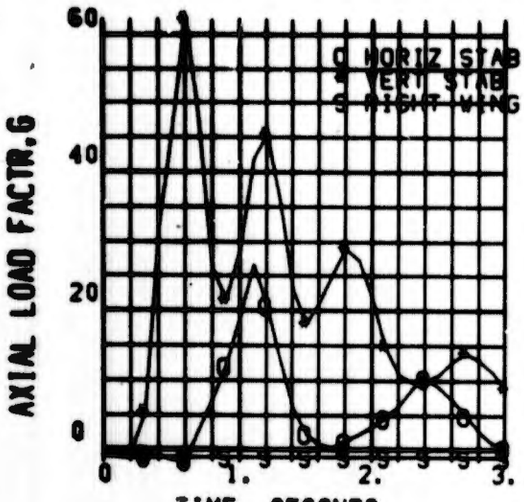

FIG 226 STRUCTURAL FAILURES
600 KT, COCKPIT LOAD FACTOR

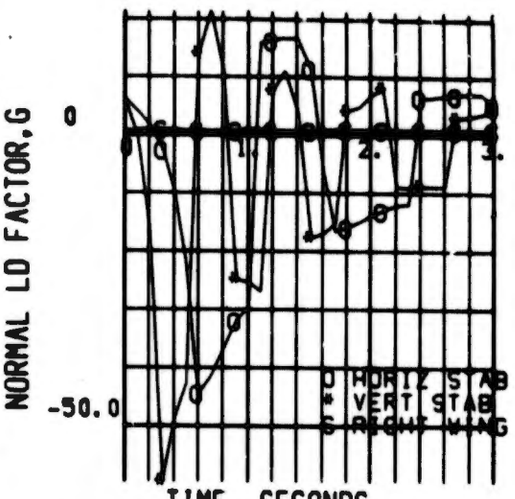

FIG 227 STRUCTURAL FAILURES
600 KT, COCKPIT LOAD FACTOR

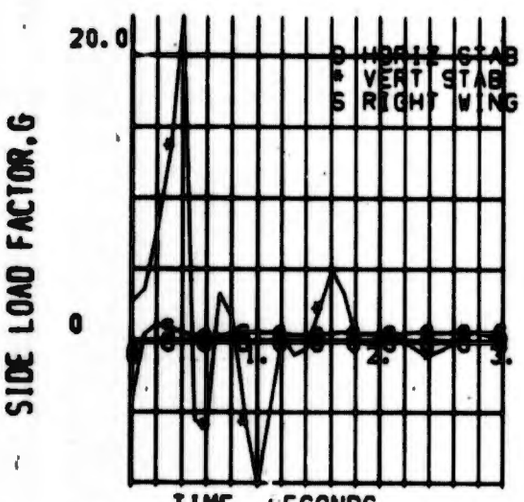

FIG 228 STRUCTURAL FAILURES
600 KT, COCKPIT LOAD FACTOR

REFERENCES

1. Ryan Aeronautical Company - Report of Preliminary System Analysis and Simulation for U. S. Army XV-5A Aircraft, Report No. 63B054, dated July 9, 1963.

2. Skelton, Grant B., Investigation of the Effects of Gusts on V/STOL Craft in Transition and Hover, Technical Report AFFDL-TR-68-85, Air Force Flight Dynamics Laboratory, Wright-Patterson Air Force Base, Ohio, October 1968.

3. General Electric Company, Final Systems Analysis and Flight Simulation Report - Volume I, AD 639 229, March 1965.

4. General Electric Company, Final Systems Analysis and Flight Simulation Report - Volume II, AD 639 230, March 1965.

5. General Electric Company, Phase I - Flight Test Results - Volume I, AD 639 231, March 1966.

6. General Electric Company, Phase I - Flight Test Results - Volume II, AD 639 232, March 1966

7. General Electric Company, Phase I - Flight Test Results - Volume III, AD 639 233, March 1966.

8. Lockheed-Georgia Company, Report No. ER-9052-XV-4B, Hummingbird Aerodynamic Report - dated 15 May 1968.

9. Fozard, J. W., First J. D. North Memorial Lecture and Main Society Lecture - "The Harrier."

10. United States Air Force, VSTOL Handling Qualities Evaluation, FTC-TR-68-10, P-1127 (XV-6A), dated August 1968.

11. Vought Aerodynamic Division DIR # 2-59320/9DIR-3-ADAM III CSX Weight and Inertia Data

12. Vought Aerodynamics Division Drawing No. L12-CSX-240.

BIBLIOGRAPHY

American Power Jet Company, Performance and Design Criteria for Deployable Aerodynamic Decelerators, TR No. ASD-TR-61-579, Aeronautical Systems Division, Wright-Patterson Air Force Base, Ohio, Dec 1963.

Evendale Demonstration Tests Completed Propulsion, Briefing Brochure X353-5 Vol 1, No. 5.

Perkins and Hage, Airplane Performance Stability and Control.

United States Air Force, United States Air Force Parachute Handbook, WADC TR 55-265, Wright Air Development Center, Wright-Patterson Air Force Base, Ohio, Dec 1958.

United States Air Force, Seat System: Upward Ejection, Aircraft, General Specifications for, Military Specification MIL-S-9479, Amendment 1, 27 Nov 1967.

United States Air Force, Six-Degree-of-Freedom Flight-Path Study Generalized Computer Program, Technical Documentary Report No. RTD-TRR-64-1, October 1964.

Unclassified
Security Classification

DOCUMENT CONTROL DATA - R & D

(Security classification of title, body of abstract and indexing annotation must be entered when the overall report is classified)

1. ORIGINATING ACTIVITY *(Corporate author)*
LTV Aerospace Corporation
Dallas, Texas 75222

2a. REPORT SECURITY CLASSIFICATION
Unclassified

2b. GROUP

3. REPORT TITLE
Study and Design of an Ejection System for VTOL Aircraft, Part I, Volume I, VTOL Aircraft Equations and Failure Mode Analysis

4. DESCRIPTIVE NOTES *(Type of report and inclusive dates)*
Final Report April 1969 December 1969

5. AUTHOR(S) *(First name, middle initial, last name)*
I. L. Clinkenbeard
E. O. Cartwright, Jr.

6. REPORT DATE	7a. TOTAL NO. OF PAGES	7b. NO. OF REFS
February 1970	142	12

8a. CONTRACT OR GRANT NO.	9a. ORIGINATOR'S REPORT NUMBER(S)
F33615-69-C-1692	N/A
b. PROJECT NO. 1362	
c. 136203	9b. OTHER REPORT NO(S) *(Any other numbers that may be assigned this report)*
d.	

10. DISTRIBUTION STATEMENT
This document is subject to special export controls and each transmittal to foreign governments or foreign nationals may be made only with prior approval of the AF Flight Dynamics Laboratory (FDFR), Wright-Patterson AFB, Ohio

11. SUPPLEMENTARY NOTES	12. SPONSORING MILITARY ACTIVITY
	Air Force Flight Dynamics Laboratory Air Force Systems Command Wright-Patterson Air Force Base, Ohio 45433

13. ABSTRACT

Equations are formulated for a hypothetical fighter/close support VTOL aircraft which will simulate a realistically severe crew station escape environment arising from aircraft failures in the VTOL and high speed, low altitude flight regimes. Four candidate airplanes with dissimilar propulsive and control concepts are analyzed and a lift-fan configuration selected to test the feasibility of any crew escape concept. Plotted time histories are presented of aircraft and crew station positions, rates, and accelerations occurring as a consequence of various failure modes. The time histories are summarized to reveal the extreme conditions encountered during VTOL and high speed emergencies, conditions for which existing escape systems are not designed.

(This document is subject to special export controls and each transmittal to foreign governments or foreign nationals may be made only with prior approval of the AF Flight Dynamics Laboratory (FDFR), Wright-Patterson AFB, Ohio.)

DD FORM 1 NOV 65 1473 (PAGE 1)
S/N 0101-807-6801

Unclassified
Security Classification

14. KEY WORDS	LINK A		LINK B		LINK C	
	ROLE	WT	ROLE	WT	ROLE	WT
Failure Mode Analysis						
VTOL Ejection Seat Escape System						
XV-5A VTOL						
VTOL Ejection System						
Crew Escape						
Ejection Propulsion Techniques						
VTOL Failures Modes						
XV-5A (Fan in Wing)						
VTOL Aircraft Equations						
VTOL Escape Seat Parameters						
Seat Tip-Off						
Drag Parachute						
VTOL Simulation Equations						
Conventional Flight Failure Modes						
VTOL and Transition Failure						